Development of a radiation computation dose model for use in ultraviolet phototherapy

David Robert Grimes

School of Physical sciences

Dublin City University

A thesis submitted for the degree of

Doctor of Philosophy

December 2010

Supervisor - Prof. Neil O'Hare

I hereby certify that this material, which I now submit for assessment on the programme of study leading to the award of Doctor of Philosophy is entirely my own work, that I have exercised reasonable care to ensure that the work is original, and does not to the best of my knowledge breach any law of copyright, and has not been taken from the work of others save and to the extent that such work has been cited and acknowledged within the text of my work.

Signed:

ID No.: 53449173

Date: 21/04/11

I would like to dedicate this PhD thesis to my long suffering and wonderful family who have been incredibly understanding, encouraging and supportive for not only the last three or so years since this research began, but throughout my entire life.

Acknowledgements

There exists a small army of people without whom this work come never have come into existence. I am deeply indebted to these people and hope to someday pay them back for their assistance, or failing that, emigrate under an assumed name. Chief among these people I would like to extend my profound thanks to my supervisor, Prof. Neil O'Hare of St. James's Hospital, who suffered my dangerous ideas for over a thousand days and will probably require an extended period of convalescence in a secure unit with padded walls for his trouble. I would also like to thank my equally long suffering internal supervisor Prof. Greg Hughes for his constant support, over which period of time I became rather gifted at pouncing on him with questions; Luckily for Greg, he's a fast mover. I would also like to thank my original internal Dr. Vince Ruddy who retired - whether this was due to the strains of having me as a student is as yet unclear.

I would also like to thank my close collaborator and mathematical genius Dr. Chris Robbins of Grallator who once made the foolish mistake of replying to an unsolicited e-mail query in a most helpful manner and has sadly been unable to shake me since then. Worse still, I know where he lives. I would be most remiss if I failed to mention my equally fantastic partners in crime at Royal Gartnavel Hospital in Glasgow, Dr. Colin Martin and Grame Phanco who has constantly catered to my borderline ridiculous ideas and allowed me use their impressive kit despite me suffering technical difficulties with anything more complex than a pencil. These gentlemen are also cunning experimentalists and their practical know-how was second to none.

As large chunks of this work required significant programming smarts, I wish to convey my deepest thanks to Dr. Tony Cafolla of DCU who took the time to help me code some things with some very pretty code, even if I almost reduced him to tears with my ugly variations! I would also like to thank Caroline Banahan and Rob Greene of DCU for their additional programming advice.

My support network in DCU deserve particular praise, especially Lisa Peyton (who turned a blind eye as I robbed bookshops worth of stationary and always got my accounts right!), Alan Hughes and Pat Wogan (who were pretty good at converting my impractical ideas into realistic ones), Dr. Enda McGlynn (who always had a fresh way of looking at things) and Dr. John Moore, who had the misfortune to share an office with me and was always picked on for advice! I would like to extend particular thanks to engineer extraordinaire Des Lavelle who can turn a doodle with a crayon on the back of a chewing gum wrapper into an engineering marvel seemingly without effort; the look of fear in Des's eyes whenever I approached his shop with some crazy idea I will never forget.

I would also like to thank all those at St James's Hospital who have allowed me work around them and trusted me with equipment worth significantly more value than the net worth of my life. In particular I'd like to thank Una O'Connor and Adam Markey for their much appreciated assistance!. Dr. Lynn Gaynor of the Mater hospital also deserves praise for being exceptionally helpful in all things ultraviolet related. Dr Donald Allen of Christie Hospital in Manchester and Dr. Steve Pye of NHS Lothian had much invaluable advice for us on paper writing and pitfalls. Much thanks goes to Dr. David Taylor of Gloucestershire Royal Hospital, who kindly donated a UV-1000 unit, which we savagely cannibalized for lamps, reflectors, power units and

our own amusement. I would also like to thank the staff at Waldmann who gave me technical details on their reflectors arrangements, in particular Marc Baermann and Petra Koch.

I also must thanks those friends of mine who got roped into helping me set up and conduct experiments, namely Niamh Lalor, Daniel Murray, Kevin Carney and Lee Hurley. I cannot thank you guys enough, and I thank you for helping out no matter how frustrating, ethically questionable or plain dangerous the undertaking may have been. Thanks must go to Larry Ward and Jason Fallon, who are particularly long suffering and transported unwieldy phototherapy cabins as a literally massive favour to me. Id also like to thank Hugh Wallace of the NHS for not only helping a relative stranger with a tricky experiment but being rather good company to boot. But the single biggest praise of all here has to go to my father, Brendan Grimes, who was exceptionally helpful with his engineering knowledge and downright tenacity - he kept encouraging when I had given up the will to even look at a UV tube - though apparently this is not recommended anyway - and gave me some great ideas about how to proceed. Words cannot express how helpful my Dad is and I cannot thank him enough for pushing me when I was slacking.

I must make particular mention to the collective of individuals who had the arduous task of proofing all the things I wrote, be they presentations, papers, conference abstracts or even this thesis. I would like to thank Ruth O'Beirne, Lorraine McCormack, Caroline Mac Namara and Sinead Griffin for taking my occasionally over-verbose and sometimes plain demented prose and helping transform it into something readable! Well readable if you're the kind of individual who reads tomes on patient dose..

On a personal note though, I cannot thank my friends and family

enough. Scientific endeavour is often immensely frustrating and difficult, and there was a few times I was myself immensely frustrating and difficult. Luckily for me, I was surrounded by good friends who cheered me up and inspired me, and could forgive the occasional bad humours / irrationality / homicides. My family were absolutely stellar - my mother Patricia was constantly full of good advice and support, despite struggling through her own masters at the same time and my father, as I have mentioned, was the enthusiasm behind this project when I had lost mine. My brother Steve was and is an absolute inspiration and could always make me work when I was starting to slouch - perhaps motivational speeches are something they secretly instill in teachers!

This work was funded through IRCSET through the EMBARK initiative.

Abstract

The ultimate motivation for this research is to investigate and quantify the nature of ultraviolet radiation for medical application over a variety of skin diseases. While application of both narrow-band and broad-band ultraviolet light have demonstrated great success in the treatment of a multitude of dermatological conditions, over-exposure to this section of the electromagnetic spectrum can be detrimental to human health, and the crux of the issue is striking a balance between maintaining a biologically effective dose while minimizing the impact on the overall health of the patient.

Treatment cabins typically consist of a series of ultraviolet emitting lamps surrounded by an array of anodized aluminium reflectors positioned around the lamp to increase the incident dose on the patient in the treatment cabin. Many different factors are important in estimating the patient dose, including the nature of lamp emission, the properties and placement of the reflectors and the position and self-shielding from the patient as well as cabin geometry. Lamp failure can also occur, complicating matters. A dose model that estimates all these factors and quantifies them could be of use in a variety of clinical applications.

This research focuses on methods of quantifying these various elements contributing to patient dose, and the creation of a dose model for patients undergoing ultraviolet phototherapy.

Contents

List of Figures

Nomenclature

Roman Symbols

β	Circular bisector angle (rad)
Ω	Solid angle (sr)
A_L	Linear attenuation / clipping function (unitless)
A_S	Squared attenuation / clipping function (unitless)
E	Irradiance (W/m^2)
I	Radiant Intensity ($Wm^{-2}sr^{-1}$)
R_F	Reflectance / Reflectivity (unitless)
S_L	Power per unit length (W/m)
S_R	Reduced power per unit length (W/m)
APD	Acquired perforating dermatosis
BB	Broad-band
BCC	Basal cell carcinoma
CRSD	Circadian rhythm sleep disorder
CTCL	Cutaneous T-cell lymphoma
DNA	Deoxyribonucleic acid

EM Electromagnetic

IRPA International Radiation Protection Association

MDF Medium density fibreboard

MED Minimal erythemal dose

MF Mycosis fungoides

MPD Minimal photo-toxic dose

NB Narrow-band

NRPB National Radiological Protection Board

PMLE Polymorphic light eruption

PUVA Psoralen and ultraviolet A

SCC Squamous cell carcinoma

ScUViDo Scottish ultraviolet dosimetry guidelines

UV Ultraviolet

UV-1000 Waldmann UV-1000 treatment cabin

UV-5000/5040 Waldmann UV-5000/5040 treatment cabin

UV-7001 Waldmann UV-7000 treatment cabin

UVR Ultraviolet Radiation

Part I

Literature Review

Chapter 1

Introduction

The observation that exposure to sunlight can be biologically beneficial for certain conditions affecting the skin has been known since antiquity. The ancient Greeks practiced a very early form of heliotherapy, and this knowledge was not just limited to hellenic cultures; the Assyrians, Egyptians, Romans and Inca practiced some form of worship equating the sun with health. Nor was this practice limited to hot climates exclusively; Worshipping the sun as a health bringing deity was also recorded by early German settlers (Ellinger 1957) and presumably other cultures. Scientific interest in the subject and the corresponding rigour that entails began in earnest around the 19th century, when investigations into the spectrum of the sun began. The ultraviolet portion of the solar spectrum, a subject at the very core of this work, was discovered by Johann Ritter in 1801 (Meyer 1952) when he showed beyond doubt that certain chemical reactions were triggered by some portion of sunlight beyond the violet. Later that century, Niels Finsen proved experimentally that it was ultraviolet radiation (UVR) that provided the mechanism for sunburn rather than the radiant heat such a name might suggest. The work of Finsen effectively laid the foundations for modern ultraviolet phototherapy (Magnus 1978) as he painstakingly researched the application of UVR to biological processes, and as a by-product improved contemporary understanding of UVR. Finsen was awarded the Nobel prize in Medicine and Physiology in 1903 "in recognition of his contribution to the treatment of diseases, especially lupus vulgaris, with concentrated light radiation, whereby he has opened a new avenue for medical science."

The early 20th century saw further developments in the field. The excitement over the potential applications of heliotherapy lead to the formation of the 'Light league' by the prolific writer and doctor Caleb Saleeby. Saleeby campaigned relentlessly for this project, and the mission statement of the league was "the education of the public to the appreciation of sunlight as a means of health; teaching the nation that sunlight is nature's universal disinfectant, as well as a stimulant and tonic". He recounted the testimony of a Dr. Rollier of Leysin who claimed to be able to cure or treat numerous diseases with sunlight alone, including spinal tuberculosis, war wounds and bed sores (Saleeby 1926). In a review on the subject by Diffey (1980), he aptly notes the contrast between the views of Saleeby and the opinion of the dermatologists at the VIIth International congress of Photobiology in Rome, 1976, who were of the opinion that excessive doses and even moderate exposure to sunlight could be potentially very harmful. Perhaps this historical background is the very epitome of phototherapy; beneficial at correct dosage, and potentially detrimental when taken to excess.

The term heliotherapy or light therapy can refer to a range of treatments for a multitude of ailments. For example, circadian rhythm sleep disorder (CRSD) often suffered by shift workers can be effectively treated using lightboxes (Smith and Eastman 2008). Babies born with neonatal jaundice can be treated with blue light or Bili light to break down bilirubin into compounds the infant can excrete (Ennever 1990). Specifically though, this work is concerned with the ultraviolet branch of phototherapy. Ultraviolet wavelengths have wavelengths between 100 - 400nm are are further subdivided into UVA (320 - 400nm), UVB (290-320nm) and UVC (100-290nm) but these borders between these subdivisions can vary slightly (Diffey & Hart 1997, Moseley 1988). Ultraviolet radiation treatments are used to treat a variety of skin conditions. For dermatological applications, UVR treatments tend to be either narrow-band UVB treatments centred around 311nm or broadband UVA treatments in conjunction with a skin photosensitizing agent or Psoralen, which readily absorbs UVA. The latter treatment is commonly referred to as a PUVA treatment (Green *et al* 1992).

Ultraviolet radiation is technically quite damaging to the molecular integrity of DNA through both direct and indirect interactions (Parrish *et al* 1982, Ribeiro *et al* 1991) and the human body has adapted the defense of melanin pigmentation (Fitzpatrick 1988) to counteract the negative repercussions of ultraviolet exposure and their detrimental side-effects; Acute ocular exposure to UVR can cause eye damage, particularly photokeratisis or snow blindness. Chronic over-exposure can result in increased incidence of cataracts (Sliney 2007). The signature effect of UVR on skin is erythema (sunburn), and in addition to this, light in the UV wavelength band can damage collagen, decreasing skin elasticity and promoting advanced aging and wrinkling (Diffey 1980, Fisher *et al* 1997). While these effects of UVR exposure are considerably unpleasant, the primary concern with this spectrum of radiation is the potential for carcinogenesis. Exposure to high amounts of ultraviolet radiation has long been a risk factor in developing skin cancers (de Gruijl 1999). In order of seriousness, cancers commonly associated with over-exposure to UVR are basal cell carcinoma , squamous cell carcinoma and malignant melanoma (Diffey and Hart 1997).

Given these seemingly negative effects of ultraviolet radiation on human biological tissue, it may seem surprising that UVR could be the basis for any medical therapy, especially for skin diseases. Yet UVR phototherapy is a well-proven and common treatment for dermatological conditions such as Psoriasis (Gordon *et al* 1999), Eczema (Grundmann-Kollmann 1999), Polymorphic light eruption (PMLE) (Hönigsmann 2008) and many other ailments. The reason why UVR is so effective at clearing these conditions is not entirely clear, but it is suspected that the ability of UV light to modulate the functioning of the immune system may be the reason. Many skin disorders are autoimmune in origin or originate with autoimmune diseases (Barker 1997), meaning that a patient's immune system incorrectly identifies cells in the patient's body as foreign pathogen and over-reacts to their presence, attacking them. The modulation of immune responses after exposure to UVR may help mitigate the over-reacting immune system (Schmitt and Ullrich 2000).

As two general treatment modalities for UVR phototherapy exist, the option to use one or the other comes down to the medical reality of the patient's condition. UVR treatments are most often used to treat skin conditions, which are highly idiosyncratic, and can manifest in various forms. Studies to date (Gordon *et al* 1999, Yones *et al* 2006, Sezar *et al* 2007) indicate that PUVA treatments clear certain forms of psoriasis better than narrow-band (NB) UVB treatments. However, many patients can have toxic reactions to the psoralen which renders it ineffective for some patients. Also, pregnant women and those on blood thinners or certain medications cannot use the photosensitizing agent, and thus UVB is often used. For chronic eczema, the clearance rate and duration of therapy is roughly the same for PUVA and NB-UVB (Sezar and Etikan 2007). NB-UVB treatments do not have the side-effects associated with PUVA treatments, such as as unpredictable phototoxic reactions, vomiting and nausea. NB-UVB therapy also has zero drug costs and shorter treatment duration (Njoo *et al* 2000) for patients with vitiligo. A study of patients suffering from lichen planus indicate that PUVA treatments perform better than NB-UVB treatments (Wackernagel 2007). For conditions like Vitiligo, evidence suggests UVB treatments work more effectively (Bhatnagar *et al* 2006). Investigation of treatment response to mycosis fungoides indicates strongly that NB-UVB is the best treatment modality (Diederen *et al* 2003). A study of NB-UVB as a treatment for perforating dermatosis indicates that is it an effective treatment (Ohe *et al* 2004). Clearly the modality of treatment should reflect the condition and patient response. Importantly, the carcinogenic potential of both modalities should be evaluated.

There is a body of evidence to suggest that long term PUVA treatments lead to higher carcinogenicity, specifically increased rates of squamous cell carcinoma (SCC) (Stern and Laird 1994). The same study concluded that NB-UVB treatments do not significantly increase the risk of developing SCC or basal cell carcinoma (BCC). A more recent study (Weischer *et al* 2004) confirms that while there is increased risk of cancers with PUVA treatments, NB-UVB treatments

do not seem to increase the risk. For this reason, along with the relative ease of treatments, many clinicians opt to use NB-UVB treatments if possible. The question of why PUVA treatments seem to increase incidence of cancers is still being examined, but research suggests that UVA can cause mutagenesis in mammalian cells (Jones *et al* 1987, Studniberg and Weller 1993).

The problem of ultraviolet dosimetry is one of great interest to medical physicists and clinicians in practice. The severity and extent of skin conditions varies significantly with patients, and it is critical to ascertain a safe yet effective dose. Treatment cabins typically consist of a number of fluorescent tubes as the UV source. The photons produced inside the lamp tube are typically UVC of wavelength $\lambda \approx 253.7$nm, produced by transitions from of mercury atoms excited by a current to a ground state. These photons are incident upon a phosphor coating on the tube wall, and depending on the chemical composition of the phosphor chosen, a photon of a desired wavelength or wavelength band can be emitted (Murdoch 1985). In the case of NB-UVB, the emitted photon is typically 311nm. These emitting lamps are generally placed in front of mirrors to increase the irradiation of the patient, and a typical cabin consists of many tubes in a variety of possible geometries. Phototherapy cabins are produced by a range of manufacturers, such as Waldmann, National Biological, Daavlin, Dixwell and Cosimo. Each of these companies produce many models with various numbers of tubes, reflector types and geometries, complicating the process of building a dose model somewhat. In addition to the problems of geometry, tube output can fluctuate with time and background temperature, complicating the process somewhat. Tubes often fail and need to be replaced, and this can complicate the picture of patient irradiance (Diffey and Hart 1997, Currie *et al* 2000). Measuring dose is important as it allows the operator to quantify the amount of UVR incident upon the patient and hence regulate the amount received and ensure it is close to the optimal amount, maximizing the benefits of treatment while minimizing the potential detrimental side effects.

Because of this huge variability in patient treatment solutions, the inherent variability of the treatment and the complexity of fully calculating dose, most phototherapy centres estimate dose using the Scottish ultraviolet dosimetry guidelines, or 'ScUVido' (Moseley 2001). In this system, a UVR protected clinician stands inside the cabin and using a radiometer calibrated to the specific wavelength of treatment, measures the irradiance at 12 different positions on their body. These measurements provide a baseline of irradiance at a particular position. This baseline is examined each week by the operator and any significant changes are recorded. These changes can indicate a lamp is failing, or has reduced in output and may need to be replaced. In practice, this method is exceptionally useful as it allows the operator to estimate cabin irradiance and any meaningful changes that occur. Essentially, it provides useful local calibration and is easily implemented and widely used. Despite this, it has some considerable drawbacks and potential causes of error; chiefly, the size and shape of the operator will influence the recorded irradiance through both geometrical changes and the effects of patient (or operator) self shielding (Langmack 1997). Also, reflections from the operator gown may throw off measurements. Also, the operator needs to be inside the cabin to get the measurements. While it gives good estimation, a more objective method is desirable. An automated irradiance detector for UVR phototherapy cabins has been developed (Currie *et al* 2000) by using a collimated and uncollimated detector pivoting on a stepper motor but due to component cost, most hospitals and clinics tend to use ScUVido.

The standard method for estimating what starting dose a patient should receive from the UVR treatment is usually decided in the case of NB-UVB by ascertaining the minimal erythema dose (MED) . This is the minimum level at which the patient responds with the classic skin reddening associated with erythema. Treatment then begins at a percentage of this level to keep the dose at suberythogenic levels throughout treatment. In the case of PUVA treatments, the minimal phototoxic dose (MPD) is obtained and treatment exposure is kept below this level (Bisland *et al* 1997, Diffey 2002, Gordon *et al* 1998). Although

guidelines in phototherapy state that MED/MPD is the standard method for establishing treatment levels, it has been acknowledged that there is currently no uniform protocol shared by all phototherapy centres (Damian *et al* 1997, Murphy *et al* 1997) and that different photocentres use a variety of methods to test skin response, including handheld devices, arrays of UV lamps and even entire phototherapy cabins (O'Connor and O'Hare 2003, Wishhart 2001). Because of this, there is a degree of ambiguity about the actual dosage received in photo-testing as well as in actual treatment.

These considerations lead to the conclusion that the development of a UVR dose model for phototherapy that could take account of the numerous factors that influence patient irradiation such as tube output, reflector contributions, cabin geometry and patient self-shielding would be of benefit to both clinicians and patients while avoiding the ambiguity of more ad hoc methods. The principle aim of this body of work is to outline and implement a dosimetry model for UVR treatments which can quantify the irradiance and dosage received by a patient on their body surface. Such a model could potentially shed light on processes such as photoadaptation, where the skin 'adapts' to UVR. A model that could quantify dose could also be used to examine the effects of failing lamps and off-centre patient placement.

Chapters 2 - 4 comprise the literature review section of this PhD thesis, establishing what work has been done in the field and the current understanding and methods used in UVR phototherapy and the areas of dosimetry, modeling and biological considerations associated with it. The production of UVR for treatment and the biological effects both positive and detrimental are discussed in some depth. These chapters also provide an overview of the current state of treatment and dosimetry methods commonly employed. The advantages and drawbacks of current dosimetry methods are outlined and the problems inherent in photobiology discussed in some depth. Existing models are examined and there is discussion on the factors influencing patient irradiance.

Chapter 5 onward is original research towards building a more powerful model, and investigations to that end. Chapter 5 concerns itself with a very simple radial model that has some merit and can give accuracy of within 10% in some limited cases. The radial model is investigated to see whether it could effectively be adapted for all cases. A discussion of patient shielding is also introduced. Chapter 6 heralds investigation into a formal line source model, treating the tube as a linear array of point sources. Using integral calculus and the properties of these point sources, this approach yields an analytical expression from irradiance from a lamp source. The major benefit of this model is that it takes account of the angle that radiation reaches it from, and so is applicable for any surface normal relative to the tube surface. Two forms of the solution are discussed; a simple case for a detector focused directly on a lamp and a powerful general form of the expression for any surface normal and radial vector from the tube are derived in this chapter as a promising method for characterizing tube output. Chapter 7 follows on from the prior chapter by rigorously testing the model through a variety of different experiments to ascertain how robust and effective it is. Both the simple and general form are investigated and found to describe the radiation emitted from the lamps to a very high degree, establishing that the formalized line source model amply characterizes UVR output from phototherapy lamps on any surface.

Chapter 8 expands the theory outlined in prior chapters extending it to reflections from the aluminium surfaces placed in phototherapy cabins to direct UV onto the patient. The extension assumes that the mirrors form images of the line source and these images can be treated as secondary sources and the resultant irradiance found. The picture is somewhat complicated by the fact that there will be as a consequence 'zones' of reflection from one mirror, both mirrors or none. A method for calculating the zones of reflection is also introduced. Chapter 9 investigates the theory established in the preceding chapter to determine its validity and examine whether it is experimentally vindicated and in what circumstances.

Chapter 10 puts all the research together and gives examples of how such a complete dose model could be implemented in practice, using examples of real

situations that can occur in practice. A discussion of observations, future work and conclusions is found in the concluding chapter.

1.1 References

- Barker JNWN 1997 Immunology of psoriasis *JEADV* **9** 71-72
- Bhatnagar A, Kanwar AJ, Parsad D and De D 2007 Comparison of systemic PUVA and NB-UVB in the treatment of vitiligo: an open prospective study *JEADV* **21** 638-642
- D Bilsland, BL Diffey, PM Farr, J Ferguson, NK Gibbs, JLM. Hawk, BE. Johnson, IA Magnus, H Moseley, GM Mruphy, PG Norris and A Pierce 1992 Diagnostic phototesting in the United Kingdom *Br. J. Deramtol.* **127** 297-299
- Currie G D, Evans A L, Smith D, Martin C J, McCalman S and Bilsland D 2001 An automated dosimetry system for testing whole-body ultraviolet phototherapy cabinets *Phys. Med. Biol.* **46** 333 - 346
- Damian DL, Halliday GM and R Barnetson 1997 Prediction of minimal erythema dose with a reflectance melanin meter *Br. J. Deramtol.* **136** 714-718
- de Gruijl FR 1999 Skin cancer and solar UV radiation *Eur. J. Cancer.* **35** 2003-2009
- Diederen PVMM, Van Weelden H, Sanders CJG, Tooshra J and Van Vloten WA 2003 Narrowband UVB and psoralen-UVA in the treatment of early-stage mycosis fungoides: A retrospective study *J. Am. Acad. Dermatol.* **48** 215-219
- Diffey BL 1980 Ultraviolet radiation physics and the skin *Phys. Med. Biol.* **25** 405-426
- Diffey BL and Hart G 1997 *Ultraviolet and Blue-Light Phototherapy - Principles, Sources, Dosimetry and safety.* York: IPEM

- Diffey BL 2002 What is light ? *Photodermatol. Photoimmunol. Photomed.* **18** 68-74
- Ellinger F 1957 *Medical Radiation Biology* (Springfield: Charles C. Thomas) 614
- Ennever JF 1990 Blue light, green light, white light, more light: treatment of neonatal jaundice *Clin. Perinatol.* **17** 467-81
- Fisher GJ, Wang ZQ, Datta SC, Varani J, Kang S and Voorhees JJ 1997 Pathophysiology of premature skin aging induced by ultraviolet light *New. Engl. J. Med.* **337** 1419 - 1428
- Fitzpatrick TB 1988 The validity and practicality of sun-reactive skin types I through VI. *Arch. Dermatol.* **124** 869871
- Gordon PM, Saunders PJ, Diffey BL, Farr PM 1998 Phototesting prior to Narrowband (TL-01) Ultraviolet B Phototherapy *Br. J. Deramtol.* **139** 811-814
- Gordon PM, Diffey BL, Matthews JNS and Farr PM 1999 A randomized comparison of narrow-bandTL-01 phototherapy and PUVA photochemotherapy for psoriasis *J. Am. Acad. Dermatol.* **41** 728-732
- Green C, Diffey B L, and Hawk J L M 1992 Ultraviolet Radiation in the treatment of Skin disease *Phys. Med. Biol.* **37** 1-20
- Grundmann-Kollmann M, Behrens S, Podda M, Peter RU, Kaufmann R and Kerscher M 1999 Phototherapy for atopic eczema with narrow-band UVB *Am. Acad. Dermatol.* **40** 995-997
- Hönigsmann H 2008 Polymorphous light eruption *Photodermatol. Photo.* **24** 155161
- Jones CA, Huberman E, Cunningham ML and Peak MJ 1987 Mutagenesis and Cytotoxicity in Human Epithelial Cells by Far- and Near-Ultraviolet Radiations: Action Spectra *Radiat. Res.* **110** 244-254

- Langmack K A 1997 An insight into the contributions of self-shielding and lamp reflectors to patient exposure in phototherapy units *Phys. Med. Biol.* **43** 207 - 214
- Magnus IA 1978 *Ultraviolet radiation and its medical applications* HSA report CRS-28 (HPA: 47 Belgrave square, London SW1X 8QX) 5
- Meyer AEH 1952 *Strahlentherapie* **88** 481
- Moseley H 1988 *Non-ionising radiation : microwaves, ultraviolet and laser radiation* (Bristol : Hilger)
- Moseley H 2001 Scottish UV Dosimetry guidelines "ScUVido" *Photodermatol. Photoimmunol. Photomed.* **17** 230-233
- Murdoch 1985 *Illumination engineering - from Edison's lamp to the laser* New York : London : Macmillan Pub. Co ; Collier Macmillan Publishers
- Murphy GM, McCann P, O'Leary A and Rogers S 1997 Guidelines for the use of phototherapy and photochemotherapy in Ireland *Irish. J. Med. Sci.* **166** 92-97
- Njoo MD, Bos JD and Westerhof W 2000 Treatment of generalized vitiligo in children with narrow-band (TL-01) UVB radiation therapy *J. Am. Acad. Dermatol.* **42** 245-253
- O'Connor U and O'Hare NJ 2003 Development of Action levels for MED/MPD Skin-testing units in Ultraviolet Phototherapy *Proc. of SPIE* **4876**
- Ohe S, Danno K, Sasaki H, Isei T, Okamoto H and Horio T 2004 Treatment of acquired perforating dermatosis with narrowband ultraviolet B *Am. Acad. Dermatol.* **50** 892-894
- Parrish JA, Jaenicke KF and Anderson RR 1982 Erythema and melanogenesis action spectra of normal human skin *Photochem. Photobiol.* **36** 187-191

- Ribeiro DT, Madzak C, Sarasin A, Di Mascio P, Sies H and Menck CFM 1991 Singlet oxygen induced DNA damage and mutagenicity in a single-stranded SV40-based shuttle vector *Photochem. Photobiol.* **55** 39-45

- Saleeby CW 1926 *Sunlight and Health* (London: Nisbet) 3rd edition 72

- Schmitt DA and Ullrich SE 2000 Exposure to Ultraviolet Radiation Causes Dendritic Cells/Macrophages to Secrete Immune-Suppressive IL-12p40 Homodimers *J. Immunol.* **165** 3162-3167.

- Sezar E and Etikan I 2007 Local narrowband UVB phototherapy vs. local PUVA in the treatment of chronic hand eczema *Photodermatol. Photoimmunol. Photomed.* **23** 1014

- Sezar E, Erbil AH, Kurumlu Z, Tastan HB and Etikan I 2007 Comparison of the efficacy of local narrowband ultraviolet B (NB-UVB) phototherapy versus psoralen plus ultraviolet A (PUVA) paint for palmoplantar psoriasis *J.Dermatol.* **34** 435440

- Sliney D H, 1997 Ultraviolet radiation effects upon the eye: Problems of dosimetry *Radiat. Prot. Dosim.* **72** 197 - 206

- Smith MR and Eastman CI 2008 Night shift performance is improved by a compromise circadian phase position: study 3. Circadian phase after 7 night shifts with an intervening weekend off. *Sleep* **31** 163945

- Stern RS and Laird N 1994 The Carcinogenic Risk of Treatments for Severe Psoriasis *Cancer* **73** 2759 - 2764

- Studniberg HM and Weller P 1993 PUVA, UVB, psoriasis and nonmelanoma skin cancer *J. Am. Acad. Dermatol.* **29** 1013-1022

- Wackernagel A, Legat FJ, Hofer A, Quehenberger F, Kerl H and Wolf F 2007 Psoralen plus UVA vs. UVB-311 nm for the treatment of lichen planus *Photodermatol. Photoimmunol. Photomed* **23** 1519

- Weischer M, Blum A, Eberhard F, Röcken M and Berneberg M 2004 No Evidence for Increased Skin Cancer Risk in Psoriasis Patients Treated with Broadband or Narrowband UVB Phototherapy: A First Retrospective Study *Acta. Derm. Venereol.* **84** 370374

- Wishhart J 2001 A new method of skin testing before narrowband UVB therapy *Photodermatol. Photoimmunol. Photomed.* **17** 197-199

- Yones SS, Palmer RA, Garibaldinos TT and Hawk JLM 2006 Randomized Double-blind Trial of the Treatment of Chronic Plaque Psoriasis *Arch. Dermatol.* **142** 836-842

Chapter 2

Biological effects of Ultraviolet Radiation

2.1 Ultraviolet radiation

The UVR portion of the electromagnetic spectrum lies between 100nm and 400nm, between the visible and X-ray part of the spectrum as illustrated in figure 2.1. The term 'ultraviolet' (UV) arises as this wavelength band begins just beyond visible violet light. The UV band is usually divided into three further subdivision; UVA, UVB and UVC based on their respective biological effects. The most commonly encountered classification is that defined by the International Commission on Radiation (CIE) (CIE,1970) shown in table 2.1.

Table 2.1: CIE Ultraviolet classification

Classification	**Wavelength Band**
Ultraviolet A (UVA)	400nm - 315nm
Ultraviolet B (UVB)	315nm - 280nm
Ultraviolet C (UVC)	280nm - 100nm

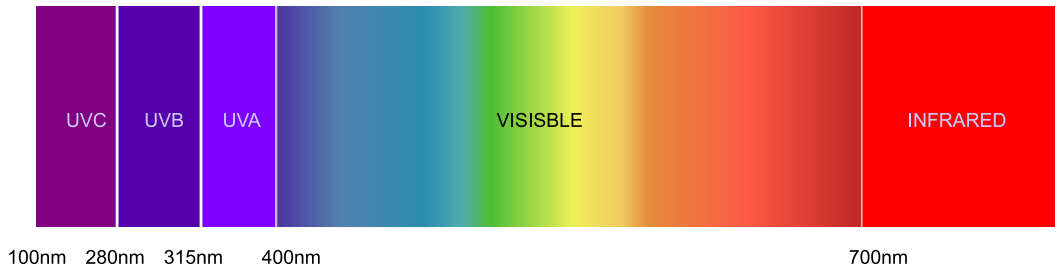

Figure 2.1: *Sections of the Electromagnetic spectrum*

While this is the most common classification, variations exist on the boundaries between these bands. Sometimes 320nm is taken as the boundary between UVA and UVB and 290nm as the boundary between UVB and UVC (Diffey and Hart 1997). The sun is the primary source of UVR incident upon the Earth's surface. While the sun emits large amounts of all UVR, the Earth's atmosphere is remarkably able at attenuating the more biologically harmful bands by absorbtion; wavelengths of less than 290nm are effectively removed by the atmosphere and as a result are not present on the Earth's surface. Of the sun's radiation that reaches Earth, only 5% is in the UVR range. Rayleigh scattering by particles of oxygen and nitrogen has a significant effect on reducing UVR with wavelengths longer then 310nm (Moseley 1988). Of the UVR that reaches the Earth's surface, 96.65% is UVA and 3.35% is UVB (Diffey 2002).

2.2 Production of Artificial UVR

There are several ways to produce UVR, including gas discharge lights, arc lamps and metal halide lamps. In the context of ultraviolet phototherapy, the UV source used is a fluorescent lamp therefore this section will focus on this mechanism. A fluorescent tube operates on the same principle as a gas discharge lamp - the lamp consists of a tube containing a low pressure gas or gas mixture which is ionized by running a current through it. These excited atoms fall back to their ground state, emitting a photon. The wavelength of this emitted photon is dependent on the gas mixture used. Additionally, the tube itself is often coated with a phosphor so that when the emitted photon is incident upon the tube walls, it stimulates the emission of a photon of a different wavelength through the mechanism of fluorescence. UVR lamps use a mixture of mercury vapor

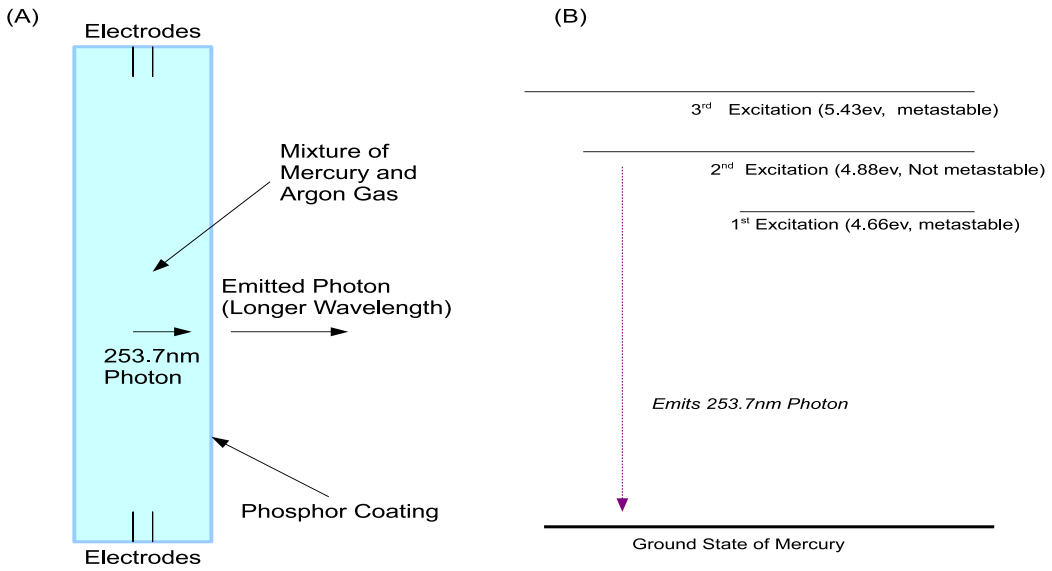

Figure 2.2: *(A) UVR tube (B) Energy states of mercury gas*

and inert argon gas. Electrons are emitted from the electrodes at either end of the tube either by thermionic emission, high-field emission or a mixture of both methods. These electrons are accelerated by the applied electric field where they encounter the argon atoms and excite them. The first ionization stage of Argon is metastable (11.56 eV), and the Argon helps establish an arc by forming a Penning mixture with Mercury; this has the net effect of making mercury easier to excite to the desired level (Murdoch 1985). Mercury has an ionization level of 10.39 eV and an excited state at 4.88 eV that is not metastable, so the excited atoms revert immediately to their ground state and radiate a photon in the UVC range of wavelength 253.7nm as in figure 2.2. These photons then impinge on the phosphor coat of the tube and fluoresce and emit a photon of a wavelength dependent on the phosphor used. For a visible fluorescent lamp, this output will be over a broad-band with an average wavelength of 555nm. For a narrow-band tube such as the TL/01 used in phototherapy, the output will be narrow-band at 311nm. The mechanism remains the same in both cases, but the type of phosphor used determines the output wavelength. Mercury is used as the active gas for three main reasons; firstly, it produces a single ultraviolet line and has a high

probability of reaching the emitting non-metastable state. Secondly, because it is a material with a vapor pressure of $1.8\mu m$ at room temperature which means the lamp does not have to be heated excessively. And finally, for high luminous output it is required that the source have a high quantum ratio. This quantity is defined as

$$QR = \frac{E_O}{E_{UV}} = \frac{\lambda_O}{\lambda_{UV}} \tag{2.1}$$

where E_O and E_{UV} are the respective energies of the output and ultraviolet photons and λ_O and λ_{UV} their respective wavelengths. So for a tube producing visible light at 555nm, the QR is 0.46 and for a narrow-band UV tube at 311nm, the QR is very high at 0.8158 (Murdoch 1985). Using inert gases such as argon in the mixture helps establish the arc as they ionize at lower tube voltages than other gases, increasing the likelihood of further excitation. The excitation of inert gas also leads to the Penning effect, making the process more efficient. Lastly, the mercury arc must be contained, and without the inert gas pressure the mercury atoms and ions would move towards the tube wall, making the resultant combinations excessive and inefficient. The presence of the inert gas in the form of argon counteracts this (Murdoch 1985, Diffey and Hart 1997).

Gas discharge lamps are examples of negative resistance phenomena, which essentially means that as current increases, lamp voltage decreases. This must be controlled with in order to limit current. The most simple solution is to use a resistor but this leads to large power loss and reduction in efficiency. Consequently, resistive ballasting is thus used only when a lamp is being operated under conditions of direct current. For all other situations, reactive or electronic ballasting is employed to regulate the current running into the lamp (Murdoch 1985)

2.3 Characteristics of fluorescent UVR sources

2.3.1 Source Spectra

The output spectra of a particular lamp will depend upon the gas mixture and phosphor used. For different theraputic applications, different spectra may be used and as a result there are many readily available commercial lamps with varying outputs at various wavelengths available. While UV lamps are often divided into UVA and UVB lamps, this does not always characterize the lamps themselves; some may have output in both the UVA and UVB or may be relatively broad-band across the spectrum (Diffey and Hart 1997) so it is more correct to analyze UVR lamps in terms of their spectral power distribution. Outputs of some common UVR lamps are shown in figure 2.3.

2.3.2 Source stability and output

Individual fluorescent lights reach full output within one minute of being powered on (Diffey and Hart 1997). However, factors such as temperature of the cabin can have an influence when many lamps are being operated together, as is usually the case in a clinical setting. In such cases it can take up to 15 minutes for the lamps to stabilize, depending on the degree of forced cooling provided by the unit. Maximum UVR output is achieved when the lamps are run in free air with ambient temperatures of $25 - 30$ degrees centigrade. If cooling is not adequate and temperature increases above 30 degrees the output decreases for older model tubes (Diffey and Hart 1997) but some newer tubes have an optimal temperature of 40 degrees centigrade (Phillips 2007) as shown in figure 2.4. Tube output also decreases with active lifetime; Fluorescent lamps typically have a 'running in' period where the radiation output rate falls steeply in comparison to the tube's later life. This period is typically 100 hours. The useful lifetime of a tube is approximately 500-1000 hours, after which tubes tend to fall to about $70 - 80\%$ of their output at the end of the running in period. At such a time the tubes are typically replaced.

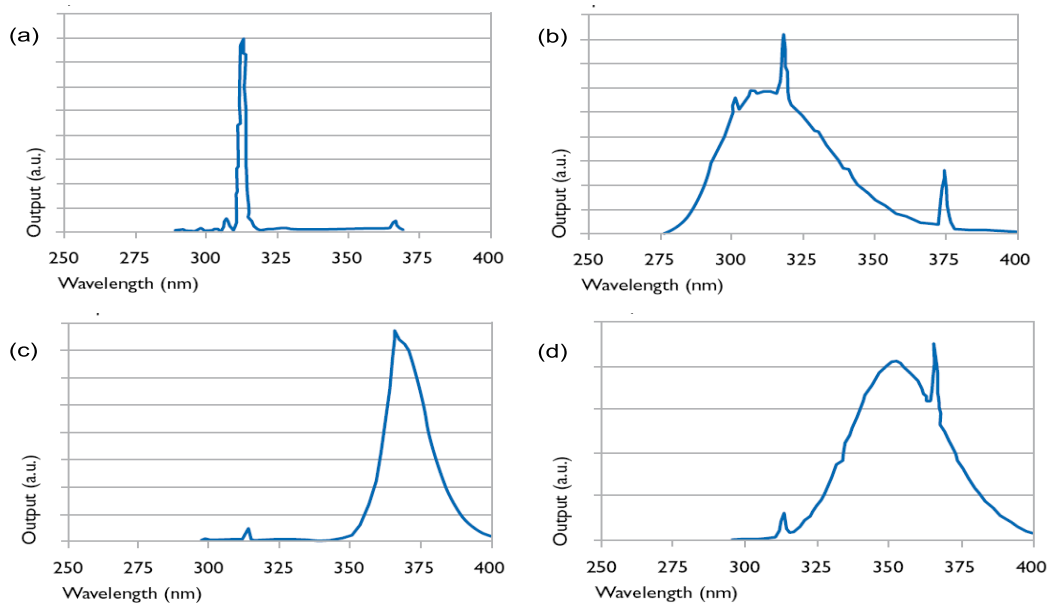

Figure 2.3: *Spectral outputs from some common Phillips UV lamps (a) Narrow-band TL/01 (b) TL/12 (c) TL/10 (d) TL/209.*(Phillips 2007)

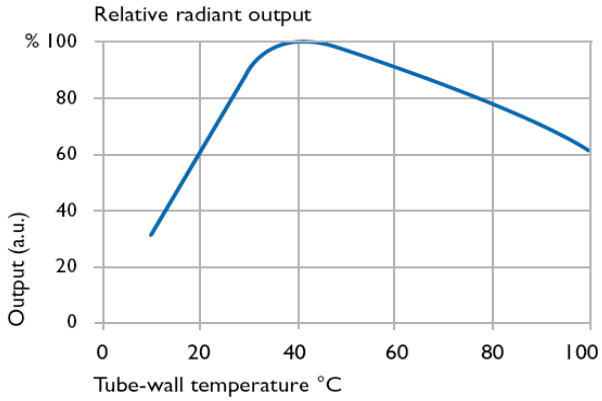

Figure 2.4: *Radiant output versus tube temperature for phillips UV lamps* (Phillips 2007)

2.4 UVR reactions with DNA and melanin

Melanin and Deoxyribonucleic acid (DNA) are extremely efficient and well adapted photo-protective agents. This is due to them having an extremely efficient internal conversion, converting the vast majority of incident UV photons to harmless amounts of heat. Melanin and DNA in skin can convert the vast majority of incident UV to small amounts of heat which dissipate harmlessly as the ultrafast conversion process of DNA means that the excited life-time is in the femtosecond ($10^{-15}s$) regime, and thus the excited molecule doesn't have enough time to react with other molecules. If the excited state was much longer, then it would lead to the generation of harmful free radical and reactive species like the hydroxyl radical or singlet oxygen which would damage DNA (Ribeiro *et al* 1991).

The quantum yield (percentage of molecules quickly dissipating the photon to heat) of both DNA and eumelanin, the form of melanin most common in humans is over 99.9% for both molecules (Meredith and Riesz 2004). While the photo-protection provided by these agents is extremely efficient, there are two distinct cases where it can break down. These cases are namely the case of direct DNA damage and indirect DNA damage, which are discussed here.

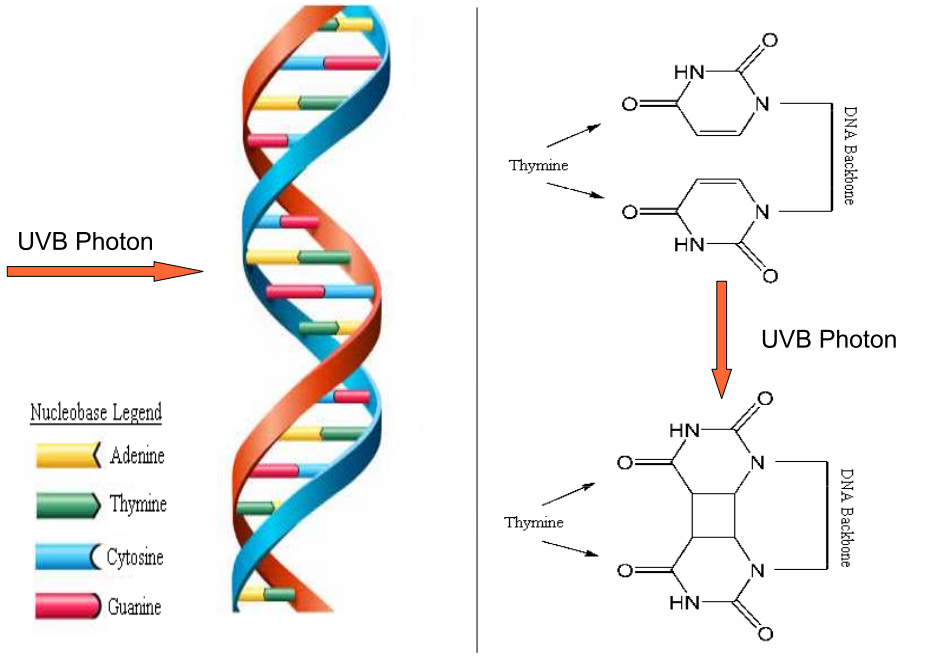

Figure 2.5: *Direct DNA damage caused by a UVB photon*

2.4.1 Direct DNA damage

While DNA can convert the vast majority of incoming photons rapidly into harmless heat energy, there are a small percentage of photons that will get through this evolved defence. When this occurs, an incoming UVB photon is completely absorbed, forcing thymine base pairs in DNA to bond to each other which would not naturally occur. In the case of UVR, this most often results in thymine forming bonds with itself, called a thymine-thymine dimer (Goodsell 2001). These erroneous pairs form lesions in the structure of the DNA, which may be repaired by the mechanism of nucleotide excision repair, but unrepaired dimers can be mutagenic (Whitmore *et al* 2001). This mutagenic DNA can lead to the skin cancer melanoma (Vink and Rosa 2001). This form of cancer is localized to the site of exposure. Direct DNA damage also provokes an increase in melanin production to counteract the damage, so such as a long lasting tan. Over-exposure leads to sunburn (Parrish *et al* 1982). These effects can be considered a painful warning sign of direct DNA damage, but it is worth noting that this mechanism of DNA damage only accounts for 8% of melanomas, the rest being attributable to indirect DNA damage (Davis *et al* 2002).

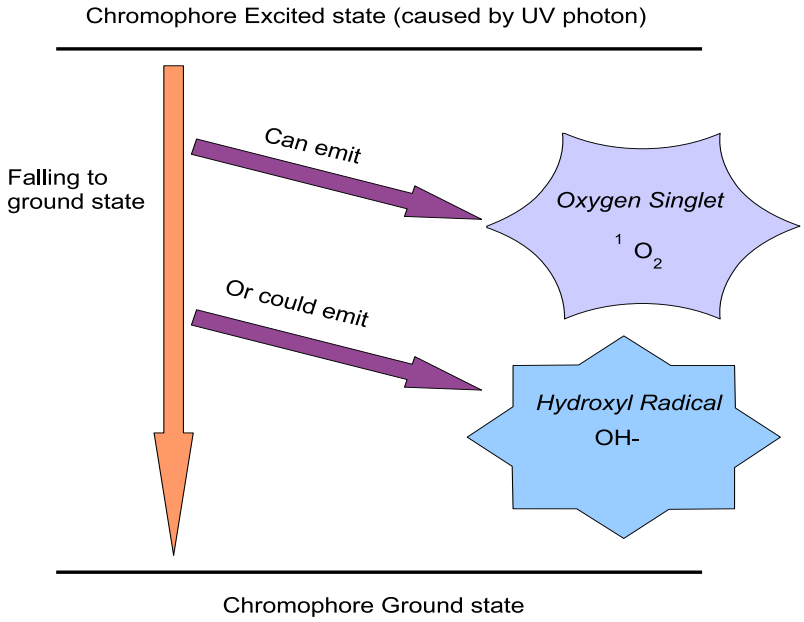

Figure 2.6: *Indirect DNA damage. Produced compounds are highly toxic to DNA.*

2.4.2 Indirect DNA damage

Indirect DNA damage occurs when a UV photon is incident upon a chromophore that cannot quickly reduce the excited molecule to harmless heat and thus has a correspondingly long lifetime, around 10^3 - 10^6 times than that of melanin (Cantrall and MacGarvey 2001). Because of this long excited state, reactions with other molecules can occur. Two processes which can occur are the generation of free radicals and reactive oxygen species, both of which are mutagenic and detrimental to DNA integrity through the mechanism of oxidative stress (Ribeiro *et al* 1991). Indirect DNA damage accounts for 92% of melanomas including the most serious cases of malignant melanoma (Davis *et al* 2002) and unlike direct DNA damage, there is no pain warning. The melanoma can manifest in unexposed sites as free radicals can travel throughout the body. Indirect DNA damage has raised concerns that some of the chemicals in certain sunscreens could contribute to free radical production and hence cellular damage (Moseley *et al* 2007, Xu *et al* 2001, Armeni *et al* 2004). An example reaction is illustrated in figure 2.6 .

2.5 Human epidermis

In humans, the skin is the largest organ, covering essentially the entire body with varying thickness. The outmost layer of the skin is the epidermis (Gray 1984). The thickness of the epidermis varies from a minimum at the eyelids of approximately 0.05mm to a maximum of about 1.5mm on the soles of the feet. The epidermis is of primary interest in phototherapy and the composition of this region is outlined in figure 2.7. The composition, thickness and properties of these layers are determined to a large degree by the rate of mitosis of the the undifferentiated epidermal cells from the basal line. The transformation of these stem cells into different skin cells occurs in various regions of the epidermis (Gray 1984).

Table 2.2: Layers of the Human Epidermis

Epidermal Layer	**Properties of layer**
Stratum germantivum	Also known as basal layer.This layer of cells can be can be considered the stem cells of the epidermis, as they are undifferentiated and proliferate through migrating 'daughter' cells that differentiate into other skin cells as they move through the epidermis. New cells are constantly produced in this layer
Stratum spinosum	Region where epidermal cells form intercellular bridges, giving the region a rough hewn appearance, explaining in part why the terms prickle cell and prickle cell layer are often used to refer to these cells and this region respectively. These prickle cells generate the protein Keratin.
Stratrum granulosum	A granular layer of the epidermis
Stratum lucidum	Penultimate layer of the epidermis composed of layers of dead and flattened keratinocyte cells.
Stratum corneum	Also known as the horny layer. Uppermost layer composed mainly of layers of dead skin cells lacking nuclei. This layer is thickest when the most protection is needed, such as the hands and soles of feet.

Table 2.3: Cells of the Human Epidermis

Cell Type	**Functions of cell type**
Keratinocytes	Synthesizes the protein keratin, accounts for 95% of epidermal cells
Melanocytes	Produce the compound melanin, responsible for skin pigmentation
Langerhan cells	Dendritic (immune system) agents residing mainly in the *stratum spinosum*

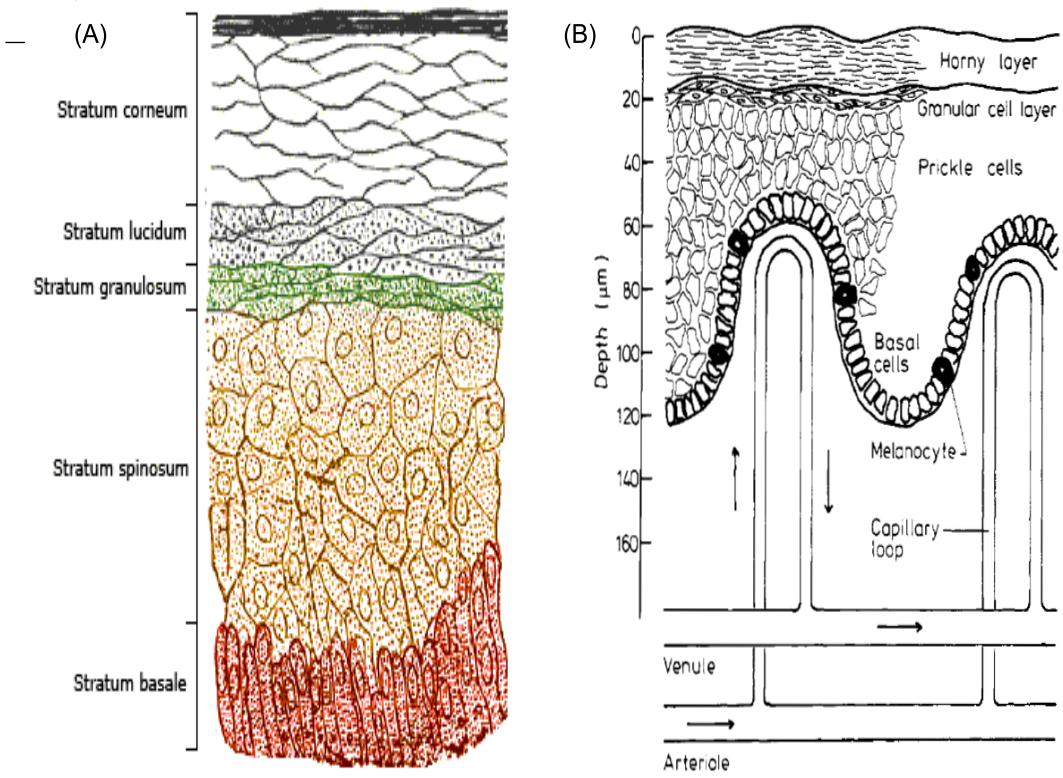

Figure 2.7: *Layers of the epidermis (A) Adapted from Gray's Anatomy 1984 (B) Reproduced from Diffey 1980*

2.5.1 Erythema and melanogenesis

The acute and long term effects of exposure to ultraviolet radiation on human biological tissue are well documented (Diffey 1979). The effect of this exposure is dependant upon both the exposure wavelength and the duration of that exposure. It is important to consider the effects of UVA and UVB wavelength photons in this regard; UVC or germicidal band photons are not used in phototherapy, and even in nature are effectively attenuated to nothing by atmospheric absorption (Gates 1966) so the biological effects of UVC are not considered in UVR therapy.

Erythema is a common consequence of exposure to UVR. It is the reddening of the skin induced by hyperemia (increase in blood flow) of the capillaries in lower skin layers, chiefly the subpapillary venules (Rothman 1954). Erythema can occur with any skin infection, injury or inflammation, but is more readily induced by exposure to ultraviolet light. In the case of relatively long-wave UVA, erythemal effects appear without any latency whereas erythema due to UVB tends to have

a delayed appearance (Kaidbey *et al* 1979). Erythema is often referred to by its colloquial term of sunburn, and is an unwanted side effect of treatment with an improper dose. In more extreme cases, there can be extensive blistering and peeling of epidermal layers (Diffey and Hart 1997). UVB radiation is 100-1000 times more likely to induce an erythemal effect than UVA, this is clear from the CIE relative action spectrum shown in figure 2.8 . It is immediately apparent from observation that UVA radiation is many orders or magnitude less effective at inducing erythemal effects than UVB. An example of an erythemal effect is shown in figure 2.9 A.

UVB exposure also causes the production of vitamin D in skin (Adams *et al* 1982), specifically Vitamin D_3. UVB can also modulate the immune system, depressing dendritic activity and thus inhibiting or otherwise altering immune system responses (Matsumura and Ananthaswamy 2004). It is this property of UVR that may explain in part its beneficial effect on autoimmune disorders. Finally, UVR exposure triggers melanogenesis or darkening of the skin, commonly referred to as tanning. This is discussed in section 2.5.4.

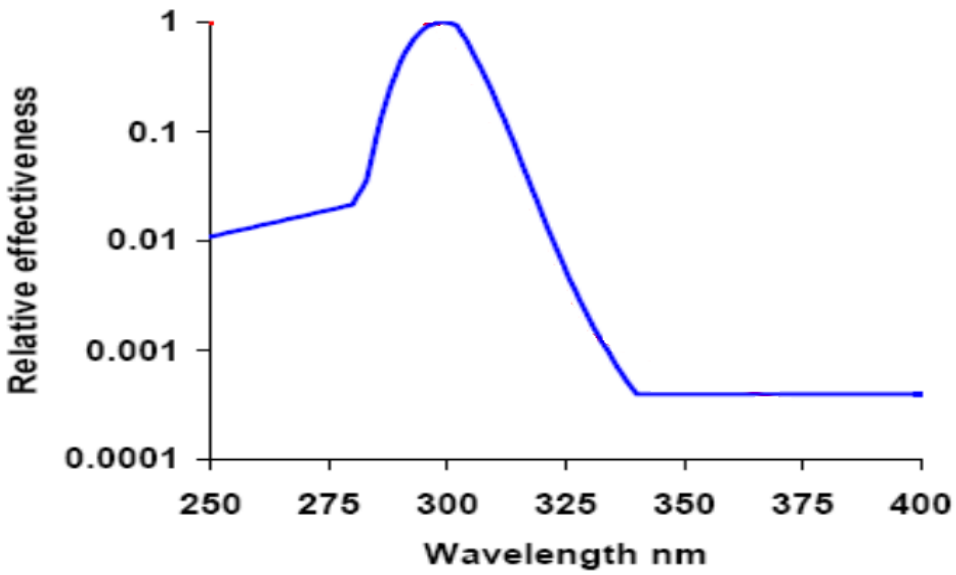

Figure 2.8: *CIE Erythemal Action spectrum (1987)*

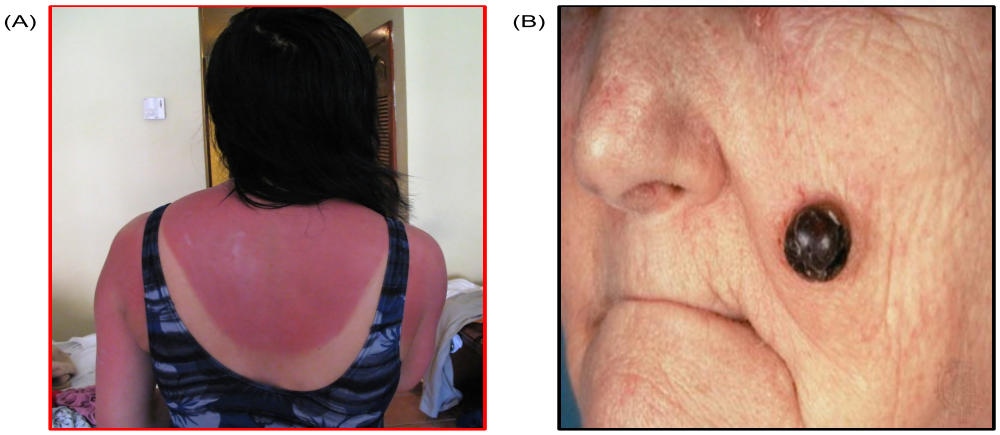

Figure 2.9: *(A) Erythema (B) Malignant Melonoma*

2.5.2 Skin aging

Collagen is the substance in skin which gives it elasticity. Collagen fibrils are located beneath the dermis, and deeply penetrating UVA tends to cause this dermal connective tissue obvious damage. Photo-aged skin is characterized by loss of elasticity, wrinkles, uneven pigmentation, brown spots and a leathery appearance whereas chronologically aged skin without over exposure to UVR is smooth and free of blemishes, though some natural loss of tone and elasticity occurs (Fisher *et al* 1997). Thus, overexposure to UVR photo-ages the skin by damaging collagen and connective dermal tissue.

2.5.3 Carcinogenesis

As the skin absorbs most UVR and this can result in DNA damage, there has been a well documented correlation of certain UVR therapies and skin cancers, particularly PUVA treatments (Stern & Laird 1994, Weischer *et al* 2004). In order of seriousness, UVR treatments have been implicated in basal cell carcinoma, squamous cell carcinoma and malignant melanoma (Diffey and Hart 1997). Current research indicates that UVB treatments are much less likely to be carcinogenic (Studniberg and Weller 1993) than conventional UVA therapies. This may be because indirect DNA damage and the oxygen species it can create are more damaging than direct DNA damage caused by UVB. Indirect DNA damage is synonymous with UVA exposure (Dedon *et al* 1998) and the risk of cancer and carcinogensis must be accounted for in any therapy involving UVR.

2.5.4 Epidermal response and Photoadaptation

The reaction of human skin to UVR is not solely based on the erythemal wavelengths present. The amount of melanin and other chromophores present in the epidermis will influence strongly the amount of reaction that will take place. Skin with more pigment will appear darker, and skin colour can be used to estimate the reaction to UVR. The Fitzpatrick phototyping scale (Fitzpatrick 1975) was developed to help classify skin types based on their appearance and reaction to UVR for predominantly white skin. This scale was later extended to include dark and even black skin (Fitzpatrick 1988). This scale is still in usage and is outlined in table 2.4 . The Fitzpatrick scale is often used by phototherapists to estimate starting dose. The minimal erythemal dose (MED) is the minimum dose required to observe an erythemal effect.

Table 2.4: Fitzpatrick Phototype scale (adapted *Dermatology*)

Type	**UVR response**	**Skin colour**	**UVA MED**	**UVB MED**
I	Burns easily / Never tans	Ivory White	20 - 35 mj/cm^2	15 - 30 mj/cm^2
II	Burns easily / Tans little	White	30 - 45 mj/cm^2	25 - 40 mj/cm^2
III	Burns moderately / Often tans	White	40 - 55 mj/cm^2	30 - 50 mj/cm^2
IV	Burns minimally / Tans easily	Olive	50 - 80 mj/cm^2	40 - 60 mj/cm^2
V	Burns rarely / Tans profusely	Brown	70 - 100 mj/cm^2	60 - 90 mj/cm^2
VI	Never burns / Trans profusely	Black	100 mj/cm^2	90 - 150 mj/cm^2

Photoadaptation is a trait of skin to respond to UVR irradiation by changing in such a way that future equivalent doses of such radiation have a diminished response (Oh *et al* 2004). While these processes are poorly understood, it has implications for UVR phototherapy in so much as a constant dose seems less than optimum. Before undergoing phototherapy, the Fitzpatrick scale gives an indication of the tolerance of the skin to UVR, and this is useful in determining a starting dose. However it has been shown that doses close to the erythemal dose are most effective (Hofer *et al* 1998) so in practice the dose has to be increased in subsequent sessions. A general rule of thumb used is the 70/20 rule; begin at 70% of MED and increase by 20% each sucessive treatment. This seems to work well for all skin types, as evidence suggests that regardless of skin type, patients adapt approximately equally per physical unit of UVR (Palmer *et al* 2006). In essence,

human skin adapts to increasing amounts of UVR by increasing production of melanin and other chromophores. This process is called melanogensis and it triggers tanning in human skin.

2.6 Human eyes

Over-exposure to UVR can be quite detrimental to the human eye. The negative effects can include ocular damage such as photokeratisis (snow blindness) with acute exposure and cataracts from chronic exposure (Sliney 2007). Photokeratisis is an inflammation of the cornea with symptoms including severe pain and visual incapacitation. Conjunctivitis can also occur due to UVR exposure; it is an inflammation of the eyelid membranes characterized by various degrees of photophobia (light aversion), blepharospasm (eyelid muscle spasm), lacrimation (tear shedding) and erythema of eyelid skin (Diffey and Hart 1997). In cases of chronic exposure to UVR, a cataract can occur. This is the complete loss of transparency in the eye lens, resulting in reduced vision or blindness. Unlike the epidermis, the human eye does not photoadapt and consequently has less of a protection mechanism.

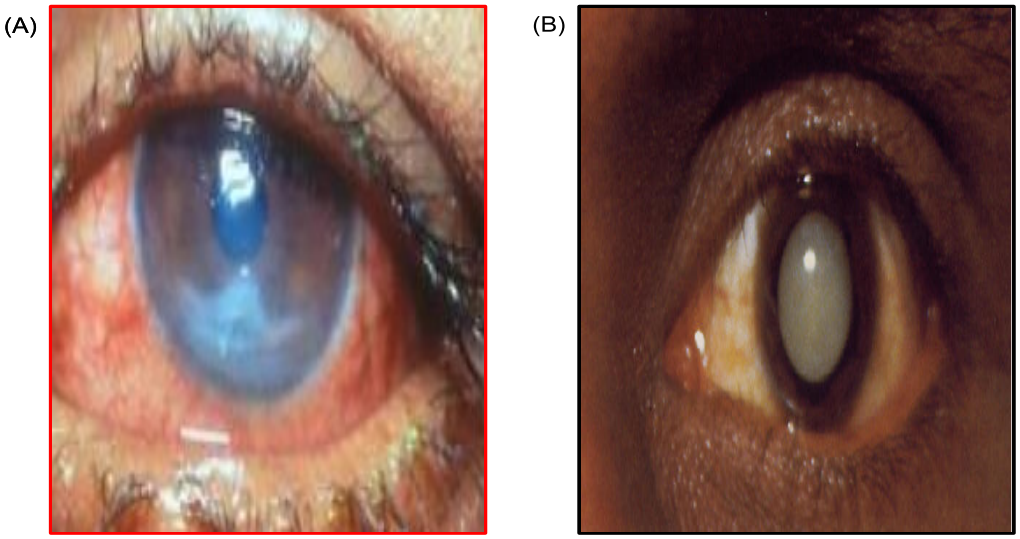

Figure 2.10: *(A) Photokeratisis (B) Cataract*

2.7 UVR Therapy and treatments

While it is apparent that UVR has many unpleasant biological effects and can act as a mutagen, this very property of biological effectiveness can be be used as treatment for several types of skin disorder. Ultraviolet therapies for these complaints can use many different spectral power distributions for different applications, but most commonly encountered treatments are narrow-band UVB centred around 311nm or broad-band UVA in conjunction with the skin photosensitizing agent psolaren, referred to as PUVA treatment.

2.7.1 Psoriasis

Psoriasis is a very common chronic non-infectious disease of the skin, resulting in raised patches on the skin known as psoriatic plaques. These plaques are the result of hyper prolific production of keratinocytes in the basal layer, resulting in regions with an abundance of skin cells and this appearance. Psoriasis is highly idiosyncratic and can manifest in a variety of ways, some of which are illustrated in figure 2.11. Diagnosis is usually made by dermatological examination. While the exact causes of psoriasis are not fully understood, the currently accepted theory is that psoriasis is an autoimmune disease (Vladimarsson *et al* 1995, Baker *et al* 1984, Barker 1997) where T-cells from the immune system react with cells in the epidermis to stimulate abnormally high production of keratinocyte cells. There is also evidence that various types of interleukin (an immune signal protein) can stimulate overproduction of these cells and the inflammation associated with psoriasis (Grossman *et al* 1989, Zheng *et al* 2007). There is also a strong genetic component, related again to immune issues (O'Nestle *et al* 2009). This may in part explain why UVR therapies excel at clearing psoriasis, as UVR can reduce the number of dendritic immune cells (O'Nestle *et al* 2009, Ozawa *et al* 1999) and reduce the activity of these cells (Schmitt and Ullrich 2000). Psoriasis is the most common disorder treated with UVR and comprises the bulk of UVR phototherapy cases.

Figure 2.11: *Common types of psoriasis; Plaque or* psoriasis vulgaris *is the most common form, presenting as raised plaques. Flextural psoriasis or inverse psoriasis presents on skin folds. Guttate psoriasis are teardrop shaped legions. Pustular psoriasis presents are raised bumps filled with non-infectious pus.*

The mechanism of action aside, UVR phototherapy is highly beneficial for patients suffering from this disease, and both PUVA and NB-UVB are widely used to induce remission (Green *et al* 1992). In clinical trials, PUVA has been show to be more effective at causing remission of psoriasis versus NB-UVB, as shown in table 2.5.

Table 2.5: Clearance of psoriasis with PUVA & NB-UVB

Study	**Psoriasis type**	**Clearance PUVA**	**Clearance NB-UVB**
Gordon et al 1999	Plaque	84%	63%
Yones & Garibaldinos 2006	Plaque	84%	65%
Sezar et al 2007	Palmoplantar	85%	61%

In addition to this, PUVA also seems to have the advantage of delaying the return of psoriatic plaques (Gordon *et al* 1999) though with potentially more risk of carcinogenesis. In at least one study, NB-UVB used three times weekly were found to be statistically no different in effectiveness or remission length than PUVA used twice weekly for chronic plaque psoriasis (Markham *et al* 2003). In general, clinics will only use PUVA if NB-UVB has failed as aside from the higher cancer risk, the use of psolaren can make the patient hypersensitive to light and can be phototoxic in some cases.

2.7.2 Vitiligo

Vitiligo is the depigmentation of the skin caused by the death of melanocytes, the cells responsible for producing melanin. The reason why this occurs isn't clear, but autoimmune reactions are suspected and there is evidence for this point of view. PUVA and NB-UVB have both been used successfully in re-pigmentation; a study by Bhatnagar (2006) found NB-UVB treatments to be more effective than PUVA for this condition, being successful in 67.57% of cases versus 54.2% of cases for PUVA where traditionally treatment resistant sites such as hands and feet were not considered. It should be noted that patients with this condition have a much greater tendency to erythemal effects due to the decreased level of pigment.

2.7.3 Eczema

Eczema is a form of dermatitis (inflammation of the skin). For chronic eczema, UVR treatments can provide some clearance and reduction in severity (Grundmann-Kollmann *et al* 1999, Reynolds *et al* 2001). Both PUVA and NB-UVB are effective, and equally capable of reducing conditions like chronic hand eczema which is resistant to other forms of treatment (Sezar and Etikan 2007).

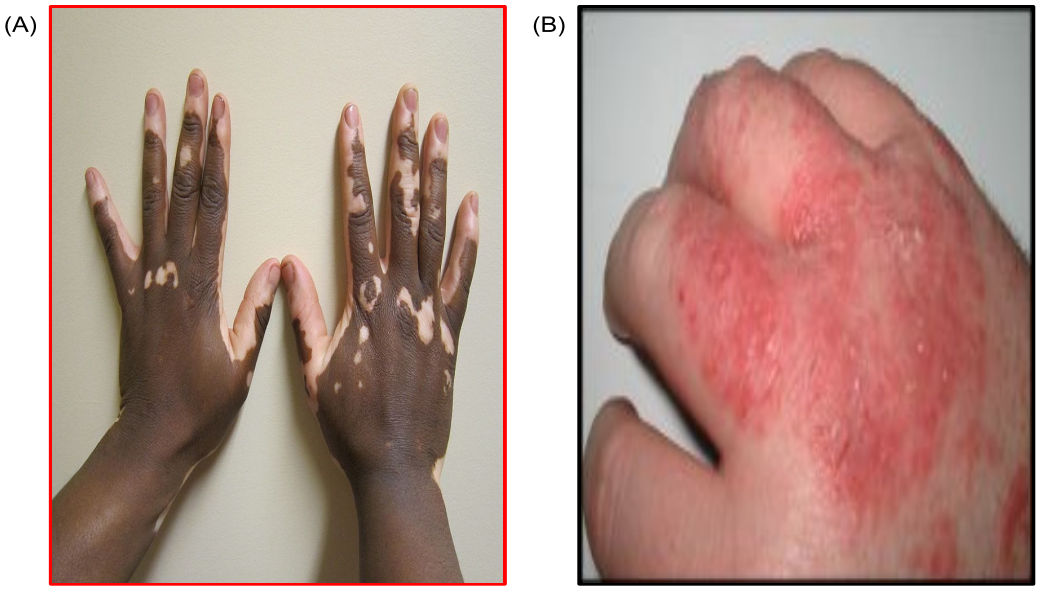

Figure 2.12: *(A) Vitiligo in a dark skinned individual (B) Infant Eczema*

2.7.4 Polymorphic light eruption

Polymorphic light eruption (PMLE) is a condition where the skin becomes hypersensitive and reacts to UVR in sunlight. These reactions can take the form of hive-like skin irritations. At first glance it may seem contradictory that a condition triggered by UVR exposure may also be treated with the very element that triggers the reaction but indeed both PUVA and NB-UVB therapies have been proven to be effective treatment in stubborn cases. Whether this is due to some photoadaptive mechanism or the immunomodulatory nature of UVR is not clear, but despite the seemingly contradictory nature of the mechanism of action, the effectiveness of the treatment is not in doubt. (Hönigsmann 2008).

2.7.5 Other disorders treated with UVR

Perforating dermatosis or acquired perforating dermatosis (APD) is a condition where papules appear on the epidermis due to keratotic activity, usually around the follicles. While this condition can occur on its own, it has high correlation with diabetics and those suffering chronic renal failure. UVR therapy can offer some hope in achieving remission, particularly NB-UVB treatments (Ohe *et al* 2004).

Lichen Planus is a disease of the skin and mucus membranes in the mouth which results in raised papules. The name itself may be a misnomer has it has no relation to lichens but rather describes the appearance of the growths on skin. NB-UVB therapy has shown some clinical effectiveness is reducing this affliction; A study (Pavlotsky *et al* 2007) found complete remission in 70% of patients treated with broad-band UVB and 85% of patients treated with NB-UVB. Another study contrasting PUVA and NB-UVB (Wackernagal *et al* 2007) found all 100% of patients treated with PUVA had a complete or partial response versus 77% of those treated with NB-UVB. The remission time and treatment duration for both UVR therapies was approximately the same.

Another condition which has been successfully treated with UVR is Mycosis fungoides. Directly translated, Mycosis fungoides (MF) roughly means "mushroom like fungal disease". This is misleading, as it is in no way a fungal infection. More correctly is it a type of Non-Hodgkin lymphoma, known as cutaneous T-cell lymphoma (CTCL). In this cancer, T-cells in the immune system become malignant and migrate to the epidermal surface, resulting in the appearance of lesions. The lymphoma can go into remission with treatment, remain stable and non-progressive or progress and infect other systems. As MF can be confused with psoriasis or eczema, a biopsy must be performed to confirm diagnosis. Table 2.6 shows the results from a clinical study (Diederen *et al* 2003) indicating strongly that the ideal treatment modality for MF appears to be NB-UVB rather than PUVA.

Table 2.6: Clearance of MF with PUVA & NB-UVB

Treatment	**Complete Remission**	**Partial Remission**	**Remission Time**
NB-UVB	81%	19%	24.5 months
PUVA	71%	29%	22.8 months

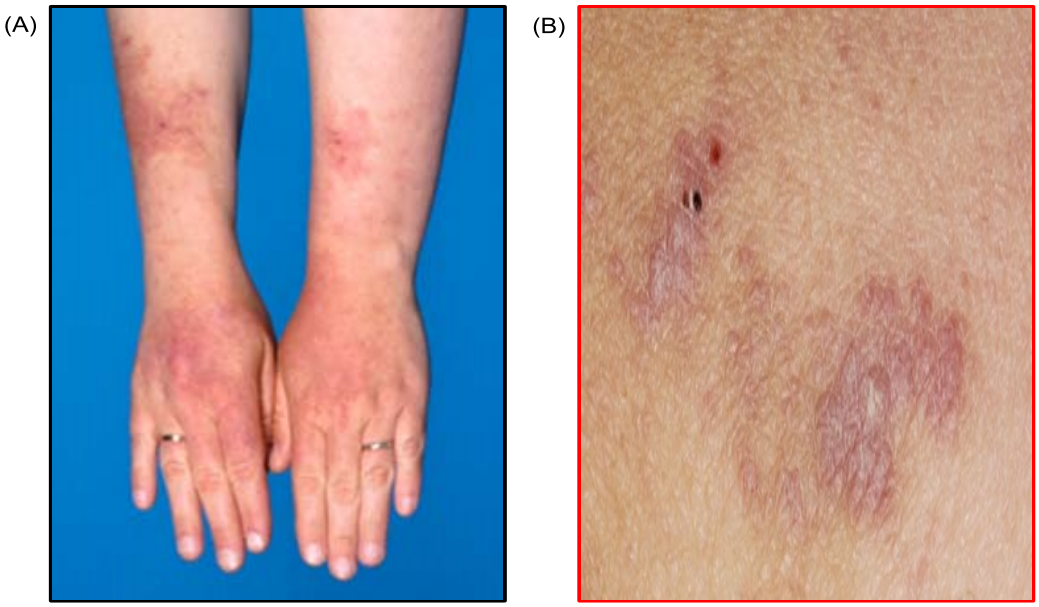

Figure 2.13: *(A) PMLE manifesting on the arms (B) Lichen Planus*

2.8 Exposure Limits

Recommended exposure limits for general and occupational UVR exposure were set by IRPA (1985,1989) based on wavelength. For UVA wavelengths (315 - 400nm) the total irradiance incident upon unprotected eye / skin should not exceed $10kJ/m^2$ over an 8 hour period and the total radiation exposure (EL) should not exceed the values in table 2.7. For UVB and UVC the exposure should not exceed the values in table 2.7 in an 8 hour period either. The irradiance of a broadband source (E_{eff}) is weighted against the spectral peak of 270nm and can be calculated by the weighing formula

$$E_{eff} = \Sigma E(\lambda)S(\lambda)\Delta\lambda \tag{2.2}$$

where $E(\lambda)$ is the spectral irradiance in units of W/m^2nm, $S(\lambda)$ is the unitless relative spectral effectiveness and $\Delta\lambda$ is the bandwidth of the measurement intervals. The limits are calculated for entirely unprotected exposure to UVR sources. Obviously patients in treatment will far exceed these levels. The permissible exposure time $t(\lambda)$ in seconds for actinic (UVB and UVC spectrum) emissions can be calculated from the exposure values at 270nm by

$$t(\lambda) = \frac{30J/m^2}{E_{eff}} \tag{2.3}$$

Table 2.7: IRPA UVR Limits

$\lambda(nm)$	$EL(J/m^2)$	$S(\lambda)$	$\lambda(nm)$	$EL(J/m^2)$	$S(\lambda)$
180	2500	0.012	310	2000	0.015
190	1600	0.019	313	5000	0.006
200	1000	0.030	315	1.0×10^4	0.003
205	590	0.051	316	1.3×10^4	0.0024
210	400	0.075	317	1.5×10^4	0.002
215	320	0.095	318	1.9×10^4	0.0016
220	250	0.120	319	2.5×10^4	0.0012
225	200	0.150	320	2.9×10^4	0.0010
230	160	0.190	322	4.5×10^4	0.00067
235	130	0.240	323	5.6×10^4	0.00054
240	100	0.300	325	6.0×10^4	0.0005
245	83	0.360	328	6.8×10^4	0.00044
250	70	0.430	330	7.3×10^4	0.00041
254	60	0.500	333	8.1×10^4	0.00037
255	58	0.520	335	8.8×10^4	0.00034
260	46	0.650	340	1.1×10^5	0.00028
265	37	0.810	345	1.3×10^5	0.00024
270	30	1.000	350	1.5×10^5	0.00020
275	31	0.960	355	1.9×10^5	0.00016
280	34	0.880	360	2.3×10^5	0.00013
285	39	0.770	365	2.7×10^5	0.00011
290	47	0.640	370	3.2×10^5	0.000093
295	56	0.540	375	3.9×10^5	0.000077
297	65	0.460	380	4.7×10^5	0.000064
300	100	0.300	385	5.7×10^5	0.000053
303	250	0.190	390	6.8×10^5	0.000044
305	500	0.060	395	8.3×10^5	0.000036
308	1200	0.026	400	1.0×10^6	0.000030

2.9 Conclusions

UVR phototherapy provides much benefit to patients suffering from a variety of skin complaints but care must be taken to ensure an adequate and biologically effective dose is administered. The ideal dose for treatments is close to the erythemal dose, and going above this results in patient burning. Going too far below this leads to a biologically ineffectual dose incident upon the patient. This leads to the conclusion that any methods to improve dosimetry in UVR phototherapy would be of great benefit to the treatment of these patients.

2.10 References

- Adams JS, Clemens TL, Parrish JA and Holick MF 1982 Vitamin-D synthesis and metabolism after ultraviolet irradiation of normal and vitamin-D-deficient subjects *New. Engl. J. Med.* **306** 722- 725
- Armeni T, Damiani E, Battino M, Greci L, Principato G 2004 Lack of in vitro protection by a common sunscreen ingredient on UVA-induced cytotoxicity in keratinocytes *Toxicology* 165 - 178
- Baker BS, Swain AF, Fry L and Valdimorsson 1984 Epidermal T lymphocytes and HLA-DR expression in psoriasis *Brit. J. Dermatol.* **110** 555-564
- Barker JNWN 1997 Immunology of psoriasis *JEADV* **9** 71-72
- Bhatnagar A, Kanwar AJ, Parsad D and De D 2007 Comparison of systemic PUVA and NB-UVB in the treatment of vitiligo: an open prospective study *JEADV* **21** 638-642
- Cantrall A and MacGarvey D 2001 *Sun Protection in Man.* Canada: Comprehensive Series in Photosciences
- Commission Internationale de IEclairage (CIE) 1970 *International Lighting Vocabulary 3rd ed* (Paris)

- CIE 69, 1987 *Methods of Characterizing Illuminance Meters and Luminance Meters: Performance, Characteristics and Specifications* (Vienna: Commission Internationale de lEclairage)

- Davies H, Bignell GR, Cox C, Stephens P, Edkins S, Clegg S, Teague J, Woffendin H, Garnett MJ, Bottomley W, Davis N, Dicks E, Ewing R, Floyd Y, Gray K, Hall S, Hawes R, Hughes J, Kosmidou V, Menzies A, Mould C, Parker A, Stevens C, Watt S, Hooper S, Wilson R, Jayatilake H, Gusterson BA, Cooper C, Shipley J, Hargrave D, Pritchard-Jones K, Maitland N, Chenevix-Trench G, Riggins GJ, Bigner DD, Palmieri G, Cossu A, Flanagan A, Nicholson A, Ho JWC, Leung SY, Yuen ST, Weber BL, Seigler HF, Darrow TL, Paterson H, Marais R, Marshall CJ, Wooster R, Stratton MR and Futreal PA 2002 Mutations of the BRAF gene in human cancer *Nature* **417** 949 - 954

- Dedon PC, Plastaras JP, Rouzer CA and Marnett LJ 1998 Indirect mutagenesis by oxidative DNA damage: Formation of the pyrimidopurinone adduct of deoxyguanosine by base propenal *Proc. Natl. Acad. Sci. USA* **95** 1111311116

- Diederen PVMM, Van Weelden H, Sanders CJG, Tooshra J and Van Vloten WA 2003 Narrowband UVB and psoralen-UVA in the treatment of early-stage mycosis fungoides: A retrospective study *J. Am. Acad. Dermatol.* **48** 215-219

- Diffey BL, Tate TJ and Davis A 1979 Solar dosimetry of the face: the relationship of natural ultraviolet radiation exposure to basal cell carcinoma localisation *Phys. Med. Biol.* **24** 931-939

- Diffey BL 1980 Ultraviolet radiation physics and the skin *Phys. Med. Biol.* **25** 405-426

- Diffey BL and Hart G 1997 *Ultraviolet and Blue-Light Phototherapy - Principles, Sources, Dosimetry and safety.* York: IPEM

- Diffey BL 2002 What is light ? *Photodermatol. Photoimmunol. Photomed.* **18** 68-74
- Fisher GJ, Wang ZQ, Datta SC, Varani J, Kang S and Voorhees JJ 1997 Pathophysiology of premature skin aging induced by ultraviolet light *New. Engl. J. Med.* **337** 1419 - 1428
- Fitzpatrick TB 1975 Soleil et peau *J. Med. Esthet.* **2** 3334
- Fitzpatrick TB 1988 The validity and practicality of sun-reactive skin types I through VI. *Arch. Dermatol.* **124** 869871
- Gates DM 1966 Spectral Distribution of Solar Radiation at the Earth's Surface *Science* **151** 525-529
- Goodsell DS 2001 The Molecular Perspective: Ultraviolet Light and Pyrimidine Dimers *The Oncologist* **6** 298-299
- Gordon PM, Diffey BL, Matthews JNS and Farr PM 1999 A randomized comparison of narrow-bandTL-01 phototherapy and PUVA photochemotherapy for psoriasis *J. Am. Acad. Dermatol.* **41** 728-732
- Gray's Anatomy *Grays Anatomy (30th ed.).* eds: CD Clemente (Philadelphia: Lea and Febiger)
- Green C, Diffey B L, and Hawk J L M 1992 Ultraviolet Radiation in the treatment of Skin disease *Phys. Med. Biol.* **37** 1-20
- Grossman RM, Krueger J, Yourish D, Granelli-Piperno A, Murphy DP, May LT, Kupper TS, Sehgal PB and Gottlieb AB 1989 Interleukin 6 is expressed in high levels in psoriatic skin and stimulates proliferation of cultured human keratinocytes *Proc. Nati. Acad. Sci. USA* **86** 6367-6371,
- Grundmann-Kollmann M, Behrens S, Podda M, Peter RU, Kaufmann R and Kerscher M 1999 Phototherapy for atopic eczema with narrow-band UVB *Am. Acad. Dermatol.* **40** 995-997

- Hofer, Fink-Punches, Kerl and Wolf 1998 Comparison of phototherapy with near vs. far erythemogenic doses of narrow-band ultraviolet B in patients with psoriasis *Brit. J. Dermatol.* **138** 96-100
- Hönigsmann H 2008 Polymorphous light eruption *Photodermatol. Photo.* **24** 155161
- IRPA 1985 Guidelines on limits of exposure to Ultraviolet radiation of wavelengths between 180nm and 400nm (incoherent optical radiation) *Health Phys.* **49** 331-340
- IRPA 1989 Proposed change to the IRPA 1985 guidelines on limits of exposure to Ultraviolet radiation *Health Phys.* **56** 971-972
- Kaidbey K H and Kligman A M 1978 The acute effects of Long-wave Ultraviolet radiation on Human Skin *Int. J. Dermatol.* **72** 253-256
- Markham T, Rogers S and Collins P 2003 Narrowband UV-B (TL-01) Phototherapy vs Oral 8-Methoxypsoralen PsoralenUV-A for the Treatment of Chronic Plaque Psoriasis *Arch. Dermatol.* **139** 325 - 328
- Matsuma Y and Ananthaswamy HN 2004 Toxic effects of ultraviolet radiation on the skin *Toxicol. Appl. Pharm.* **195** 298 - 308
- Meredith P and Riesz J 2004 Radiative Relaxation Quantum Yields for Synthetic Eumelanin *J. Photochem. Photobiol. A.* **79** 211 - 216
- Moseley CN, Wang L, Gilley S, Wang S and Yu H 2007 Light-Induced Cytotoxicity and Genotoxicity of a Sunscreen Agent, 2-Phenylbenzimidazole in Salmonella typhimurium TA 102 and HaCaT Keratinocytes *Int. J. Environ. Res. Public Health* **4(2)** 126-131
- Moseley H 1988 *Non-ionising radiation : microwaves, ultraviolet and laser radiation* (Bristol : Hilger)
- Murdoch 1985 *Illumination engineering - from Edison's lamp to the laser* New York : London : Macmillan Pub. Co ; Collier Macmillan Publishers

- Ohe S, Danno K, Sasaki H, Isei T, Okamoto H and Horio T 2004 Treatment of acquired perforating dermatosis with narrowband ultraviolet B *Am. Acad. Dermatol.* **50** 892-894

- Ozawa M, Ferenczi K, Kikuchi T, Cardinale I, Austin LM, Coven TR, Burack LH and Krueger JG 312-nanometer Ultraviolet B Light (Narrow-Band UVB) Induces Apoptosis of T Cells within Psoriatic Lesions *JEM* **189** 711-718

- O'Nestle F, Kaplan DH and Barker J 2009 Mechanisms of Disease: Psoriasis *New. Engl. J. Med.* **361** 496- 509

- Palmer RA, Aquilina S, Milligan PJ, Walker SL, Hawk JLM and Young AR 2006 Photoadaptation during Narrowband Ultraviolet-B Therapy Is Independent of Skin Type: A Study of 352 Patients *J. Invest. Deramtol.* **126** 1256 - 1263

- Parrish JA, Jaenicke KF and Anderson RR 1982 Erythema and melanogenesis action spectra of normal human skin *Photochem. Photobiol.* **36** 187-191

- Pavlotsky F, Nathansohn N, Kriger G, Shpiro D and Trau H Ultraviolet-B treatment for cutaneous lichen planus: our experience with 50 patients *Photodermatol. Photo.* **24** 83-86

- Reynolds N J, Franklin V, Gray J C, Diffey B L and Farr P M 2001 Narrow-band Ultraviolet B and broad-band ultraviolet A phototherapy in adult atopic eczema; A randomised controlled trial *Lancet* **357** 2012 - 2016

- Ribeiro DT, Madzak C, Sarasin A, Di Mascio P, Sies H and Menck CFM 1991 Singlet oxygen induced DNA damage and mutagenicity in a single-stranded SV40-based shuttle vector *Photochem. Photobiol.* **55** 39-45

- Schmitt DA and Ullrich SE 2000 Exposure to Ultraviolet Radiation Causes Dendritic Cells/Macrophages to Secrete Immune-Suppressive IL-12p40 Homodimers *J. Immunol.* **165** 3162-3167.

- Sezar E and Etikan I 2007 Local narrowband UVB phototherapy vs. local PUVA in the treatment of chronic hand eczema *Photodermatol. Photoimmunol. Photomed.* **23** 1014

- Sezar E, Erbil AH, Kurumlu Z, Tastan HB and Etikan I 2007 Comparison of the efficacy of local narrowband ultraviolet B (NB-UVB) phototherapy versus psoralen plus ultraviolet A (PUVA) paint for palmoplantar psoriasis *J.Dermatol.* **34** 435440

- Sliney D H, 1997 Ultraviolet radiation effects upon the eye: Problems of dosimetry *Radiat. Prot. Dosim.* **72** 197 - 206

- Stern RS and Laird N 1994 The Carcinogenic Risk of Treatments for Severe Psoriasis *Cancer* **73** 2759 - 2764

- Studniberg HM and Weller P 1993 PUVA, UVB, psoriasis and nonmelanoma skin cancer *J. Am. Acad. Dermatol.* **29** 1013-1022

- Valdimarsson H, Baker BS, Jónsdóttir I, Powles A and Fry L 1995 Psoriasis: a T-cell-mediated autoimmune disease induced by streptococcal superantigens? *Immunol. Today* **16** 145 - 149

- Vink AA and Roza L 2001 Biological consequences of cyclobutane pyrimidine dimers *J. Photochem. Photobiol. B.* **65** 101 - 104

- Wackernagel A, Legat FJ, Hofer A, Quehenberger F, Kerl H and Wolf F 2007 Psoralen plus UVA vs. UVB-311 nm for the treatment of lichen planus *Photodermatol. Photoimmunol. Photomed* **23** 1519

- Weischer M, Blum A, Eberhard F, Röcken M and Berneberg M 2004 No Evidence for Increased Skin Cancer Risk in Psoriasis Patients Treated with Broadband or Narrowband UVB Phototherapy: A First Retrospective Study *Acta. Derm. Venereol.* **84** 370374

- Whitmore SE, Potten CS, Chadwick CA, Strickland PT, Morison WL 2001 Effect of photoreactivating light on UV radiation-induced alterations in human skin *Photodermatol. Photoimmunol. Photomed* **17** 213217

- Xu C, Green A, Parisi A and Parsons PG 2001 Photosensitization of the Sunscreen Octyl p-Dimethylaminobenzoate by UVA in Human Melanocytes but not in Keratinocytes *Photochem. Photobiol.* **73** 600-604

- Yones SS, Palmer RA, Garibaldinos TT and Hawk JLM 2006 Randomized Double-blind Trial of the Treatment of Chronic Plaque Psoriasis *Arch. Dermatol.* **142** 836-842

- Zheng Y, Danilenko DM, Valdez P, Kasman I, Eastham-Anderson J, Wu J and Ouyang W 2007 Interleukin-22, a TH17 cytokine, mediates IL-23-induced dermal inflammation and acanthosis *Nature* **445** 648 - 651

Chapter 3

Clinical ultraviolet phototherapy

Having established the biological and theraputic effectiveness of ultraviolet radiation treatments, it is important to examine how these solutions are implemented in clinical practice.

3.1 Phototherapy Cabins

A phototherapy cabin is a free standing structure designed to surround the patient and provide approximately equal irradiance to all body sites during treatment. As skin disorders such as psoriasis can affect a large area of epidermis, the use of UV cabins is widespread. There are an abundance of different designs available from numerous manufacturers. In general, cabins consist of multiple fluorescent lamps with their associated ballasts mounted in front of mirrors, where a patient stands at the cabin centre. Cabins tend to be electrically cooled to keep the lamps at optimum operating temperature and there is usually a grill or UVR transparent plastic safety sheet between the patient and the lamps to reduce the potential of an accident. Various models of Waldmann cabin are most frequently encountered in phototherapy centres across Europe, and other manufacturers include Dixwell, National Biological and Daavlin. There is much variation in size, number of tubes and reflector placement but the essential premise of the UVR cabin is to direct this bandwidth of radiation upon the patient epidermis. Some cabin designs are shown in figure 3.1

Figure 3.1: *(A) Waldmann UV-5040 (B) National Biological Houva III (C) Waldmann UV-1000*

Different cabins have different geometries and varying number of tubes (Amatiello and Martin 2006); Some common arrangements of tube placement inside various cabins are shown in figure 3.2 for the some common units.

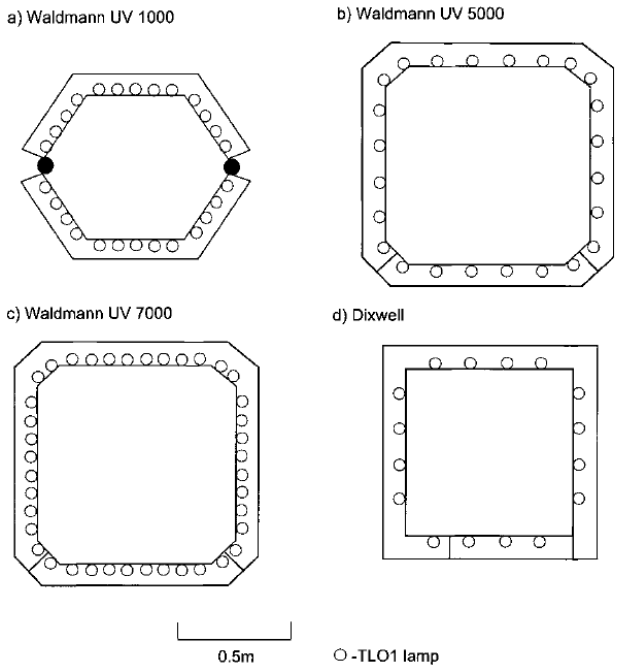

Figure 3.2: *Tube placement of various different cabins. Reprinted from Currie* et al *2000*

3.1.1 Ultraviolet lamps

Depending on the particular condition being treated and the severity of that condition, a wide variety of UV lamp with varying spectral power can be employed in the cabin. The most common of which are UV lamps from Phillips or versions of these lamps by other manufactures. The principle of operation of these lamps have been discussed in chapter 1. These lamps tend to be between 1.7m and 2m long for use in full body cabinets where they are usually mounted in front of reflectors to maximize the irradiance on the patient. The dimensions of the lamps commonly encountered are depicted in figure 3.3.

Type	A max	B min	B max	C max	D max
Philips TL 20W /01	589.8	594.5	596.9	604	40.5
Philips TL 40W/01	1199.4	1204.1	1206.5	1213.6	40.5
Philips TL 100W /01-F71 RDC	1763.8	1768.5	1770.9	1778	40.5
Philips TL 100W /01-F72 RDC	1755.7	1760.4	1762.8	1774.1	40.5
Philips TL 120W/01	2000	2004.7	2007.1	2014.2	40.5
Philips TL 20W /12	589.8	594.5	596.9	604	40.5
Philips TL 40W /12	1199.4	1204.1	1206.5	1213.6	40.5
Philips TL 100W /12	1763.8	1768.5	1770.9	1778	40.5
Philips TL 20W /52	589.8	594.5	596.9	604	40.5
Philips TLD 20W/09	437.4	442.1	444.5	451.6	28
Philips TL 100W/209	1763.8	1768.5	1770.9	1778	40.5
Philips TL 100W/209-R	1763.8	1768.5	1770.9	1778	40.5
Philips TL 100W /10 R	1763.8	1768.5	1778	1778	40.5

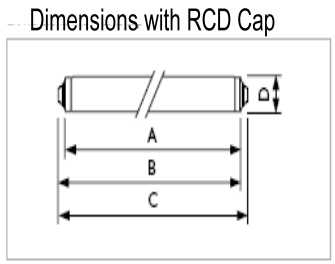

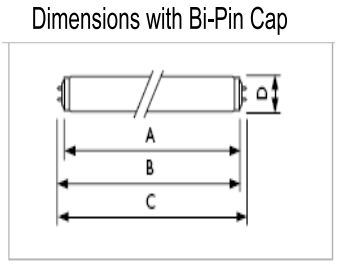

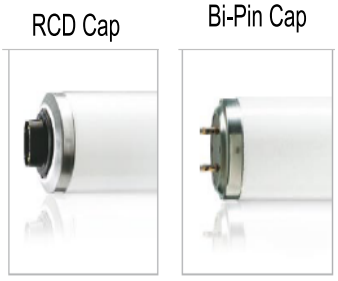

Figure 3.3: *Various UV tube dimensions from Phillips 2007*

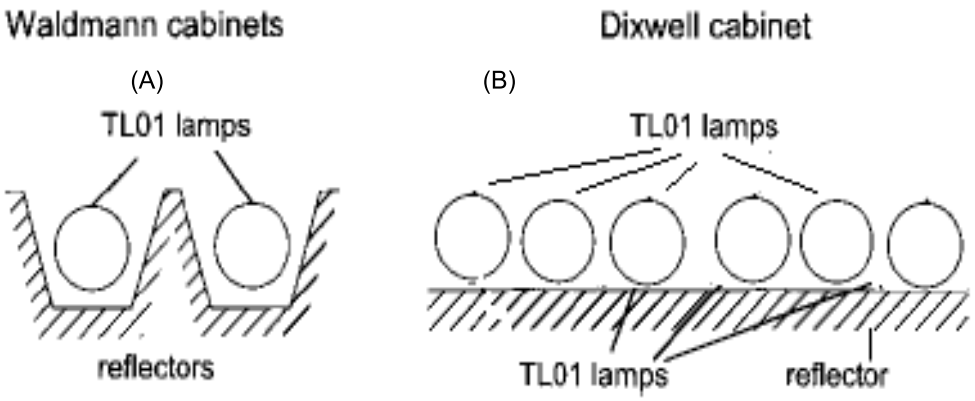

Figure 3.4: *(A) Waldmann mirror arrangement (B) Dixwell mirror arrangement. Reproduced from Currie* et al *2000*

3.1.2 Reflectors

Reflectors are usually mounted behind or around the UVR lamps to direct more light onto the patient epidermis. Like photocabins themselves, there is much variation in how these mirrors are designed and where they are placed. Figure 3.4 depicts two frequent situations; in (a) the mirror surrounds the tube and consists of three pieces of highly reflective coated aluminium. In (b) the coated aluminium is placed just behind the tube and does not surround it. Waldmann cabins tend to use the former arrangement while Dixwell and National biological the latter. The metal sheets used as mirrors are aluminium; aluminium has a reflectivity in the wavelength band of interest (300-400nm) of about 92% (Bartl and Baranak 2004) as shown in figure 3.5. The aluminium can be further coated with a film to change this or protect the aluminium, and common anodized aluminium coating (Coilzak) is often used for this purpose (Phillips 1983).

3.1.2.1 Optical properties of aluminium reflectors

As the metal used in reflectors tends to be aluminium, it is important to examine the properties of this metal and define the quantities used. The defining feature of conductive media (non dielectric) is the presence of free electrical charges in those media. In the case of metals, these charges are electrons, and the motion of electrons constitutes a current. In dielectric media the conductivity, σ, is zero. But for conductors such as metals the situation is quite different. In general, the conductivity of a metal, σ_m, is given by

$$\sigma_m > 0 \tag{3.1}$$

This means that the simple solutions to the Fresnel equations need to be modified to deal with such cases. In fact, it can be shown that the re-formalisation for such cases requires a complex refractive index (Hecht 2002) such that

$$\tilde{n} = n_R - in_I \tag{3.2}$$

where the real and imaginary indices n_R and n_I are both real numbers. As the wave propagates through the metal, it can be shown that its amplitude is exponentially attenuated. The irradiance a distance y into the conductive medium can be expressed as

$$I(y) = I_O \exp[-\alpha y] \tag{3.3}$$

where I_O is the irradiance at the boundary of the metal and α is the attenuation coefficient given by

$$\alpha = \frac{2\omega n_I}{c} \tag{3.4}$$

where is ω the angular temporal frequency or $2\pi\upsilon$. After the wave have traveled a distance of $1/\alpha$ through the medium, the flux density will drop by a factor of exp[−1]. This distance is known as the skin depth or penetration depth; If a material is transparent, it must have a large penetration depth in relation to its thickness. In metals however, the penetration depth tends to be very small, explaining the observed opacity of most metals. Metals are highly reflective primarily because incident waves cannot effectively penetrate the medium and the majority of incoming flux is reflected (Hecht 2002). Reflectance (R_f) is the ratio of reflected flux to incident flux. R_f can be calculated for conductive media from the equation

$$R_f = \frac{(n_R - 1)^2 + n_I^2}{(n_R + 1)^2 + n_I^2} \tag{3.5}$$

The reflectance for aluminium is greater than 0.9 for UVR (Langmack 1997). Reflectance is also related to wavelength as the refractive index is dependent upon it. The spectral reflectivity versus wavelength for aluminium is shown in figure 3.5.

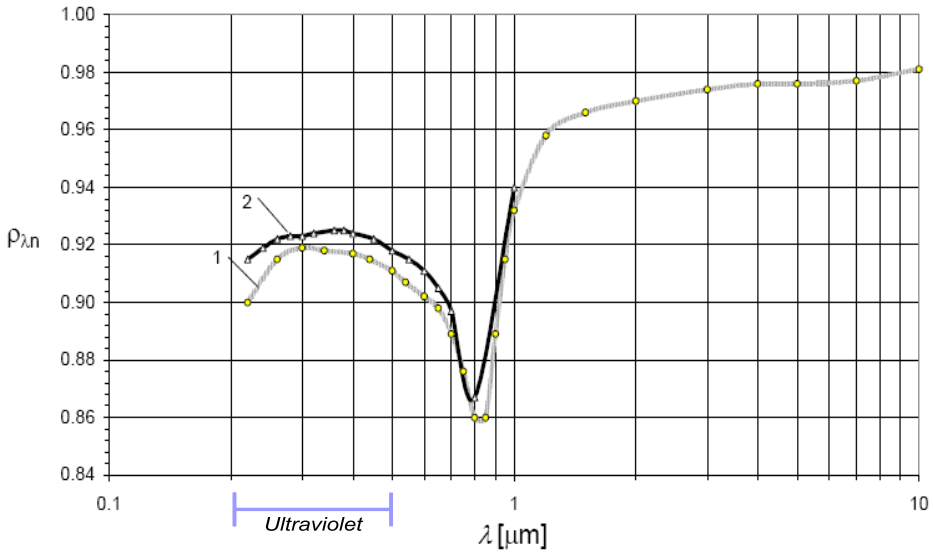

Figure 3.5: *Spectral normal reflectivity of Aluminium at 295 K. Adapted from Bartl and Baranek 2004. [1] Denotes literature values, [2] denotes range of measured values.*

Reflectivity is a property of the material dependent on the polarization of the incoming wave and the incident angle. For incoming light with the electric vector perpendicular to the plane of incidence then the reflectivity R_s (Heavens 1955) is given by

$$R_s = \frac{(n_R^2 + n_I^2) - 2n_R \cos\phi + \cos^2\phi}{(n_R^2 + n_I^2) + 2n_R \cos\phi + \cos^2\phi} \tag{3.6}$$

If the light is polarized so that the electric vector is parallel to the plane of incidence than the reflectivity R_p (Phillips 1983) is given by

$$R_p = \frac{(n_R^2 + n_I^2)\cos^2\phi - 2n_R \cos\phi + 1}{(n_R^2 + n_I^2)\cos^2\phi + 2n_R \cos\phi + 1} \tag{3.7}$$

For natural unpolarized light (Abeles 1967) R is dependent on incident angle by

$$R(\phi) = [R_s(\phi) + R_p(\phi)]/2 \tag{3.8}$$

Table 3.1 from Hass and Waylonis (1961) shows some optical constants for evaporated aluminium at various wavelength. The variation of R_s, R_p and $R(\phi)$ with varying angle of incidence at $\lambda = 340nm$ is shown in figure 3.6. In the case or normal incidence the equations for reflectivity reduce to the case for reflectance in equation 3.5. It is important to distinguish between reflectance and reflectivity; reflectance is a property of an actual surface where as reflectivity is a material property in a section thick enough to be opaque (Grum and Becherer 1979). This means that the term reflectance is specific to a given surface and includes the effects of multiple reflections whereas the term reflectivity refer to the elementary process independent of slab thickness (Garbuny 1965). Oftentimes these terms can be interchanged but it is worthwhile to note the difference for cases where this breaks down.

Table 3.1: Optical constants for evaporated Aluminium

λ **(nm)**	n_R	n_I	$R_{\phi=0}$ (%)
220	0.14	2.35	91.8
240	0.16	2.60	92.1
260	0.19	2.85	92.0
280	0.22	3.13	92.2
300	0.25	3.35	92.1
320	0.28	3.56	92.2
340	0.31	3.80	92.3
360	0.34	4.01	92.4
380	0.37	4.25	92.6
400	0.40	4.45	92.8

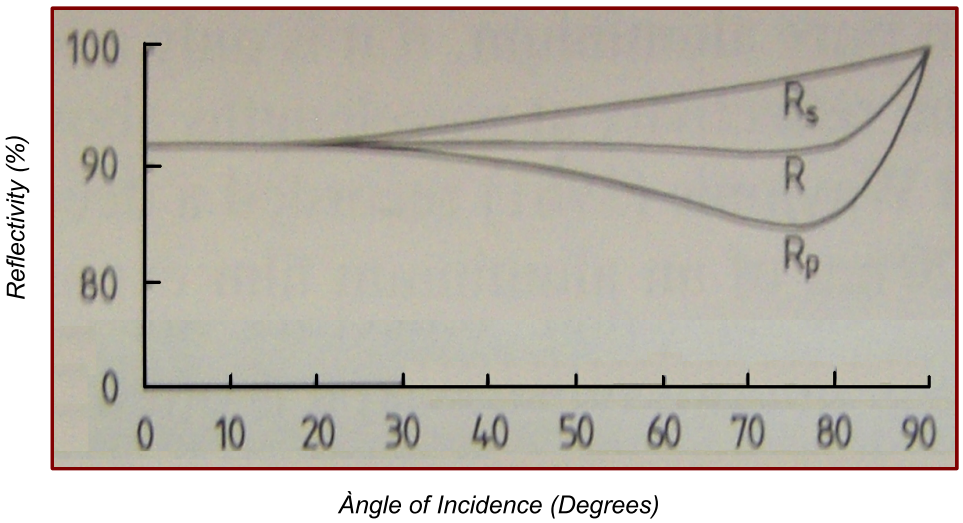

Figure 3.6: *Reflectivity with angle for aluminium and a wavelength of 340nm. R_s, R_p and R are shown. Adapted from Phillips 1983*

While the reflectivity of aluminium is very high, the situation in practice is complicated somewhat because pure aluminium is not feasible for use as it oxidizes; instead, most manufacturers opt for anodized aluminium. Anodization is the process of increasing the naturally forming oxide layer on a metal to increase its damage and corrosion resistance. Anodic layers are non-conductive (Davis 1993) and increase surface hardness. In addition to anodization, aluminium alloys are often used in combination with anodization (Phillips 1983). While this provides protection for the metal itself and prevents it from degrading, it has implications for the reflections from the surface.The situation depends then on the coating used; Spectral reflectance measurements for two anodized sheet materials are shown in figure 3.7. These materials are sold under the names Alzak and Coilzak respectively. The former is a premium quality product made from high purity aluminium and anodized in sheet form. The latter is less expensive material made from a bright trim alloy. The process of anodization drastically impacts on the UVR reflectance; while pure aluminium has reflectance greater than 0.9 at 311nm, Alzak is only about 0.6 at this wavelength and Coilzak only around 0.3 (Phillips 1983, Langmack 1997). In general, the higer the purity of the aluminium used, the greater the specular reflectivity (Wernick and Pinner 1972, Chalkley 1973) and anodizing metal causes a large drop in reflectance (Jackson and Thomas 1979).

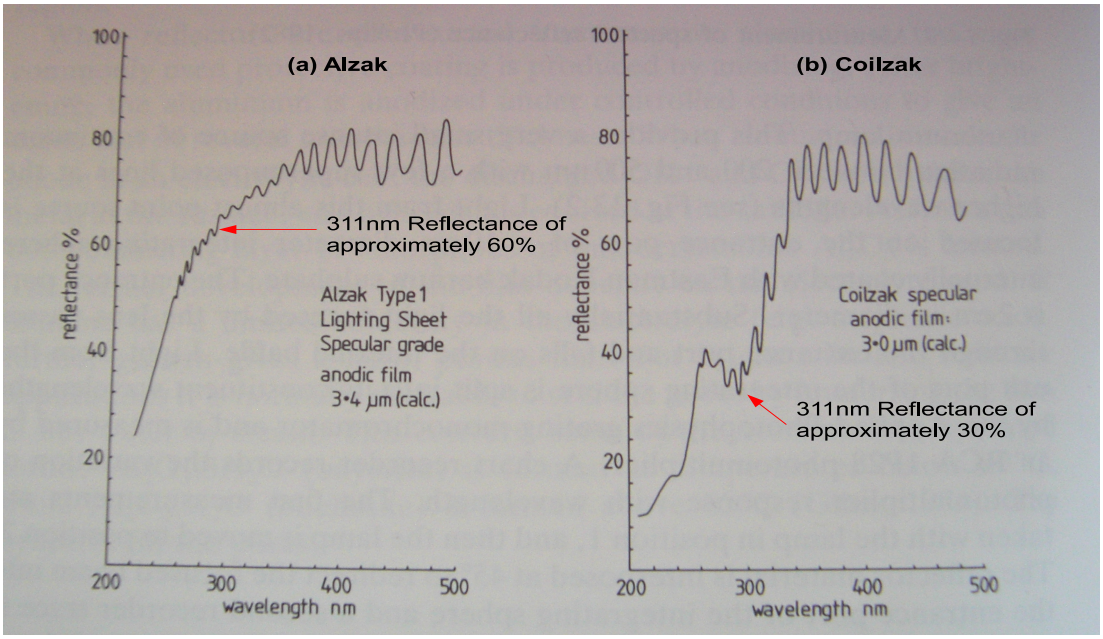

Figure 3.7: *Reflectance for Alzak and Coilzak. Taken from Phillips 1982*

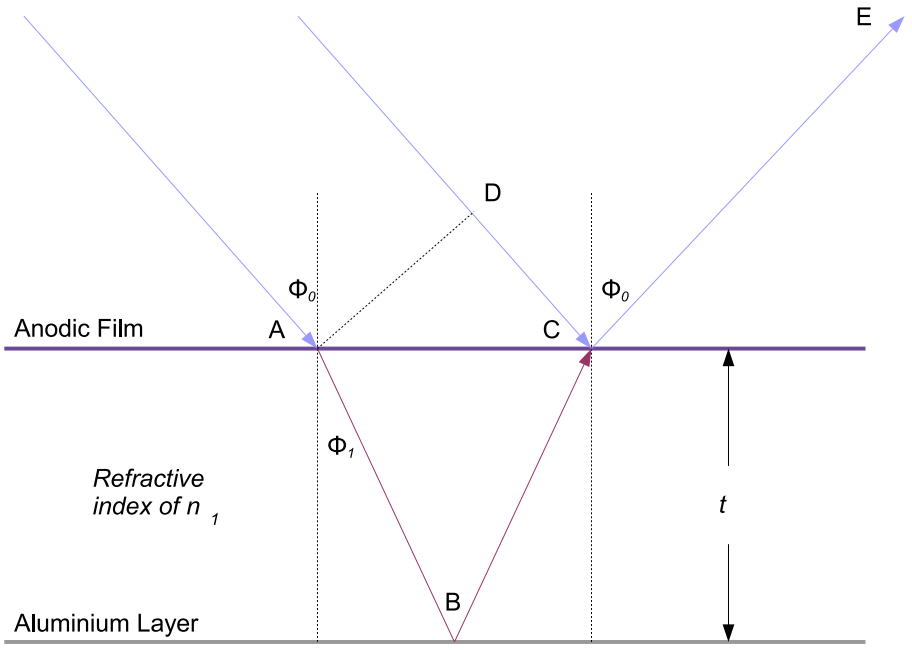

Figure 3.8: *Interference between Anodic film and aluminium. Modified from Phillips 1983*

Another issue that arises with anodizing is the interference effects between the anodized layer and the metal layer itself. This manifests itself in the striking modulations seen in the curves for anodized surfaces such as those shown in figure 3.7. This modulation is the direct result of interference between waves reflected from the dielectric coating and the surface itself, as illustrated in figure 3.8. An approaching wavefront hits the film with incident angle ϕ_0. Some of this light enters the film with refracted angle ϕ_1. The total reflected ray CE is composed of reflected components from both the film and metal layer. If the optical path length between DC and ABC is an integer number of wavelengths constructive interference occurs. There will also be an absolute phase change between the two boundaries. These are namely δ_1 for the air - anodic film interface and δ_2 for the film - Aluminium interface. Thus, constructive interference for wavelength λ_1 occurs when the following condition is satisfied.

$$2n_1 t \cos\phi_1 + \delta_1 - \delta_2 = m\lambda_1 \tag{3.9}$$

where m is an integer. If the wavelength changes to λ_2 such as the path difference becomes $m+1$ times the wavelength, constructive interference will again take place such that

$$2n_1 t \cos\phi_1 + \delta_1 - \delta_2 = (m+1)\lambda_2 \tag{3.10}$$

Hence m can be eliminated and an expression linking the wavelengths of adjacent peaks obtained. This is given by

$$t = \frac{1}{2n_1 \cos\phi_1}[\frac{\lambda_1\lambda_2}{\lambda_1 - \lambda 2} - (\delta_1 - \delta_2)] \tag{3.11}$$

Hass (1949) has shown that the term $\delta_1 - \delta_2$ is practically independent of wavelength and small ($\simeq 50nm$) compared to the other terms so this term can be neglected, reducing the expression to

$$t = \frac{1}{2n_1 \cos\phi_1}[\frac{\lambda_1\lambda_2}{\lambda_1 - \lambda 2}] \tag{3.12}$$

This condition explains why anodic films cause modulations which can be observed in the peaks of the reflectance patterns (Phillips 1983). Langmack (1997) estimates that an R_f of 0.3 is a realistic value for UVB around 311nm though all the other conditions discussed in this section can alter this significantly. Waldmann (Baermann and Muenk 2010) use reflectors made by Alanod, specifically Alanod 318G2 which is an alloy of 99.85% aluminium with a reflectance of up to 0.85 at $311nm$ and approximately 8% diffuse reflection

3.2 Ultraviolet dosimetry in practice

3.2.1 Initial dose

The concept of skin typing has been mentioned in chapter 2, but it is worth explaining the clinical process in some more depth as it is usually performed prior to treatment. For treatments without a photosensitizing agent, the minimum erythemal dose (MED) is ascertained for a patient. For a treatment such as PUVA with a phototoxic agent, the minimum phototoxic dose (MPD) must be found. The method for yielding these quantities are essentially the same. The most common method involved using a thin plastic template with eight small windows; the template is positioned over an area of skin relatively unaccustomed to UV light, such as buttocks or back. The remainder of the body is protected. A sequence of exposures are performed on each slit, with each successive one in the ratio of $\sqrt{2}$ to the previous exposure (Taylor *et al* 2002).

For UVB, erythema peaks between 8 - 24 hours after initial exposure, and the template sites can be examined to find the lowest dose of UVB resulting in an erythema. This is the MED for the patient. The peak of UVA exposure tends be between 48-72 hours after exposure and the MPD can be determined then by a similar visual inspection. Treatment usually begins as a ratio of the MED/MPD, typically 50-70%. The patient is then started on this dose and it is incremented over several weeks until a marked improvement of the condition is observed by the physician or clinician (Van Weelden *et al* 1988, Taylor *et al* 2002).

There are other similar methods for ascertaining the starting dose; another method (Diffey 1993, Gorden *et al* 1998) involves a photo-testing template with a number of foil apertures. These apertures are all differing sizes and thereby attenuate the incident UVR by varying amounts, thus causing skin exposure of varying irradiance at different hole sites. The MED/MPD is then inspected visually again. It should be noted the starting dose method relies on visual inspection and can be somewhat subjective.

3.2.2 ScUViDo protocol

As discussed in chapter 1, UVR outputs from phototherapy tubes fall over time. The skin testing method can only then give information about the skin's response to that particular test source and so the problem remains of comparing two sources with an objective method. The Scottish photochemotherapy audit board (1995) identified this as a serious problem and recommended steps so that UVR therapy sources could be correctly compared and contrasted over the lifetime of a unit and even between units and phototherapy centres. The guidelines laid down improved PUVA treatment doses and were updated in 2001 (Moseley 2001) for NB-UVB sources. The premise of the Scottish ultraviolet dosimetry (ScUViDo) is to provide a standard for UV irradiance in treatment centres. A flowchart depicting the process is shown in figure 3.9.

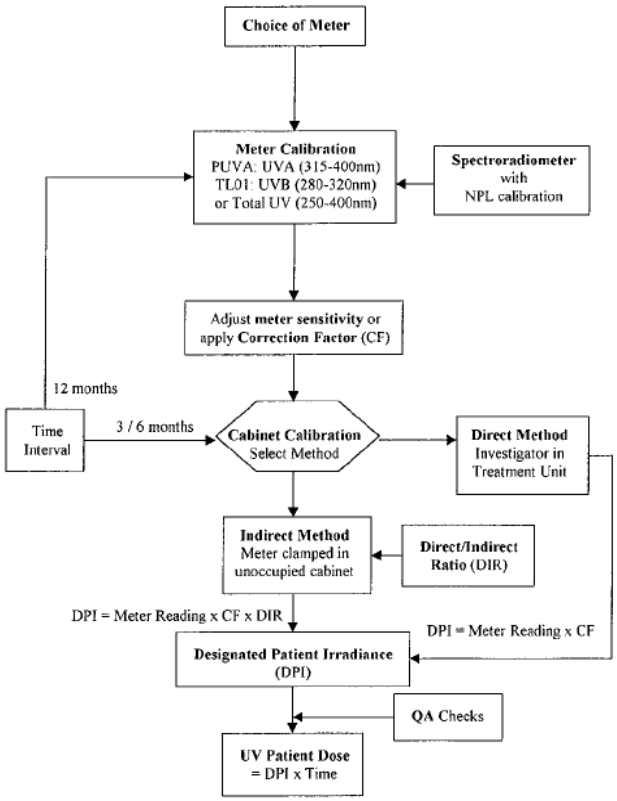

Figure 3.9: *ScUViDo protocol. Reproduced from Moseley (2001)*

3.2.2.1 Calibration

In ScUViDo, the meter used must be calibrated against the source which it is designed to work with; in the case of a UVA meter, a bank of UVA tubes and for a UVB meter a bank of TL/01 tubes. The cosine response error of the meter should be low with an f_2 error of less than 10%. The calibration of any meter used should be traceable to the National Physical Laboratory. The display should be adjusted if needs be or a correction factor applied and the accuracy should be ±10%. Meter calibration should be performed annually.

3.2.2.2 Designated Patient Irradiance

The designated patient irradiance (DPI) is the average irradiance on a patient of average height and build standing in a phototherapy cabin at chest, waist and knee height. The investigating physicist in appropriate UVR protection gear stands in the cabin and adopting the position of a patient in treatment makes a series of measurements at various positions as shown in figure 3.10.

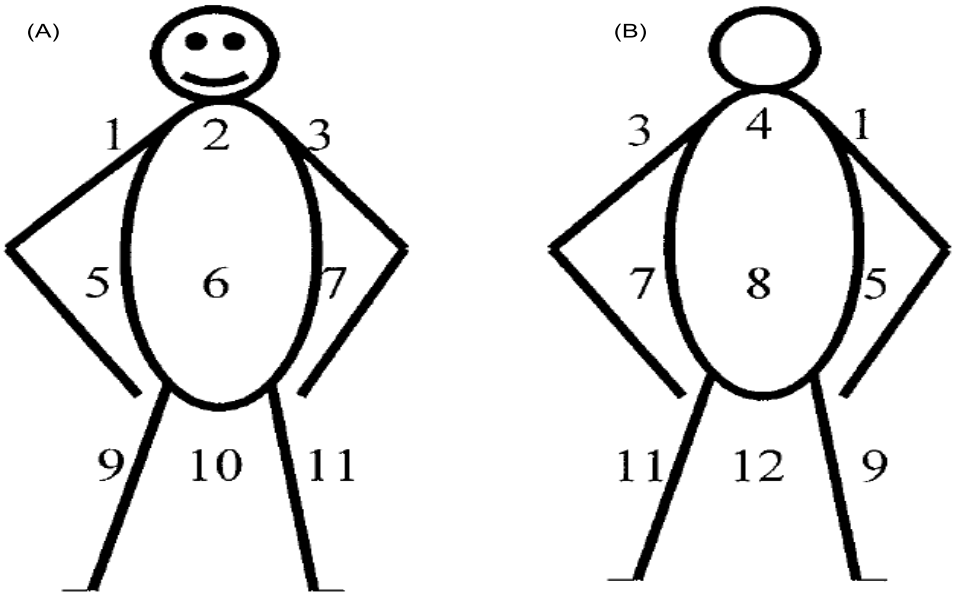

Figure 3.10: *DPI measurement sites (A) Anterior (B) Posterior. Reproduced from Moseley (2001)*

The lamps are usually warmed up 5 minutes prior to measurements being made, and the investigating physicist uses a hand held UV meter appropriate for the wavelength band of the lamps. Measurements are taken on the twelve sites and recorded. This gives the mean DPI at each body site without requiring a recourse to a known body correction factor. It is important to ensure that clothing does not obstruct any emitting sources. The colour of the clinicians clothing can lead to variations of approximately 5% (Moseley 2001). There is also an indirect method for obtaining the DPI by placing a retort stand with a clamped meter in place and multiplying by a correction factor. This correction factor should ideally be ascertained for each individual cabin to improve accuracy. A list of correction factors for indirect DPI are shown in table 3.2.

Table 3.2: Correction factors for indirect DPI (Moseley 2001)

Unit type	**Meter type**	**Distance (cm)**	**Ratio**
Waldmann UV-1000 (PUVA)	Waldmann	25	0.68
Waldmann UV-6001 (PUVA)	Waldmann 585-100	30	0.80
Waldmann UV-6002 (PUVA)	Waldmann 585-100	30	0.80
Waldmann UV-7001 (PUVA)	Waldmann 585-100	30	0.80
Waldmann UV-8001 (PUVA)	Waldmann 585-100	30	0.80
Waldmann UV-6001 (PUVA)	Dixwell UV-365	30	0.75
Waldmann UV-6002 (PUVA)	Dixwell UV-365	30	0.75
Waldmann UV-7001 (PUVA)	Dixwell UV-365	30	0.75
Waldmann UV-8001 (PUVA)	Dixwell UV-365	30	0.75
Dixwell	Waldmann 585-100	25	0.8
Waldmann UV-5000 (UVB)	International light UVB1	30	0.77
Waldmann UV-1000 (UVB)	International light UVB1	20	0.75
Dixwell (UVB)	International light UVB1	20	0.90

The ScUViDo protocol has the advantage of allowing comparison of treatments between different centres and units. It also indicates when lamps need to be replaced, typically when DPI has changed by 10%. Despite the advantages and practicality of this approach, patient and clinician self shielding can still be a factor heavily influencing the DPI as different builds will shield different regions. Though the dosages indicated by ScUVido are not absolute, it does allow detection of variations.

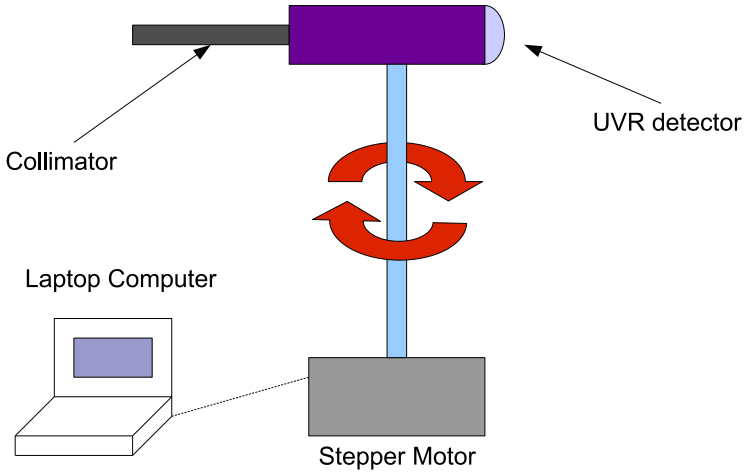

Figure 3.11: *Automated detector system. Arrows denote rotation direction*

3.2.3 Automated detector system

The ScUVido protocol is useful for localized calibration and facilitates comparison of irradiance between different phototherapy centres, as well as indicating when irradiance has dropped due to lamp failure or aging. It is also cheap to implement and consequently used not only in Scotland but across many European phototherapy centres. Another method to examine and calibrate UVR cabins involves the use of an automated detection system as outlined by Currie et al (2001). The basic set up is illustrated in figure 3.11.

The system comprises of two detectors facing opposite directions from each other; one is a wide angle UVR detector with a raised polytetrafluorethylene (PTFE) diffuser and the other is a photodiode housed at the end of a $200mm$ collimating tubes with slots at either end measuring $10mm$ by $1mm$. The entire mount rotates on a stepper motor which records the irradiance at 800 points in a full rotation for both the normal and collimated detector. The data is send to a laptop computer which can display this information as a linear or polar plot.

There are major advantages to such a system; firstly, it doesn't require an operator so self-shielding by the investigator is not a problem. Secondly, the collimated detector allows the user to see specifically which individual tubes are failing or

reducing in output. Thirdly, it offers greater repeatability than the ScUViDo method and less uncertainly as readings are automated and human error is a less of a factor. The downside is that the system is quite costly and so far it has not been widely adopted despite its advantages (Martin 2010). It also doesn't factor self-shielding into the analysis, meaning results would need to be considered with this in mind.

3.2.4 Photodetector and Radiometer design

The accurate measurement of UVR is paramount to obtaining a suitable treatment dose. The majority of UVR radiometers consist of a photodiode mounted behind a filter which acts to limit the incoming radiation to the wavelengths the radiometer is designed to measure; for for example, a UVB radiometer will have input optics designed to filter the UVB portion of the spectrum. As the head photodiode is placed behind filters and often embedded deep in the probe head, a diffuser is a vital part of the radiometer set-up. Several different types exist, designed to improve angular response so UVR can be correctly quantified.

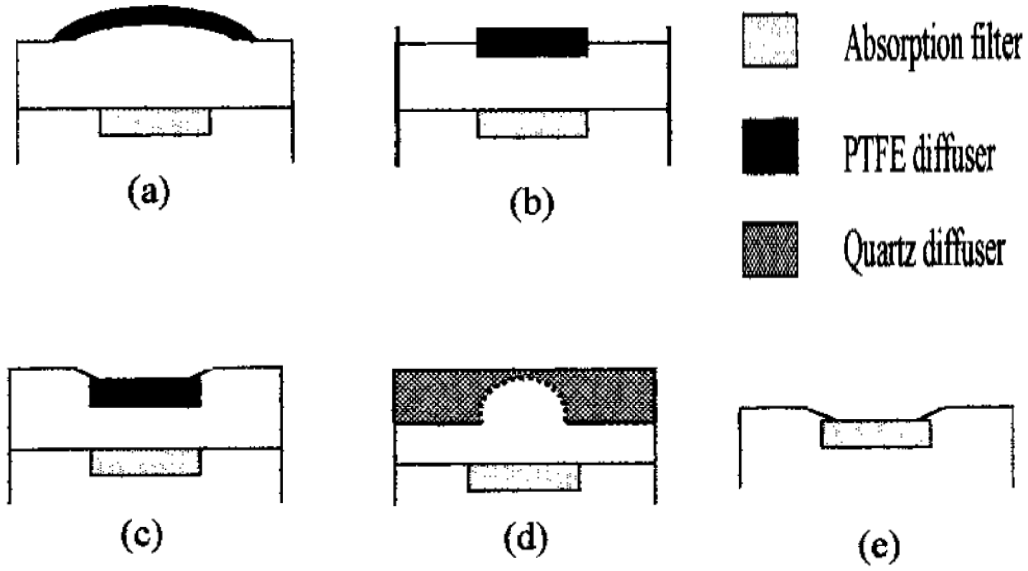

Figure 3.12: *Diffuser designs; (a) Raised PTFE dome (no rim) (b) Raised PTFE dome (with Rim) (c) Recessed diffuser (d) Ground quartz diffuser (e) No diffuser. Adapted from Pye and Martin 2000.*

3.2.4.1 Angular response

UVR meters can have wildly varying responses to UV light at varying angles. A perfect detector would have a cosine response (Coleman *et al* 2000) and should vary with the cosine of the incident angle. In practice, the photodiodes used in radiometers may be nested inside the receiving head and a cosine response may not be obtained. One way of correcting this is to use a diffuser head which facilitates the cosine response. There is considerable variation in the manufacture of such devices (Pye and Martin 2000, Martin *et al* 1999). The figure of merit, f_2, is the deviation of actual directional response $D(\alpha)$ from perfect cosine response, defined by the CIE 69 (1987). It is then given by

$$f_2\% = 100 \int_0^{\alpha_m} 2|D(\alpha)\sin\alpha - c(\alpha)\sin\alpha|d\alpha \tag{3.13}$$

Where $c\alpha = \cos\alpha$ for $0^\circ < \alpha < 90^\circ$ and $c\alpha = 0$ for $\alpha > 90^\circ$. There is also an internation standard BS 667 (1996) which defines the direction error T. The version modified by Pye and Martin (2000) to accept angles of up to 90° is

$$T\% = 100 \int_{0^\circ}^{90^\circ} |D(\alpha) - c(\alpha)|d\alpha \tag{3.14}$$

Pye and Martin (2000) examined a number of different detector set-ups and found that detectors with polytetrafluorethylene (PTFE) diffusers with rims to cut off irradiance from $\alpha > 90^\circ$ performed exceptionally well with $f_2 < 5\%$. These diffusers have raised domes to direct the incoming UVR to the photodiode encased in the filter head and maintain a good cosine response at all angles. Quartz differs had poor angular response but were mechanically robust; the authors recommended that detectors with $f_2 < 10\%$ should be used in all phototherapy centres and ideally $f_2 < 5\%$.

3.2.4.2 Internal dosimeters

Several modern cabins include a built in dosimeter to facilitate irradiance calculations. There are several problems with this approach (Diffey and Hart 1997); the dosimeters have to be placed on a wall and oftentimes they are located in the corners and lower areas, meaning their irradiance will be significantly lower than a patient might get and thus not representative. Secondly, patients will tend to shield detectors located on the cabin during the course of therapy and the UVR detector will not be measuring the typical cabin and patient intensity. The detectors are prone to accumulation of dust and skin, which would result in a false low reading. Finally, constant exposure to UVR over the long periods of treatment would tend to reduce the sensitivity. For these reasons, the readings provided by built-in sensors should be treated skeptically and not form any basis of treatment dosimetry.

3.3 Conclusions

There are several problems with current dosimetry methods as they stand. Firstly, MED and MPD are subjective measurements made by a clinician; the irradiance from the UVR source on the skin itself is not being calculated and could vary with source output over time. In fact, this is almost certainly happening as the skin itself photoadapts with each successive treatment and changes over time. For this reason, MED/MPD may provide a rough estimate but essentially it amounts to using the patient's skin as a rather inaccurate dosimeter. This means the uncertainty is high and so too is the probability of either under or overdosing the patient if this method on its own is solely used.

The ScUViDo method is a great improvement as it allows comparison between units and test centres. It also gives a rough estimation of self-shielding by virtue of measuring irradiance with an operator in situ but cannot account fully for the shielding provided by the patient which can vary massively despite its clinical practicality. The automated detector system is a unique and interesting

approach to determining cabin irradiance and is very useful in ascertaining instances of lamp failure but it is expensive to implement and cannot as it stands allow for patients self-shielding.

For these reasons, an accurate dose model would be beneficial as it would allow objective dose recording and comparison between units and centres without the inherently large uncertainty found in other methods. The characterization of artificial UVR sources has been an area marked for research by the NRPB (2002) for precisely these reasons. Such a model would not only facilitate accurate dose estimation for treatment, but could also give insight into processes such as photoadaptation discussed in chapter 2.

3.4 References

- Abeles F 1967 In *Advanced optical Techniques* eds. ACS Van Heel, pp 145-188. North Holland, Amsterdam
- Amatiello H and Martin C J 2006 Ultraviolet Phototherapy: review of options for cabin dosimetry and operation *Phys. Med. Biol.* **51** 299-309
- M Baermann and N Muenk 2010 *Engineering department Waldmann Inc* - Personal communication
- Bartl J and Baranek M 2004 Emissivity of aluminium and its importance for radiometric measurement, Institute of measurement science, Slovak Academy of Sciences
- BS 667, 1996 *Specification for illuminance meters*, London (British Standards institution)
- Chalkley B 1973 The Chemical and Electrochemical Polishing of Aluminum *Proc. 4th Symp. Electroplating* pp193-205, Kiadja, Budapest, Hungary
- CIE 69, 1987 *Methods of Characterizing Illuminance Meters and Luminance Meters: Performance, Characteristics and Specifications* (Vienna: Commission Internationale de lEclairage)
- Coleman A J, Collins M and Saunders J E 2000 Traceable calibration of ultraviolet meters used with broadband, extended sources *Phys. Med. Biol.* **45** 18596
- Currie G D, Evans A L, Smith D, Martin C J, McCalman S and Bilsland D 2001 An automated dosimetry system for testing whole-body ultraviolet phototherapy cabinets *Phys. Med. Biol.* **46** 333 - 346
- Davis JR 1993 *Aluminum and Aluminum Alloys* (4th ed.). ASM International.
- Diffey BL and Hart G 1997 *Ultraviolet and Blue-Light Phototherapy - Principles, Sources, Dosimetry and safety.* York: IPEM

- Diffey BL, de Berker DAR, Saunders PJ and Farr PM 1993 A device for phototesting patients before PUVA therapy *Br. J. Deramtol.* **129** 700-703
- Gordon PM, Saunders PJ, Diffey BL, Farr PM 1998 Phototesting prior to Narrowband (TL-01) Ultraviolet B Phototherapy *Br. J. Deramtol.* **139** 811-814
- Garbuny M 1965 *Optical Physics* New York and London: Academic Press
- Grum F and Becherer RJ 1979 *Optical Radiation Measurements Volume I* New York and London: Academic Press
- Hass G and Waylonis JE 1961 Optical constants and reflectance and transmittance of evaporated aluminum in the visible and ultraviolet *J. Opt. Soc. Amer.* **51** 719-722
- Heavens OS 1955 *Optical properties of thin solid films* London: Butterworth
- Hecht E 2002 *Optics* 4th Ed. San Francisco: Adelphi University / Pearson Education Inc.
- Jackson CM and Thomas RW 1979 The Specular Reflectivity of Bright Anodized Aluminium *Trans. Inst. Met. Finish.* **57** 105-109
- Langmack K A 1997 An insight into the contributions of self-shielding and lamp reflectors to patient exposure in phototherapy units *Phys. Med. Biol.* **43** 207 - 214
- Martin C J, Currie G D, Pye S D 1999 The importance of radiometer angular response for ultraviolet phototherapy dosimetry *Phys. Med. Biol.* **44** 843 - 855
- Martin CJ 2010 Private communication (Health Physics, Department of Clinical Physics and Bio-Engineering, North Glasgow University Hospitals NHS Trust, Western Infirmary, Dumbarton Road, Glasgow G11 6NT, UK)
- Moseley H 2001 Scottish UV Dosimetry guidelines "ScUVido" *Photodermatol. Photoimmunol. Photomed.* **17** 230-233

- National Radiation Protection Board (NRPB) 2002 *Health effects from Ultraviolet Radiation* Report of an advisory group on non-ionising radiation, Documents of the NRPB Vol. 13, No. 1, 15-16

- Phillips R 1982 Reflector Materials for Ultraviolet Driers *Trans. Inst. Met. Finish.* **61** 233-240

- Phillips R 1983 *Sources and applications of Ultraviolet Radiation* London: Academic Press

- Pye S D and Martin C J 2000 A study of the directional response of Ultraviolet radiometers: I. Practical evaluation and implications for ultraviolet measurement standards *Phys. Med. Biol.* **44** 2701 - 2712

- Royal Philips Electronics 2007 Effective Light - *Phillips lamps for therapeutic purposes* Royal Philips Electronics brochure

- Taylor DK, Anstey AV, Coleman AJ, Diffey BL, Farr PM, Ferguson J, Ibbotson S, Langmack K, Lloyd JJ, McCann P, Martin CJ, Menage H, Mosely H, Murphy G, Pye SD, Rhodes LE and Rogers S 2002 Guidelines for Dosimetry and Calibration in Ultraviolet Radiation Therapy; a report of a British Photodermatology Group workshop. *Br. J. Deramtol.* **146** 755-763

- Van Weelden H, Baart de la Faille H, Young E, Van Der Leun JC 1988 A new development in UVB Phototherapy of psoriasis *Br. J. Deramtol.* **119** 11-19

- Wernick S and Pinner R 1972 *The surface treatment and finishing of Aluminium alloys* 4th Ed. Teddington: Robert Drapper Ltd.

Chapter 4

Existing dose models in UVR phototherapy

The advantages of a dose model have been outlined in the preceeding chapter and studies into the quantification of artificial sources of UVR is a recommended area for research by the NRPB (2002). Some work in the area of UV dose modeling for ultraviolet sources has already been done, and it is worthwhile to examine these approaches.

4.1 Limitations of simple inverse square model

The simplest type of light measurement model rests on a source approximating a point source radiating isotropically. This is a valid approximation in some optical areas. In such a case, the electromagnetic radiation recorded is inversely proportional to the square of the distance from the source, as expressed in equation 4.1

$$E \propto 1/r^2 \tag{4.1}$$

where E is the measured irradiance at distance r from source. While this approximation provides good results when r is large, this is not the case in phototherapy. A general rule of thumb for making irradiance measurements is the 'five times rule' (Ryder 1997), which states any inverse square law approximations to a source are

only valid where the source to detector distance is at least five times the greatest dimension of the source. A typical tube has length $\simeq 1.74m$, meaning that if one was to consider the entire lamp as a point source, the measurements would have to be at least $8.7m$ away. Typical phototherapy cabins have a floor area less than $1m$ x $1m$, so it is immediately apparent that such an approximation will not suffice for phototherapy. Hence a point source approximation will not suffice for phototherapy.

4.2 Radial emitter models

Prior to 1970, radial emitter models were used exclusively in approximating photochemical reactors (Phillips 1983). The Radial model makes the evidently erroneous assumption that all photons emitted from a source are perpendicular to the surface of the source, as illustrated if figure 4.1. Despite the obvious inaccuracy, this method can give remarkably good results under certain conditions as the non-perpendicular conditions can essentially cancel each other out (Akehara and Shirai 1972).

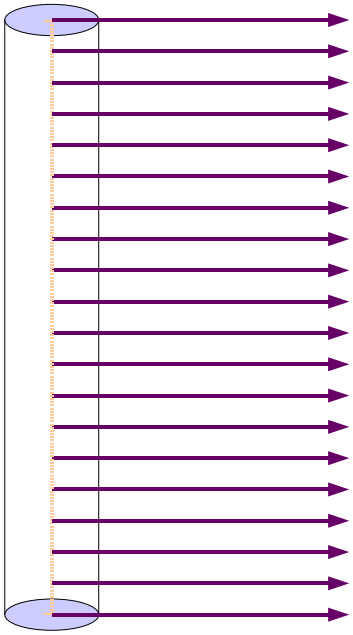

Figure 4.1: *Radial emitter. Note the output from centre of source rather than tube edges*

The form for the radial emitter is inherently simple; a distance r from the emitter, the irradiance would be proportional to that measured on the surface of a cylinder of that radius. This can be expressed as

$$E = S_L/2\pi r \tag{4.2}$$

Where S_L is the power per unit length in units of W/m. The radial model can give accuracy of within 10% where the distance from lamp to detector is small but fails at predicting the irradiance from small surface elements (Akehata and Shirai, 1972). It also does not take into the account the angle at which photons strike the detector, rendering it of limited use in UVR dosimetry (Phillips 1983).

4.3 Specular and diffuse emitter models

Specular and diffuse models of irradiance have been examined in context of photochemical reactors (Akehara and Shirai 1972). The basic emitting profile of these two models are shown in figure 4.2.

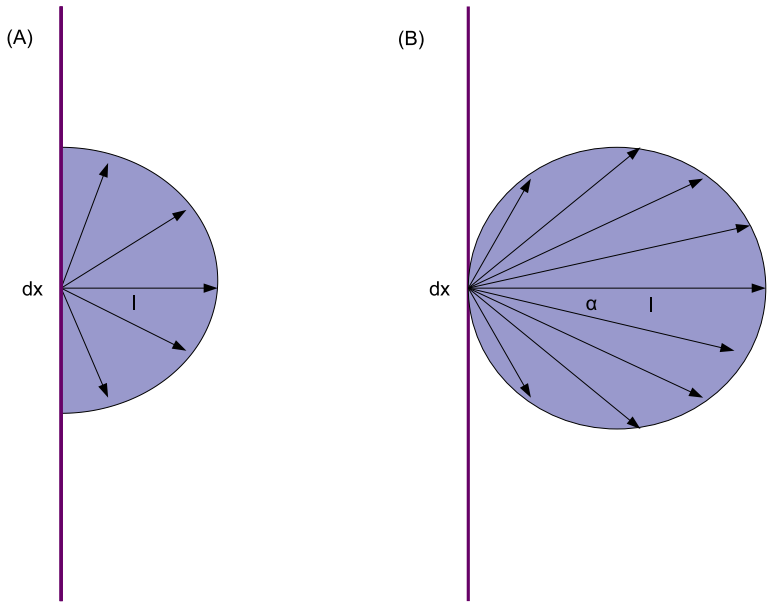

Figure 4.2: *(A) Specular emitter (B) Diffuse Emitter*

The specular model makes the assumption that each small element of the lamp acts as a point source and emits uniformly into a solid angle of 4π. In this case, the total radiation flux from the segment of length dx is equal to the sum of the radiation crossing the sphere of unit-length radius whose origin is at the centre of dx (Akehara and Shirai 1972) so that

$$S_L dx = 2\int_0^{\pi/2} (Idx)2\pi \cos\alpha d\alpha = 4\pi I dx \tag{4.3}$$

Which can be re-arranged in terms of the power per unit length S_L to give the radiant intensity I

$$I = S_L/4\pi \tag{4.4}$$

The diffuse model approximates each element to a Lambertian radiator, which means cosine dependence on the intensity from an element. This can be expressed as

$$S_L dx = 2\int_0^{\pi/2} (Idx\cos\alpha)2\pi cos\alpha d\alpha = \pi^2 I dx \tag{4.5}$$

Which rearranges to

$$I = S_L/\pi^2 \tag{4.6}$$

Both models represent an improvement over the radial model, and the diffuse model is superior to the specular model for a fluorescent tube source (Funayama 1977).

4.4 Line source models

The specular and diffuse models give rise to the concept of line sources; these are linear arrays of point sources integrated along the length of the source, in this case the UVR lamp. In the context of phototherapy, some work has been done on treating the UVR lamps as line sources. These approaches are discussed here.

4.4.1 Martin and Pye model

This model considers the irradiance on a vertical surface O (a surface of skin or a radiometer) from a line source tube broken into elements of length Δl_α. The geometry of this situation is depicted in figure 4.3. From this one can compute the irradiance from this finite length $\Delta I_{R\alpha}$ and summate.

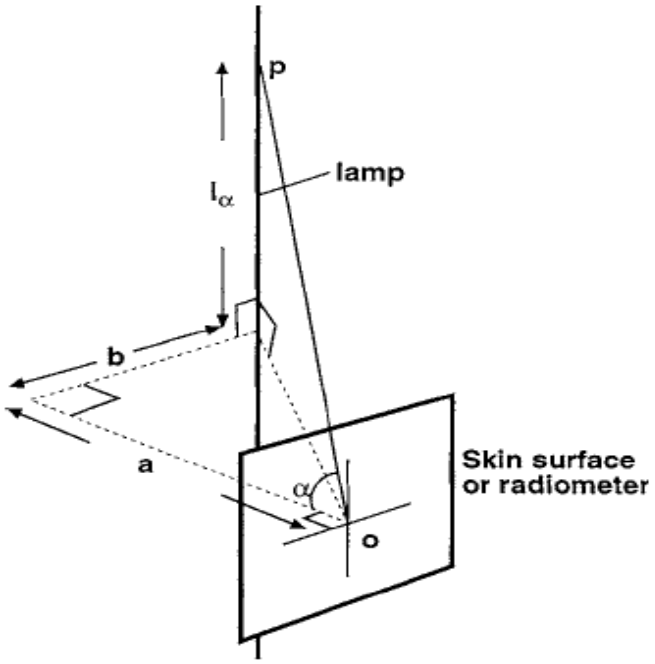

Figure 4.3: *Geometry of Martin-Pye Model. Reproduced from Martin and Pye 2000*

At a height of l above or below the reference point at O with a mean angle of incidence α, the irradiance can be expressed as

$$\Delta I_{R\alpha} = \frac{S_L \cos\alpha \Delta l_\alpha}{a^2 + b^2 + l_\alpha^2} = \frac{S_L a \Delta l_\alpha}{(a^2 + b^2 + l_\alpha^2)^{3/2}} \tag{4.7}$$

So the irradiance for each lamp over a discrete range of angles α can be expressed as

$$I_R = \sum \frac{S_L a \Delta l_\alpha}{(a^2 + b^2 + l_\alpha^2)^{3/2}} \tag{4.8}$$

The values of α used in Martin and Pye's model were discrete; they were 0° - 2.5°, sixteen 5° ranges from 2.5° to 82.5° and three ranges to cover angles from 82.5° to 90°. This gives 40 elements contributing to irradiance. This meant for example, a 1.74m lamp 200mm from the detector would be divided into 32 elements with angles between 0° and 77°. This means in practice that the number of elements being summed will change at varying displacements; for example if the displacement was instead 555mm, there would be 24 elements summed for angles between 0° and 57.5°. This model was developed to test the angular response of radiometers and diffusers rather than construct a comprehensive dose model but it does have some merit for this purpose. As the model was not specifically developed for dose modeling, it does not contain any correction terms for patient obstruction and reflection contribution.

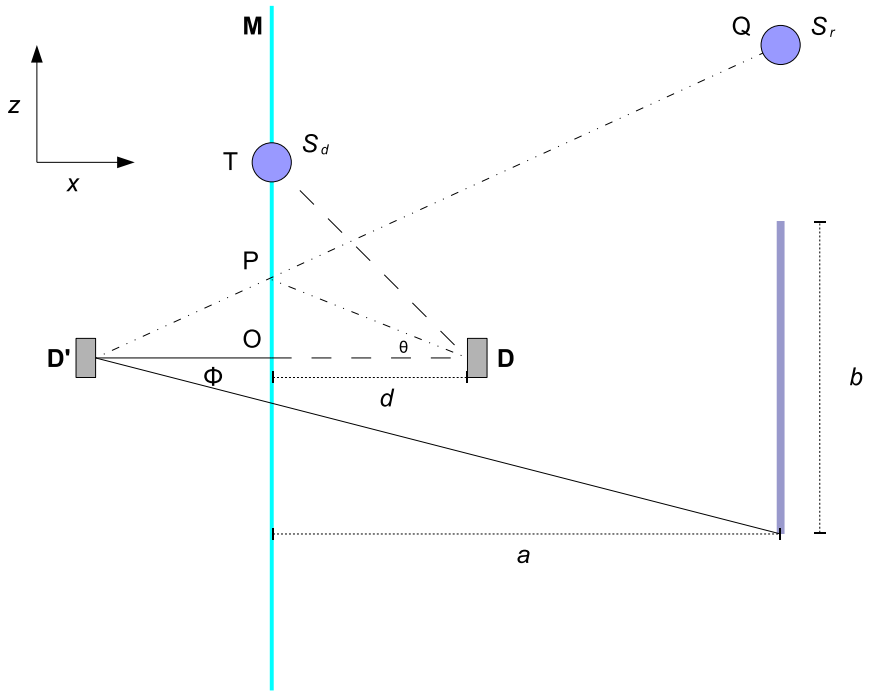

Figure 4.4: *Geometry of Langmack Model. Adapted from Langmack (1997)*

4.4.2 Reflection and obstruction modeling

While Martin and Pye's model is useful in ascertaining the irradiance due to a tube or multiple tubes, it does not give any information about shielding or reflection. Langmack (1997) put forward a model that considers direct contributions from line source tubes and indirect contributions from reflections of tubes upon a mirrored surface. A person in the cabin acts as a barrier of width b. Their presence can block some of the reflections and lower the recorded irradiance. The geometry of this model is shown in figure 4.4.

Let O be the origin of a co-ordinate system (X-Z). M is a mirrored wall and D is a detector a distance d away from this wall so that the image of that detector, D', is also a distance of d away from the M. A barrier of width b is placed a distance a from M. There are two light sources; one on M denoted S_d and one beyond the barrier denoted S_r. S_d makes an angle of $\theta(S_d)$ with the D ($\angle TDO$) and the reflection of S_r makes an angle $\theta(S_r)$ ($\angle ODP$) with D.

There are then two possible ways for D to see a light source. If $\theta < 90°$ then the tube is directly visible. If the tube is not on M, it can be viewed by reflection in M. Certain tubes will satisfy both these conditions, giving them two components to detector reading. A person of width b acts as a barrier; this means reflected light with angles less than ϕ will be blocked from the detector. The correction factor is then the ratio of reading with barrier to reading without it.

Let the detector reading when viewing an indirect or direct source i be $I(S_i)$. In Langmack's model, the irradiance falls off to $1/l$ where l is the path length from the tube centre to the detector. Thus it can be written that

$$I(S_i) \propto \frac{\cos(\theta(S_i))}{l_i} \tag{4.9}$$

If $x(S_i)$ and $z(S_i)$ are respectively the x-z co-ordinates of S_i, then for a directly viewed source

$$\cos(\theta(S_d)) = \frac{d}{l(S_d)} \tag{4.10}$$

and re-expressing

$$l^2(S_d) = z^2(S_d) + d^2 \tag{4.11}$$

Then equation 4.9 can be expressed

$$I(S_d) \propto \frac{d}{z^2(S_d) + d^2} \tag{4.12}$$

For a number of directly viewed sources, this can be expressed as

$$I_d \propto \sum \frac{d}{z^2(S_i) + d^2} \tag{4.13}$$

Sources seen by reflection through M at D' have cosine given by

$$\cos(\theta(S_r)) = \frac{d + x(S_r)}{l(S_r)} \tag{4.14}$$

and subsequently

$$l^2(S_r) = z^2(S_r) + [x(S_r) + d]^2 \tag{4.15}$$

Which yields a reflected irradiance of

$$I(S_r) \propto \frac{x(S_r) + d}{z^2(S_r) + [x(S_r) + d]^2} \tag{4.16}$$

Hence for a number of reflected sources the irradiance is

$$I_r \propto \sum \frac{x(S_r) + d}{[x(S_r) + d]^2 + z^2(S_r)} \tag{4.17}$$

Thus in the Langmack model, total irradiance for a finite number of direct and reflected sources without a barrier present (denoted by $\bar{b}$) is given by

$$I_t(\bar{b}) = I_d + I_r(\bar{b}) \tag{4.18}$$

4.4.2.1 Barrier effects

The Langmack model has the advantage of estimating the correction factor due to a barrier. The total irradiance with barrier present is given by

$$I_t(\bar{b}) = I_d + I_r(b) \tag{4.19}$$

Knowing this, and using Langmack's method for calculating the angles which block reflection (Langmack 1997), the obstruction correction factor C_f can be expressed as

$$C_f = \frac{I_t(b)}{I_t(\bar{b})} = \frac{1 + I_r(b)/I_d}{1 + I_r(\bar{b})/I_d} \tag{4.20}$$

4.4.2.2 Reflection correction

Langmack's model assumes that reflection is perfectly specular. However, noting this is not the case, a low reflectivity correction can be added to equation 4.20 to factor in the effects of a co-efficient of reflection R. This yields the equation for reflection

$$C_f = \frac{1 + RI_r(b)/I_d}{1 + RI_r(\bar{b})/I_d} \tag{4.21}$$

4.5 Comment on current Models

The models discussed herein have varying degrees for merit for different applications. Observations on the Radial, Martin-Pye and Langmack models for irradiance are shown in table 4.1.

Table 4.1: Model Comparisons

Model	Intensity fall-off	Incident angle	Reflections
Radial	$\propto 1/r$	No	No
Martin-Pye	$\propto \cos\theta_v/r^2$	Yes	No
Langmack	$\propto \cos\theta_h/r$	No	Yes

As it stands none of these models or even a combination of them are yet suitable in their current state for accurate UVR dosimetry; at a basic level all the models have disagreements. Note also that the cosine factors in the Martin-Pye and Langmack model refer to different angles; the Martin-Pye angle is θ_v and is the

angle made from a vertical element on the tube. In the Langmack model, the angle θ_h is the angle in the xz plane taking no account of the vertical position of the tube. In reality, the real angle will be a combination of both and will have implications for the recorded irradiance. While these current models can be effective for specific scenarios and applications, they can not handle the general case. For example, the Martin-Pye model relies on discrete sums that can produce large inaccuracies and the Langmack model does not take account of true angles of incidence outside the two dimensional XZ plane. Furthermore, the two models seem to disagree on the radiation fall off from a line source, indicating more investigation into the matter should be undertaken. As it stands the models discussed here-in are clever and useful ad-hoc methods for specific situations but there is not yet a general model for phototherapy.

4.6 Conclusions

There is currently no complete and effective model for dosage in ultraviolet phototherapy. Current models are not adequate to characterize the irradiance at any point on a patient's skin and thus the development of a new dose model capable of doing this would be of great benefit in clinical applied phototherapy. A comprehensive dose model would then have the following attributes:

1. Full characterization of the lamp sources: This is the most important and fundamental element in ascertaining the dose received from a phototherapy unit as an understanding of the output from the artificial source will be related to reflections and shielding.

2. Inclusion of reflection contribution: The model should be able to quantify the amount of radiation reflected and incident upon the patient

3. Factor for patient self shielding: Irradiance from multiple / reflected sources should be quantifiable and factored into patient irradiance.

Headway into any of these areas would constitute a major advance in the dosimetry of ultraviolet phototherapy.

4.7 References

- Akehata T and Shirai T 1972 Effect of light-source characteristics on the performance of circular annular photochemical reactor *J. Chem. Eng. Jap.* **5** 385 - 391

- Funayama H, Ogiwara K, Sugawara T, Ohashi H 1977 Light intensity profiles in photoreactors applied by a low pressure mecury lamp. Effect of spectral distribution of light source. *Kagaku Kogaku Rombunshu 3* 354-358

- Langmack K A 1997 An insight into the contributions of self-shielding and lamp reflectors to patient exposure in phototherapy units *Phys. Med. Biol.* **43** 207 - 214

- Martin C J and Pye S D 2000 A study of the directional response of Ultraviolet radiometers: II. Implications for Ultraviolet phototherapy derived from computer simulations *Phys. Med. Biol.* **45** 2713 - 2729

- Phillips R 1983 *Sources and applications of Ultraviolet Radiation* London: Academic Press

- Ryder 1997 *The Light Measurement Handbook* Newbury MA : International light technical publications department

Part II

Research and investigation

Chapter 5

Initial model approach

The relative merits of the radial, specular, diffuse and specific models have been discussed in the chapter 4. The radial model is under-pinned by the assumption that radiation is emitted perpendicular to the tube. As has been discussed this is not a realistic assumption but can give accuracy within 10% in limited situations. As the radial model is the most basic to implement, it was decided there may be some merit to experiment with the model and the kind of irradiance profile expected from such a source in order to gain insight into self-shielding on patient irradiance from first principles.

5.1 Simple Radial model

The form of the simple radial model has been mentioned in the preceding chapter; If all photons are emitted perpendicular to the tube, then the detector acts like it is on the surface of a cylinder emanating from the centre of the tube. Thus the irradiance at a point r any radial distance from the tube is of a reciprocal nature given by

$$E = S_L/2\pi r \tag{5.1}$$

where S_L is the power per unit length. For n such tubes at various points, this equation for irradiance at any point can be adapted from equation 5.1 by the

principle of superposition to become a summation.

$$E_{total} = \frac{S_L}{2\pi} \sum \frac{1}{r_1} + \frac{1}{r_2} .... + \frac{1}{r_n} \tag{5.2}$$

where r_i is the radial displacement from each respective tube to a point. Note that the radial model makes no allowance for direction of orientation of the detector relative to the source. For all intents and purposes, the incident angle $\theta = 0$ in all cases.

5.2 Simulating Radial model

A simulated radial model profile for a single tube at the centre of a $1m^2$ cabin is shown in figure 5.1. S_L was assumed to be unity in this implementation.

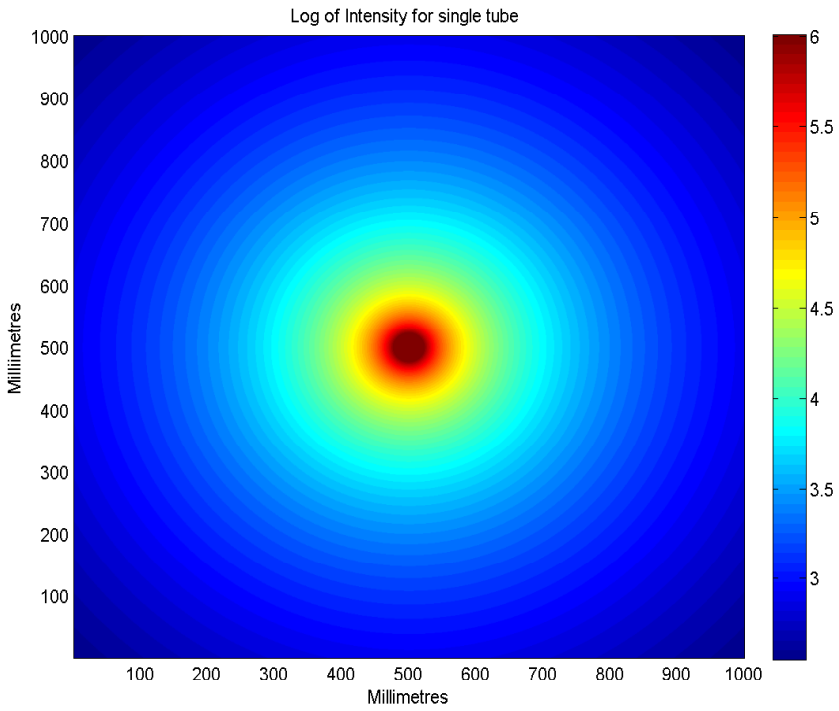

Figure 5.1: *Log of Irradiance from a single radial emitter at centre of a* $1m^2$ *cabin. Simulation is capped at 6 for clarity*

5.3 Obstruction in a radial model

The radial model is so basic an approximation that it is relatively straightforward to use it to examine obstructions. Two cases have been considered; one where the obstructing cross section is a circle and the case where the obstruction is elliptical. These were chosen as they are useful starting points for modeling cross sections of the human frame. The implementation of these test models is discussed herein.

5.3.1 Circular obstructions

Consider a circular obstruction, M, of radius R centred on *(g,f)* and a single tube, T, at point (T_x, T_z). Let D be the distance from T to the centre of M. Any point outside a circle has two tangent lines to that circle from that point. Tube T illuminates all points below the lower tangent line A and above the higher tangent line B, in addition to illuminating all points between the two tangent points outside the radius of the patient circle provided their displacement from the tube is less than D. For any point outside a circle, the bisector theorem states that the line from a point to the centre of the circle is an equal bisector of the angle subtended from that point to the two tangent lines.

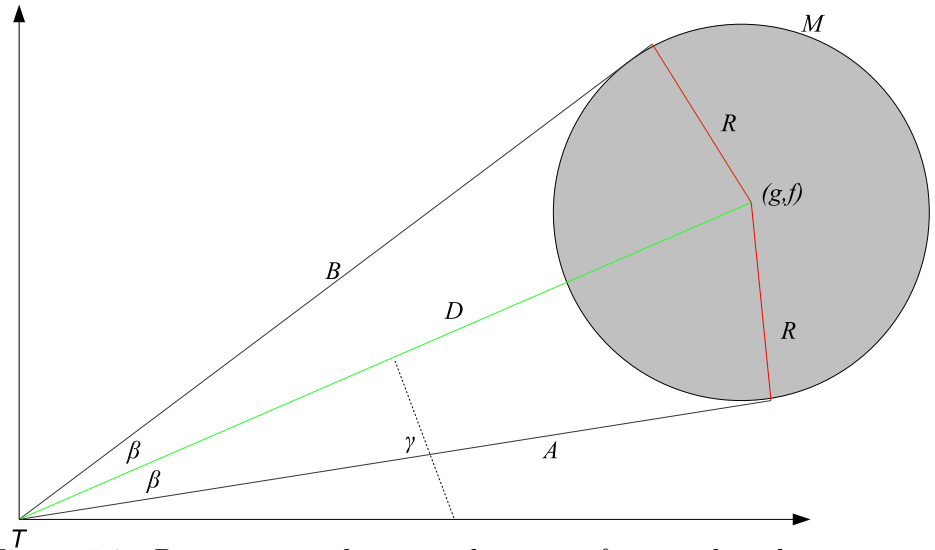

Figure 5.2: *Determining the critical extent of a circular obstruction*

We define the bisector angle as β, as shown in figure 5.2 and this angle is thus given by

$$\beta = \arcsin(R/D) \tag{5.3}$$

We define the angle between the centre of M and T as γ which is given by inverse tangent function as shown in equation 5.4. As trigonometric functions are multi-valued, it is advisable to use a more selective adaptation of the function, such as the `atan2` function found in many software packages which provides a single value in the correct quadrant and eliminates ambiguity. This becomes important when dealing with multiple tubes.

$$\gamma = \arctan[(f - T_z)/(g - T_x)] \tag{5.4}$$

Now, consider any point in the plane and let the angle between this point and the tube centre be given by ψ. There are two possible conditions, outlined here

$$|\{\gamma - \psi - \pi \mod 2\pi\} - \pi| \geq \beta \tag{5.5}$$

$$|\{\gamma - \psi - \pi \mod 2\pi\} - \pi| < \beta \tag{5.6}$$

For angles of ψ that satisfy the condition in equation 5.5, the point lies outside the critical extent of $\gamma \pm \beta$ and thus the irradiance simply governed by equation 5.2. For any points lying between the angular extents $\gamma \pm \beta$ by equation 5.6, the irradiance either obeys the prior relationship or is shielded by the patient and thus is zero. This latter case occurs inside the patient circle, and for all points beyond the patient relative to the emitting tube. If we consider a point inside the critical extent and define the distance from the centre of the patient circle to this point as W, then we measure the irradiance at a point a distance r from the centre of T,E_p to be zero if either of the following conditions hold

- (I) Points inside Patient circle M - Where $W < R$, it follows that $E_p = 0$.
- (II) Points beyond the patient - Where $r > D$, then $E_p = 0$.

The effects each of these conditions have on the final model is shown over an area of a metre squared in figure 5.3 for a tube T at $(0.2m, 0.1m)$ and a circular obstruction of radius $10cm$ centred at $0.5m, 0.5m$.

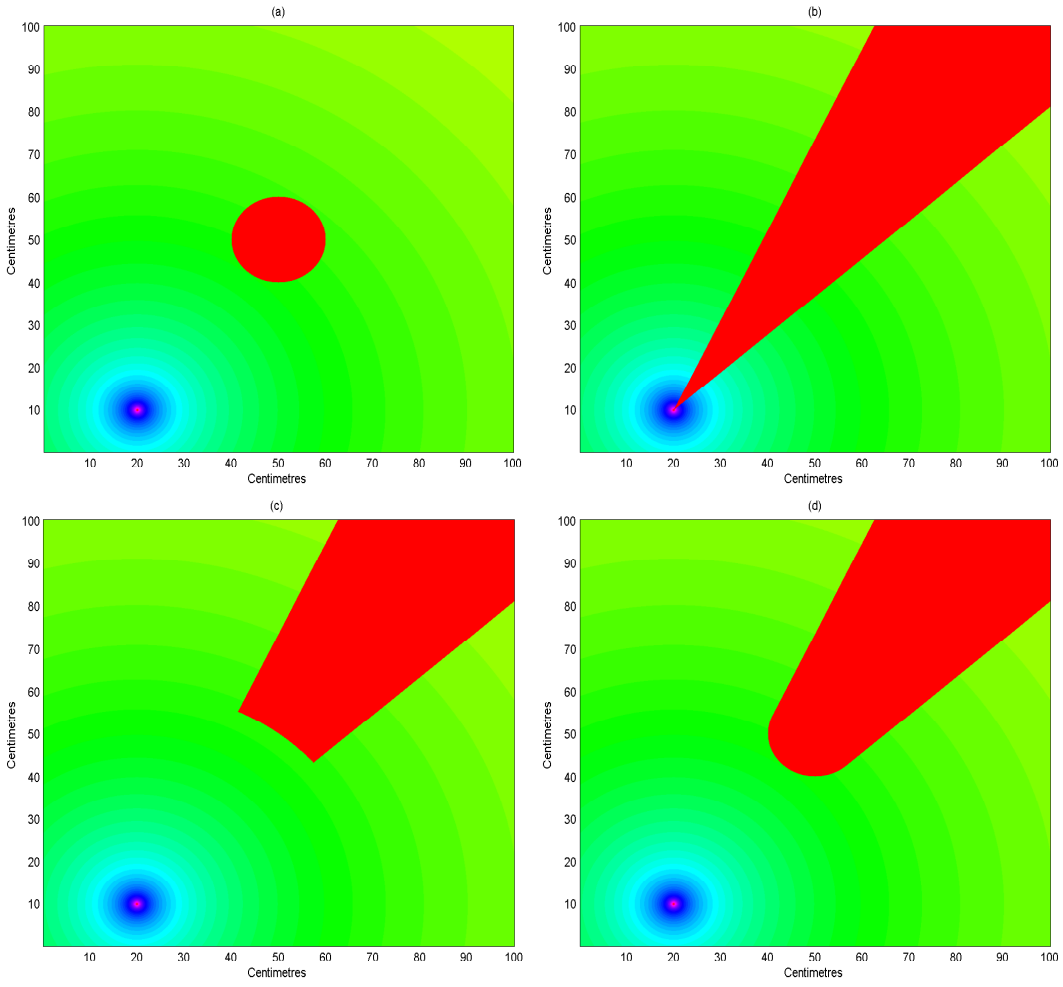

Figure 5.3: *Logarithmic plots of conditions for circular shielding (a) $E = 0$ inside circular obstruction (b) $E = 0$ between critical extent (c) $E = 0$ inside critical extent when $r > D$ (d) All conditions combined and satisfied*

5.3.2 Elliptical obstructions

While an ellipse is another conic section with many similarities to the circle, there are several key differences that make it more complicated to model. Like the circle, two tangent points can be drawn from any external point to the ellipse. However, unlike the circle, the bisector theorem does not hold for elliptical shapes; in practice, that means we need to go to greater lengths and less obvious methods to find the corresponding expressions defining the major critical extent $\gamma \pm \beta$. In addition, points outside the major critical extent are treated as in the circular cases, but the conditions for zero irradiance inside this critical zone must be modified.

5.3.2.1 Finding the tangent points from an external point to an ellipse

There exists an analytic and algebraic method and notation by Joachimsthal (Brannan *et al* 1999) for finding the tangent lines to any conic section. Any ellipse S with semi-axis of length a and b centred on *(h,k)* can be described fully by the equation

$$S = (\frac{x-h}{a})^2 + (\frac{z-k}{b})^2 - 1 = 0 \tag{5.7}$$

Any point on the ellipse satisfies this equation while any point outside the ellipse satisfies $S > 0$. This is the first condition for elliptical shading, as any point lying inside the ellipse will satisfy $S < 0$ and thus have zero irradiance. Joachimsthal notation can be used to describe any conic section and is of the form;

$$S_{ij} = Ax_ix_j + \frac{B}{2}(x_iz_i + x_jz_j) + Cz_iz_j + \frac{F}{2}(x_i + x_j) + \frac{G}{2}(z_i + z_j) + H \tag{5.8}$$

where i and j denote arbitary points P_i and P_j and A, B, C, F, G, and H are respectively the co-efficients of x^2, xz, z^2, x, z and the constant when the equation 5.7 is solved for any arbitrary values. The Joachimsthal notations for S_i and

S_{ii} are

$$S_i = Ax_i x + \frac{B}{2}(x_i z + x z_i) + C z_i z + \frac{F}{2}(x_i + x) + \frac{G}{2}(z_i + z) + H \tag{5.9}$$

$$S_{ii} = Ax_i^2 + B x_i z_i + C z_i^2 + F x_i + G z_i + H \tag{5.10}$$

It can readily be seen that S_i gives the equation of a line and S_{ii} produces a numerical value. The advantage of Joachimsthal notation is that it allows one to find the equations of the tangent pair at any point from a given conic through algebraic manipulation. A full discussion of the derivation and mathematics can be found in Brannan *et al* (1999) and Salmon (1896), but for our purposes it is sufficient to know that if a line is tangent to conic section, then it satisfies equation 5.11

$$S_i^2 - S.S_{ii} = 0 \tag{5.11}$$

When this equation is solved for a point, an expression is obtained that is the product of the two resultant tangent lines A and B. These equations of these lines are in the form $A = \kappa x + \varphi z + \mu = 0$ and $B = \upsilon x + \iota z + \nu = 0$ and it follows that the resultant expression is of the form

$$A.B = \kappa\upsilon z^2 + \varphi\iota x^2 + (\kappa\iota + \varphi\upsilon)zx + (\kappa\nu + \upsilon\mu)z + (\varphi\nu + \iota\mu)x + \mu\nu \tag{5.12}$$

One can factorize this expression and obtain the two line equations A and B from the point. From these line equations, one can find the slope of the lines and hence the angles formed with the ellipse. Factorizing an expression such as this can be computationally very difficult and can result in ambiguities, but one can avoid these difficulties if we consider the case where the co-efficient of z^2 in equation 5.12 is unity, so that $\kappa\upsilon = 1$; from this, it can be shown that in such a case, the co-efficients of x^2 and xz, denoted W_U and P_U respectively, are related to the

tangent line slopes m_1 and m_2 by

$$W_U = m_1 m_2 \tag{5.13}$$

$$P_U = -m_1 - m_2 \tag{5.14}$$

This method of evaluating W_U and P_U and hence the respective slopes of the tangent pairs only works when the co-efficient of z^2 is one. However, it is possible to manipulate the initial algebraic expression to obtain generalized expressions, W_G and P_G. For any external point *P(x,z)*, it can then be shown that

$$W_G = \frac{b^2 - (z-k)^2}{a^2 - (x-h)^2} \tag{5.15}$$

$$P_G = \frac{2(x-h)(z-k)}{a^2 - (x-h)^2} \tag{5.16}$$

These values are easily obtained from the input values for the ellipse centre *(h,k)*, axis lengths a and b and an external point *P(x,z)*, avoiding the use of symbolic manipulations and allowing calculation of the tangent points from the initial conditions. It is straightforward to use the quadratic formula to obtain values for m_1 and m_2. Furthermore, it can be shown that solving the quadratic expression for either m_1 or m_2 will actually yield both pairs of roots, so it is only required to solve the quadratic for m once, which is of the form $m^2 + Pm + W = 0$. This physically makes sense when we consider that we only expect two distinct values for the slope. If we denote the solution m_1 as the smaller of the two solutions, then the solutions to the quadratic take the form shown in equations 5.17 and 5.18.

$$m_1 = \frac{1}{2}(-P_G - \sqrt{P_G^2 - 4W_G}) \tag{5.17}$$

$$m_2 = \frac{1}{2}(-P_G + \sqrt{P_G^2 - 4W_G}) \tag{5.18}$$

If we solve tangent lines through T at (T_x, T_z) we get the slope of both tangent

lines and the point common to both these lines. Thus, we can readily ascertain the equations of both lines. These equations are

$$A = z - T_z - m_1 x + m_1 T_x = 0 \tag{5.19}$$

$$B = z - T_z - m_2 x + m_2 T_x = 0 \tag{5.20}$$

These lines intersect once each with the ellipse. The ellipse equation is a polynomial of the second order, and the line equation a polynomial of the first order, and as the very definition of a tangent to a boundary is a line that touches that boundary just once, is it possible to show that the solution to both sets will be repeated root. This can be verified by checking the discriminant of the quadratic equation is zero, and indeed this is what we physically expect. Now we define the point where the tangent line A of slope m_1 intersects the ellipse as *(r,t)*, and solve for r and t by

$$r = \frac{hb^2 + km_1a^2 - m_1a^2(T_z - m_1T_x)}{b^2 + m_1^2a^2} \tag{5.21}$$

$$t = m_1(r - T_x) + T_z \tag{5.22}$$

By the same logic, defining the point at which the tangent line B of slope m_2 intersects the ellipse as (p, q), we solve for p and q by

$$p = \frac{hb^2 + km_2a^2 - m_2a^2(T_z - m_2T_x)}{b^2 + m_2^2a^2} \tag{5.23}$$

$$q = m_2(p - T_x) + T_z \tag{5.24}$$

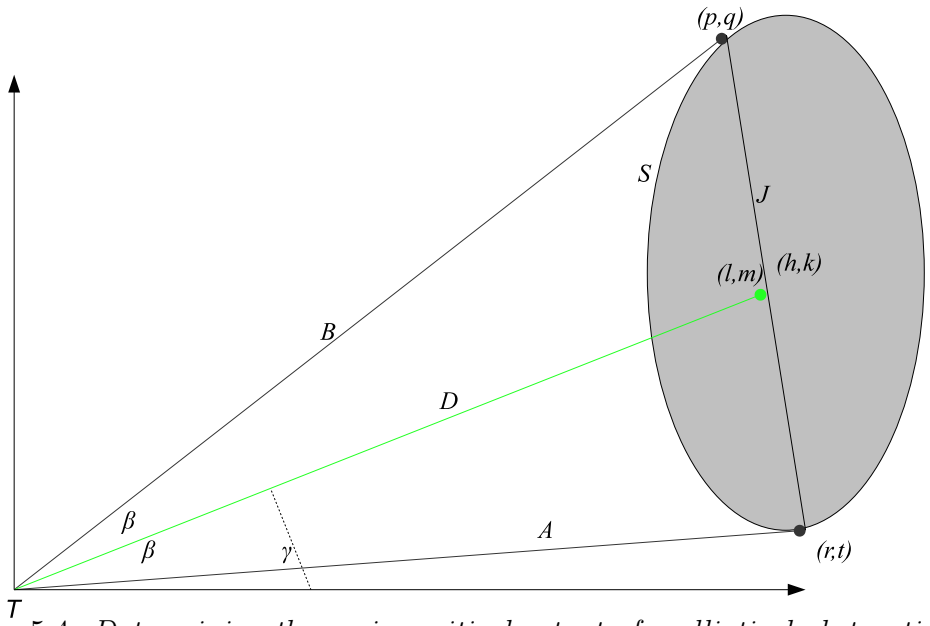

Figure 5.4: *Determining the major critical extent of a elliptical obstruction*

5.3.2.2 Ascertaining the major critical extent

As in the circular case, we wish to find the bisector angle between the two tangent lines. In the circle case, this was trivial as the bisector theorem states the angle between the point and the circle centre is the bisector. In an ellipse, however, this is not the case, and we need a method to generalize finding the bisector point *(l,m)* as shown in figure 5.4. This point lies on the line D which evenly bisects the tangent lines A and B. This slope of this line, m_D , is given by

$$m_D = \tan(\frac{\arctan m_1 + \arctan m_2}{2}) \tag{5.25}$$

Knowing that (T_x, T_z) also lies on this line, we can readily obtain the line equation. Now consider the line joining the two tangent points *(r,t)* and *(p,q)*. We call this line J and the slope of which is easily calculated as

$$m_J = [t - q]/[r - p] \tag{5.26}$$

The point *(l,m)* lies on J as well as on D and thus we can solve these first order polynomial equations to obtain a value for the bisector point. The solutions for l and m take the form

$$l = (m_J r - m_D T_x + T_z - t)/(m_J - m_D) \tag{5.27}$$

$$m = m_J(l - p) + q \tag{5.28}$$

Now, having solved the bisector point, we can ascertain the angle γ by a method analogous to the method in circular method.

$$\gamma = \arctan[(m - T_y)/(l - T_x)] \tag{5.29}$$

Now we need a value for β as in the previous case so that we can describe the critical extent $\gamma \pm \beta$. Because all side lengths of the triangle (T_x, T_z), *(r,t)* and *(p,q)* can be calculated, one can invoke the cosine rule to solve for the angle.

$$\beta = \frac{1}{2}\arccos\left(\frac{|A|^2 + |B|^2 - |J|^2}{2|A||B|}\right) \tag{5.30}$$

Thus, analogous to the circular case for any angle ψ, the irradiance effects described by equations 5.5 and 5.6 hold, so that outside the angular extent $\gamma \pm \beta$, the irradiance is otherwise unaffected and obeys equation 5.2.

5.3.2.3 The minor critical extent and cosine tracing method

Unlike a circle, points on an ellipse are not all equidistant from the centre of the ellipse. For this reason, the act of drawing a line or arc that connects the two tangent points and stays within the confines of the ellipse can be a complicated undertaking, and for any simulation to be successful, we need a generalized method of finding such a line. One effective way of doing this is to consider the

points (T_x, T_z), *(r,t)* and *(p,q)* as three points of a circle and to locate the circumcentre of these inscribed points. We call this point *(w,v)* and it has the property of being equidistant from each of the three inscribed points. The circumcentre lies on the intersection of lines drawn perpendicular to the midpoints of each the three lines. Knowing that the product of the slopes of perpendicular lines is minus one, it can shown that the slopes of the $A_\perp$ and $B_\perp$ are respectively

$$m_{A_\perp} = [(T_x - r)/(t - T_z)] \tag{5.31}$$

$$m_{B_\perp} = [(T_x - p)/(q - T_z)] \tag{5.32}$$

The points through which these lines pass through are given by the midpoints of the the tangent lines and are thus

$$A_\perp x, A_\perp z = \frac{T_x + r}{2}, \frac{T_z + t}{2} \tag{5.33}$$

$$B_\perp x, B_\perp z = \frac{T_x + p}{2}, \frac{T_z + q}{2} \tag{5.34}$$

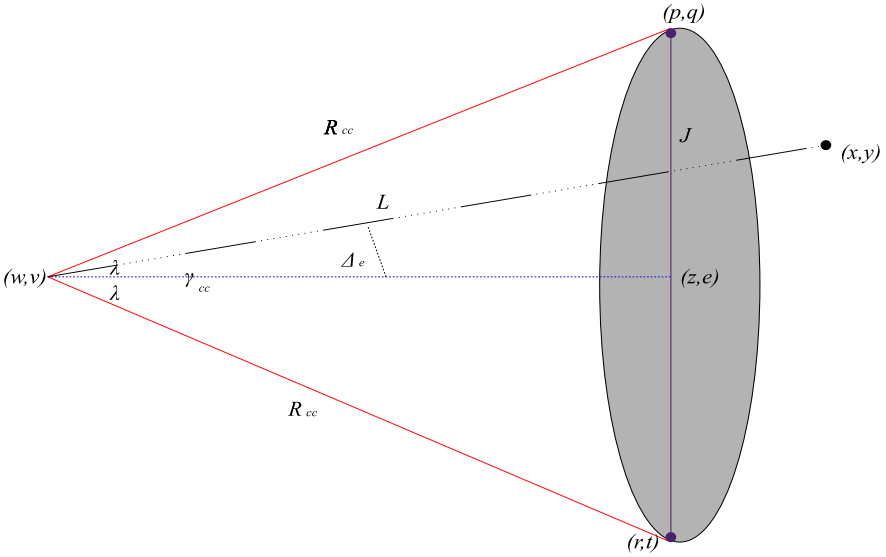

Figure 5.5: *Determining the minor critical extent of a elliptical obstruction*

This gives us enough information to find the circumcentre which corresponds to the intersection of these perpendicular lines. The solution for *(w,v)* is then

$$w = \frac{m_{B_\perp} B_\perp x - m_{A_\perp} A_\perp x + A_\perp z - B_\perp z}{m_{B_\perp} - m_{A_\perp}} \tag{5.35}$$

$$v = m_{B_\perp}(w - B_\perp x) + B_\perp z \tag{5.36}$$

Finding the radius of this circle, denoted as R_{cc} is straightforward, as it is distance from *(w,v)* to any of the points. A line of length R_{cc} traced from tangent point *(r,t)* to tangent point *(p,q)* produces an arc spanning the ellipse, and it is tempting to think think that this condition in combination with the $S < 0$ condition fully describes the non illuminated regions and this is very near the truth; however, a condition which states that anything beyond the arc is non-illuminated is too simplistic as it can result in impossible regions of illuminations behind the ellipse. The solution is to modify this arc into a straight line joining the two tangent points, so that it is always inside the ellipse. First, we call the half angle between *(w,v)* and either of the tangent points λ, defined as

$$\lambda = \frac{1}{2} \arccos\left(\frac{2R_{cc}^2 - |J|^2}{2R_{cc}^2}\right) \tag{5.37}$$

Now, consider the line J connecting the tangent points; consider the midpoint of this line and define this point as (z, e), which can be deduced as previously shown in equations 5.33 and 5.34. Thus, the effective zero angle relative to the circumcentre γ_{cc} is defined as

$$\gamma_{cc} = \arctan[(e - v)/(z - w)] \tag{5.38}$$

Now we have an new angular extent of $\gamma_{cc} \pm \lambda$, which we call the minor critical extent, as shown in figure 5.5. We define the angle Δ as the angle between any

point and the circumcentre *(w,v)*. If we further define the angle Δ_e as the effective angle with respect to γ_{cc} we can prove

$$\Delta_e = |\gamma_{cc} - \Delta| \tag{5.39}$$

Using the sine rule and various other trigonometric manipulations, it is possible to show that the for any angle of Δ_e lying within the minor critical extent is a distance r_J from J given by

$$r_J = R_{cc}|\frac{\cos\lambda}{\cos\Delta_e}| \tag{5.40}$$

Thus, for any point within the minor critical extent, the irradiance is zero when the distance from the point to the circumcentre is greater than r_J, provided that point is still inside the major critical extent. Points which lie inside the minor critical extent and beyond r_J yet outside the major critical extent are still illuminated. We can then combine all these conditions to fully describe an elliptical obstruction, and this is illustrated in figure 5.6 for tube T at $0.2m, 0.4m$ and an obstruction with $a = 5cm$ and $b = 20cm$ centred at $0.5m, 0.5m$.

Despite the simplicity of the radial model, the elliptical obstruction conditions are quite intensive and mathematically involved.

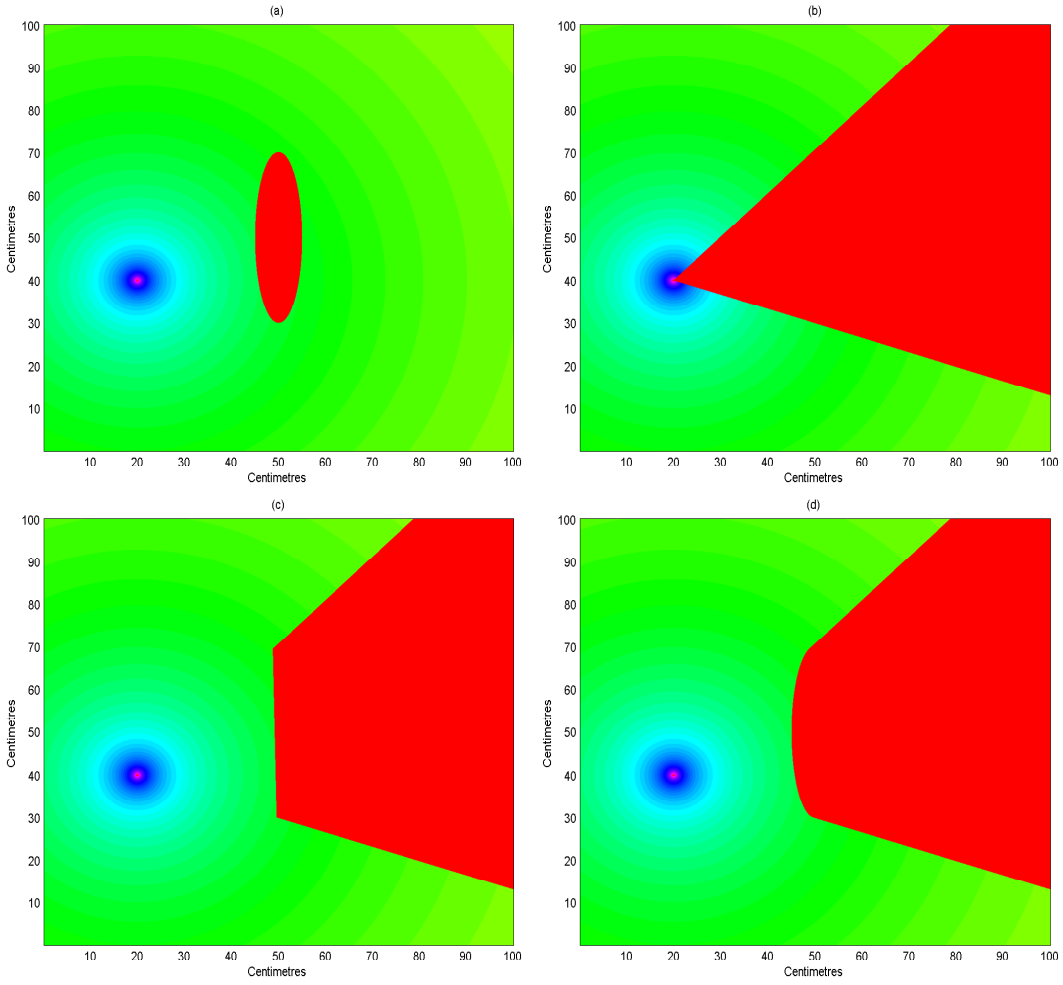

Figure 5.6: *Logarithmic plots of conditions for elliptical shielding (a)* $E = 0$ *inside ellipse (b)*$E = 0$ *inside critical extent (c)* r_J *condition in minor critical extent (d) All conditions combined*

Table 5.1: Hypothetical Patient Attributes

Patient Attribute	Typical total value	Semi-major / minor value
Head Length	188 mm	94 mm
Head Breath	145 mm	72.5 mm
Shoulder Breath	438 mm	219 mm
Hip breath	387 mm	193.5 mm
Abdominal depth	237 mm	118.5 mm
Knee Radius	57.3 mm	57.3 mm
Knee spacing	110 mm	110 mm

5.3.3 Radial cabin with patient

Multiple source irradiance can be modeled as it is a cumalative effect. Thus, it is possible to model the effects of multiple sources for the radial model by simulating the effects for each tube and summing all these effects. Table 5.1 gives the average DINBelg (DINBelg 2005) dimensions of elements of human anatomy, all of which approximate elliptical shapes with their own respective semi-major / semi-minor axis values. The effects of multiple tubes arranged in an array similar to that encountered in a Waldmann UV-1000 cabin impinging on a patient standing at the centre is shown in figure 5.7 for various anatomical heights - head, shoulders, waist and knees. The Waldmann unit in this situation has 26 tubes and no reflections are assumed.

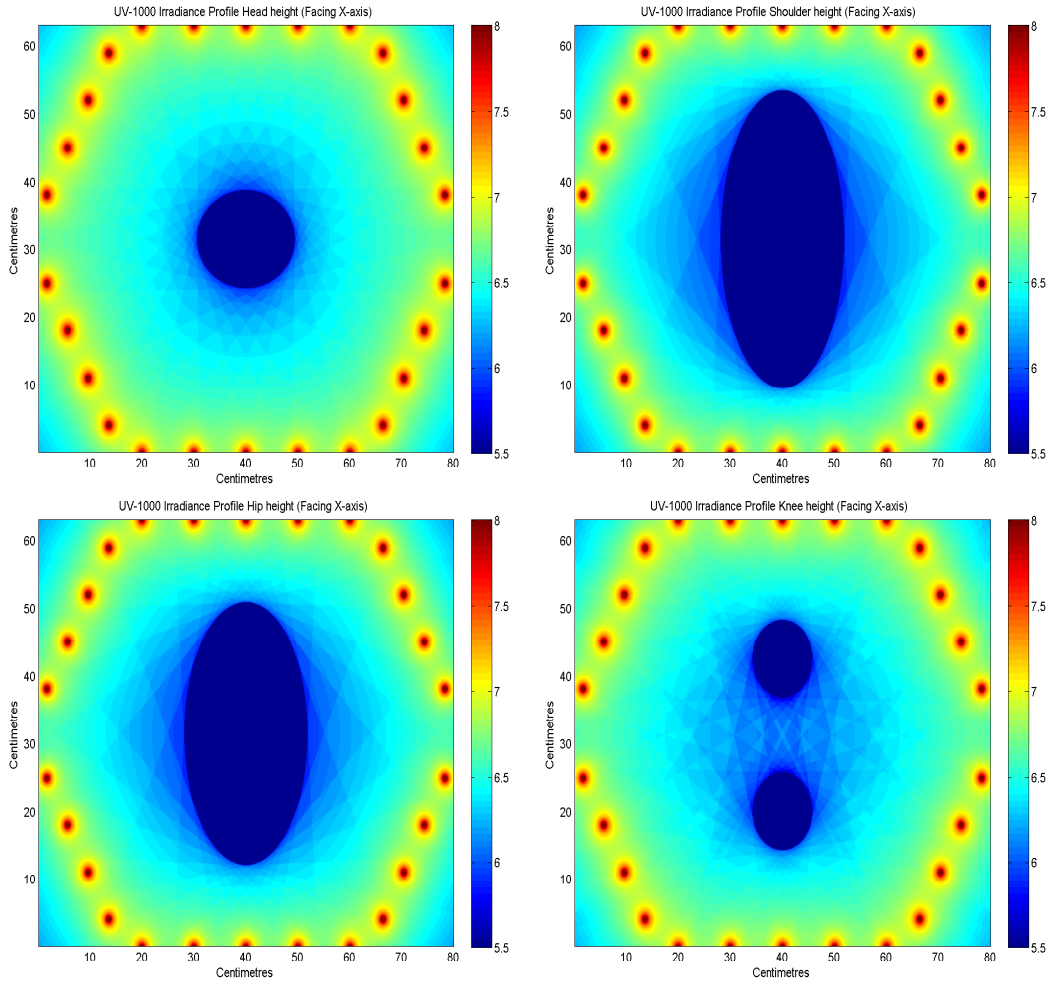

Figure 5.7: *Logarithmic plots of UV-1000 array irradiance at different vertical heights along a patient assuming radial model. Clockwise from top left - Head, Shoulds, waist and knees.*

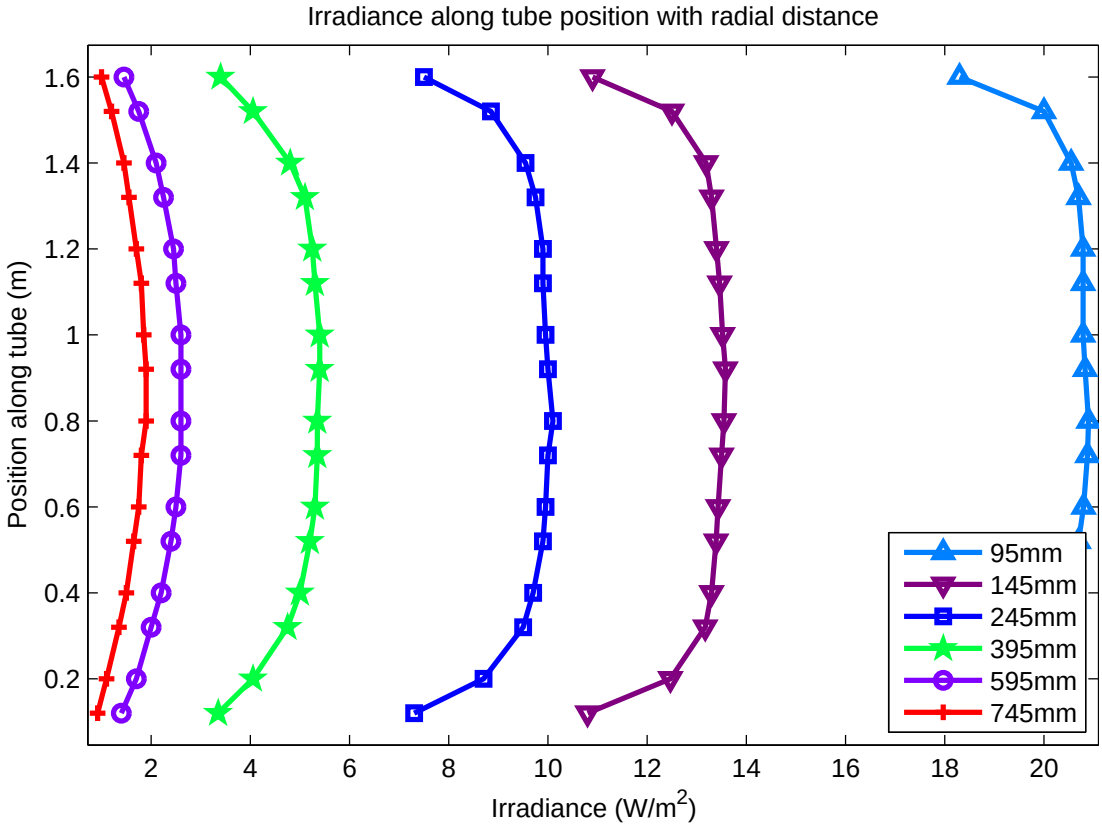

Figure 5.8: *Variation of irradiance along length*

5.4 Applicability of the radial model

The radial model relies on a major simplification, namely that all radiation is emitted perpendicular to the surface. While this is false, in certain situations it can approximate reality to within 10%. The outstanding question is whether this is the case in UVR phototherapy. In a radial emitter, at any given distance the detector will record the same value regardless of vertical position along the tube length. Figure 5.8 shows the actual recorded irradiance along the tube length with increasing distance from the tube centre (see experimental procedure in chapter 8 for an outline of this experiment). In the middle of the tube length the irradiance stays consistent and drops off near the tube edges. This effect becomes more pronounced as radial distance from the tube centre increases. The equation for the radial models as given in equation 5.1 implies the irradiance is inversely proportional to the radial distance. This equation can be rewritten as

$$E = C/r \tag{5.41}$$

where C is a constant. The measured values of E from the midpoint of the tube with increasing radial distance were contrasted with the expected irradiance from a radial model. The constant C was found by setting the first measured value and rearranging $C = Er$ which yielded a value of $1.9552W/m$. The comparison between the radial model and measured values is shown in figure 5.9. The relative error with distance is shown in table 5.2.

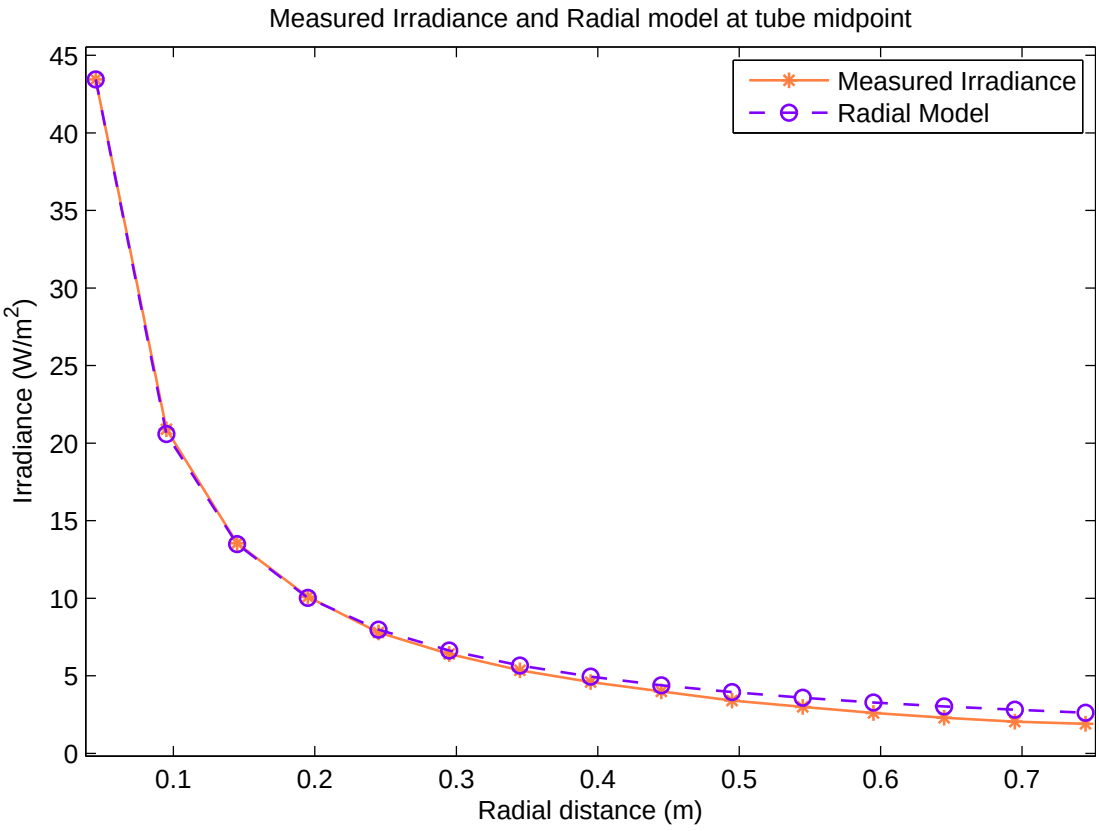

Figure 5.9: *Irradiance error with distance in radial model*

Table 5.2: Percentage error for radial model

Distance (mm)	**Error** %
45	0
95	1.5235
145	0.4835
195	0.7235
245	2.3155
295	3.5620
345	5.9325
395	7.6087
445	9.8455
495	16.1765
545	19.5872
595	26.3898
645	31.7998
695	37.2346
745	38.1314

In this particular case, the radial model has an error of less than 10% up to 445mm from the tube centre. Thereafter the error increases as the irradiance falls off much faster than the model predicts. It is then tempting to think that the radial model is a then good approximation up to this point but this is not in fact the case; The radial model makes no concession for incident angle and by its very nature cannot be easily modified to do so. In the case depicted in figure 5.9, the detector was directly facing the tube and at zero inclination. In this case, the radial model can work quite well as illustrated. However, in any case where the detector is not directly facing the source and is in any way inclined, the radial model entirely breaks down, rendering it unsuitable for all but very specific applications in the near-field.

5.5 Conclusions

While the radial model is simple and seemingly a good starting point, there are several factors that render it unfit for the purpose of irradiance modeling and dosimetry

1. The model itself has questionable reliability as the major assumption it makes regarding radiation emission is demonstratably false; this produces small errors in the immediate vicinity of the tube, but breaks down quickly further away.

2. The radial model cannot allow for the angle which radiation is received. In reality this will affect the overall irradiance quite drastically but the model can only handle situations where the detector has no inclination.

3. Obstruction modeling with the radial model is complex and again the problem of incident angle presents itself.

In conclusion, the radial model is not adequate for dosimetry and a new, more robust model must be developed to handle clinical situations.

5.6 References

- DINBelg: Body dimensions of the Belgian population (2005)

Chapter 6

Construction of a rigorous lamp source model

Initial research led to the conclusion that the approach examined in chapter 5 was only sufficient to characterize UVR sources in very limited situations. For this reason, it became important to research other types of models that are more promising.

6.1 A new Line source model

Line sources are one dimensional source geometries with a finite extent. In the field of ultraviolet phototherapy, reference has been made to this specific model geometry before (Martin and Pye 2000) as a method of approximating tube behaviour. Martin and Pye's model has been discussed in chapter 4, and can be an effective ad hoc system in certain cases. The aim here is to examine this concept from first principles in order to construct a formalized computational dose model. A line source is a linear array of point sources, and it is important to revisit some important radiometric definitions in order to ascertain an expression for the irradiance from a point source. Radiometric quantities can have a certain degree of ambiguity depending on the field in which they are being applied, but have been defined well for photobiology by Sliney (2007).

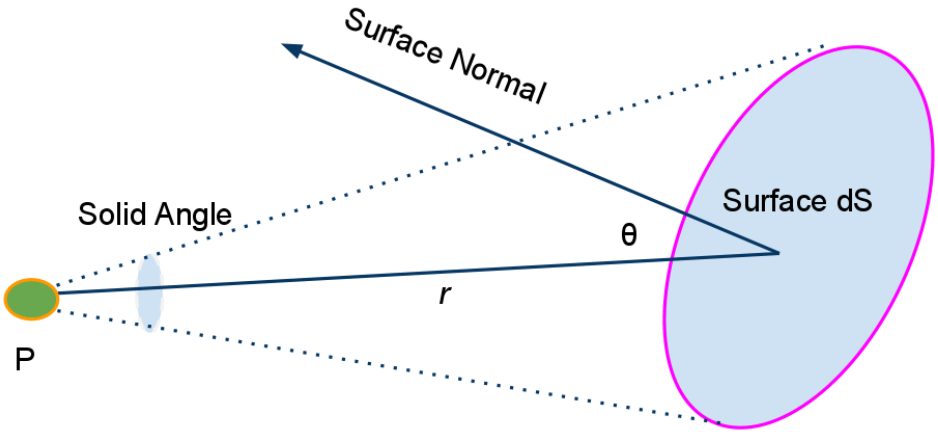

Figure 6.1: *Point irradiance upon an inclined plane*

Irradiance (E) is the quotient of the radiant power incident upon an element of surface containing that point divided by the area of that element. The radiant intensity (I) is the quotient of the radiant power leaving the source in a direction divided by the solid angle made in that direction.

$$E = d\Phi_E/dS \tag{6.1}$$

$$I = d\Phi_E/d\Omega \tag{6.2}$$

The situation for a point source a distance r from a detecting area inclined with angle θ is shown in figure 6.1. It is possible to calculate the solid angle and manipulate the identities established in equations 6.1 and 6.2 to get an expression for irradiance from the point source.

$$d\Omega = dS\cos\theta/r^2 \tag{6.3}$$

$$E = I\cos\theta/r^2 \tag{6.4}$$

So the expression for irradiance from a point source has both a cosine dependence and an inverse square law relationship. Assuming diffuse radiation, the radiant intensity is a constant per unit length given by equation 4.6

$$I = S_L/\pi^2 \tag{6.5}$$

As the line source is a linear array of such point sources, the radiant intensity of a line source can be considered to be approximately constant without loss of generality. Recalling that a simple line source model is a linear array of point sources, it stands to reason that the irradiance from a line source in the integral of the points sources along the entire length of the source. This is expressed in equation 6.6

$$E = \frac{S_L}{\pi^2} \int \frac{\cos\theta}{r^2} dl \tag{6.6}$$

The cosine between the surface normal of the detector $\vec{n}$ and the radial vector $\vec{r}$ is given by the dot product as expressed in equation 6.7

$$\cos\theta = \frac{\vec{n} \cdot \vec{r}}{|n||r|} \tag{6.7}$$

This identity allows the form in 6.6 to be written in vector terms without the direct inclusion of the cosine identity. Re-writing S_L/π^2 as S_R, the reduced constant, this is expressed explicitly in equation 6.8.

$$E = S_R \int \frac{\vec{n} \cdot \vec{r}}{|n||r|^3} dl \tag{6.8}$$

The question that immediately arises is whether there are any explicit solutions for the equations 6.6 or 6.8 and what the forms of these solutions might be.

6.1.1 Solutions of the new model

6.1.2 Simple case solution

The simple case to solve is when there is a detector or element of skin directly facing a line source, such as that illustrated in figure 6.2. In this case, the cosine can be expressed in terms of d and l as

$$\cos\theta = d/r = d/\sqrt{d^2 + l^2} \tag{6.9}$$

And accordingly, equation 6.8 can be expressed

$$E = \int \frac{S_R \cos\theta}{r^2} dl = \int \frac{S_R d}{(d^2 + l^2)^{3/2}} dl \tag{6.10}$$

This expression can also be solved analytically for the entire length of the tube by integrating with respect to l between the limits of $L - h$ and h, and results in a expression, $E(h, d)$, for a detector as shown in equation 6.11.

$$\underset{\text{UV Lamp}}{E(h,d)} = S_R[\frac{L-h}{d\sqrt{d^2 + (L-h)^2)}} + \frac{h}{d\sqrt{d^2 + h^2}}] \tag{6.11}$$

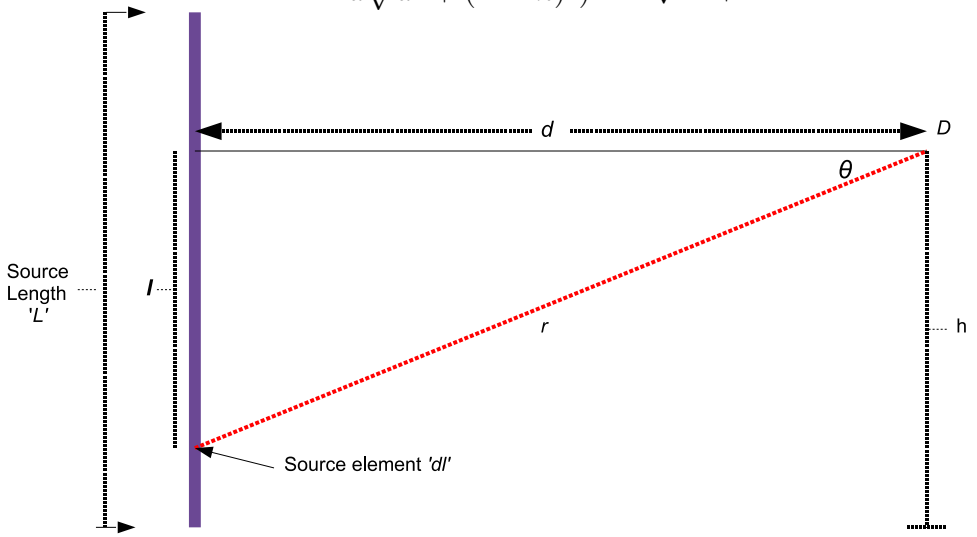

Figure 6.2: *A detector of area dS at a distance* r *from point source at* P

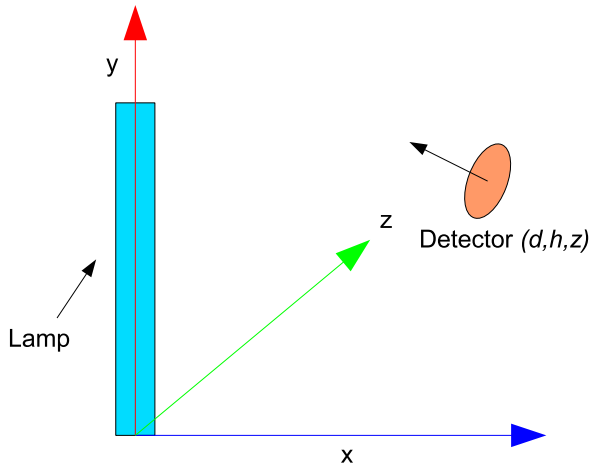

Figure 6.3: *Vector orientation for general case: The detector is inclined relative to the lamp and not directly facing the source*

6.1.3 General case solution

The simple solution gives the irradiance for detectors and surface elements focused directly upon the line source. However, in practice detectors and human epidermis will oftentimes be at various orientations to the source and thus a more robust solution is required to examine the majority of cases. A surface normal has the equation

$$\vec{n} = (A\vec{x} + B\vec{y} + C\vec{z}) \tag{6.12}$$

where $\vec{x}$, $\vec{y}$ and $\vec{z}$ are orthogonal vectors and $\vec{y}$ is the vector along the length of the lamp as in figure 6.3. If the centre of the detecting surface is at (d, h, z) and the source standing on the origin, then the radial vector is

$$\vec{r} = (-d\vec{x}, -l\vec{y}, -z\vec{z}) \tag{6.13}$$

The identity in equation 6.8 can then be written as

$$E = \frac{-S_R}{\sqrt{A^2 + B^2 + C^2}} \int \frac{Ad + Bl + Cz}{\sqrt{d^2 + z^2 + l^2}^3} dl \tag{6.14}$$

Integrating between the limits of $L-h$ and $-h$ and rewriting the $\sqrt{A^2+B^2+C^2} = |n|$ for clarity, this can also be solved analytically, giving the general expression for irradiance for any surface normal.

$$E = \frac{-S_R}{|n|(d^2+z^2)}[\frac{(Ad+Cz)(L-h)-B(d^2+z^2)}{\sqrt{d^2+z^2+(L-h)^2}} + \frac{(Ad+cz)(h)+B(d^2+z^2)}{\sqrt{d^2+z^2+h^2}}] \quad (6.15)$$

This analysis yields the general case for a detector or epidermal surface at any orientation relative to the source. This equation produces negative values of E when the absolute angle between the $\vec{n}$ and $\vec{r}$ vectors is greater than $\pi/2$ so care must be taken to ensure that simulated irradiance is forced to zero when a negative value occurs. This arises because cosine is negative between $\pi/2$ and $3\pi/2$. However, at these angles the radiation is not incident upon the surface and thus it can be safely set to zero in any simulation. The general equation derived can handle any orientation. This analysis can also be done for an extended source but results in a non-analytical utterly unwieldy expression as outlined in appendix B. Consider the orientation in the simple case. Then the normal vector becomes

$$\vec{n} = (-1\vec{x} + 0\vec{y} + 0\vec{z}) \quad (6.16)$$

Thus the general equation reduces to

$$E = \frac{-S_R}{(d^2)}[\frac{(-d)(L-h)}{\sqrt{d^2+(L-h)^2}} + \frac{(-d)(h)}{\sqrt{d^2+h^2}}] \quad (6.17)$$

Which further reduces to

$$E = \frac{S_R}{d}[\frac{L-h}{\sqrt{d^2+(L-h)^2}} + \frac{h}{\sqrt{d^2+h^2}}] \quad (6.18)$$

Which is the identify derived for the simple case in equation 6.11.

6.2 Determining S_L and S_R

S_R gives a normalization constant for the model. If the UV tubes are well described by a line source model, then determining S_R is experimentally possible by contrasting the simulated results with a constant of unity at some point, E_U with the irradiance experimentally measured at the same point, E. Thus for a consistent line source emitter, S_L can be determined by

$$S_L = \pi^2 S_R = \pi^2 \frac{E}{E_U} \tag{6.19}$$

The result obtained should be relatively consistent for values chosen if the model is sufficiently robust and describes the emission well. However, improved accuracy is expected further away from the tube ends where there may be scatter effects and obstruction from the lamp anode / cathode elements.

6.3 Conclusions

The new model derived here has several advantages over models previously available and those discussed in chapter 5. The main features that make the model so advantageous are

1. **Accounts fully for incident angles** This model handles all potential cases by fully solving the surface normal cases. It can thus account for irradiance from any angle with respect to the source, rendering it extremely useful.

2. **Completely Analytical** The new model does not rely on summations from discrete elements, instead factoring in all source contributions. This is in stark contrast to previous models.

3. **Instantly applicable** The other models discussed required modification for various cases that might arise; the new model works regardless of initial conditions, provided one has a measure of the S_R, which is in theory easily measured.

Chapter 7

Experimental investigation of new source model

The source model derived in chapter 6 requires experimental verification to determine its predictive power and applicability. Two experiments were designed to examine this - A relatively straightforward 'chart-recorder' style experiment for the simple case and a more complex rotating detector procedure to examine the general case.

7.1 Investigating the simple case

7.1.1 Experimental procedure

In this experiment, a Phillips 100W TL-01 lamp was analyzed in a 'chart-recorder' set-up; the tube was rigged independently of the cabin with the detector directly facing the tube centre so the irradiance could be recorded as a function of radial distance from the tube centre (d) and position along the tube length (h). TL-01 bulbs are narrow-band UVB with emissions at $311nm$. A standard Phillips ballast was used to power the tube. The detector was a calibrated IL1400A handheld meter with an SEL240 UVB probe [International light, Massachusetts] with a PFTE filter and low f_2, designed to detect this radiation. The experimental set up is illustrated in figure 7.1.

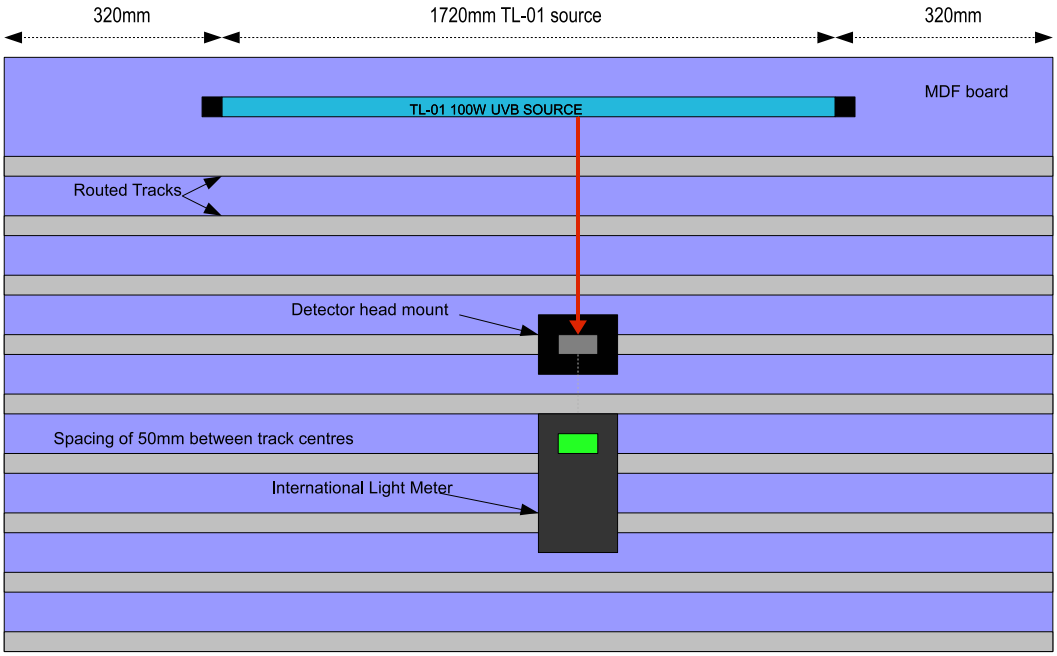

Figure 7.1: *Routed experimental MDF board, with 50mm tracks equidistant.*

The rigging was mounted on a sturdy medium density fibreboard (MDF) which had tracks routed in it at equidistant 50mm intervals. The tube diameter was measured at 37mm. The head of the IL meter detector was placed in a specially designed mount engineered to slide inside the routed tracks, allowing variation in the plane parallel to the tube 'length', as shown in figure 7.2. This mount was blackened to reduce any scatter or reflection. The TL-01 tube source was placed on similarly blackened mounts and attached to the ballast, with 1720mm of tube visible. The rig was designed to ensure the tube mounts and the detector mounts kept the tube and detector at equal heights at all points.

In addition to the primary IL400A meter for taking measurements, an independent *sglux* [sglux, Berlin] sensor and UVB probe were set along side a digital thermometer to examine whether the tube output changed significantly during the experiment. The tube was left operating for approximately ten minutes until the sglux monitor showed a stable reading.

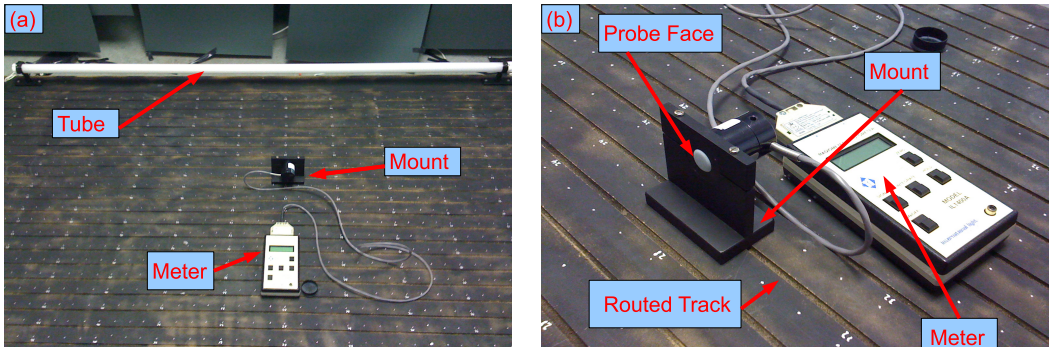

Figure 7.2: *(a) 'Chart recorder' board (b) View of the mount and detector*

Measurements were taken from the first routed track, which was 26.5mm radially from the tube (45mm from centre) to 745mm from centre. Along the other plane, measurements were taken in increments of 40mm. Changes in temperature and baseline UVB were recorded. Temperature varied between 18.8 and 21 degrees celsius. During measurements, the UVB output recorded by the secondary meter showed no change once the tube had warmed up, indicating consistency for results taken with the primary meter. At all points multiple readings were taken and the results averaged. These were taken at different times to ensure repeatability.

All reflective surfaces were covered with black matt board to reduce incidences of reflection or scatter of ultraviolet radiation back into the radiometer, and to this end the MDF board was coated in matt black spray paint to minimize the reflectance. The reflectance of the matt-black board and blackened mounts were examined by measuring background UV readings with and without tube output at different angles. The reflectance was found to be negligible at all measurement points.

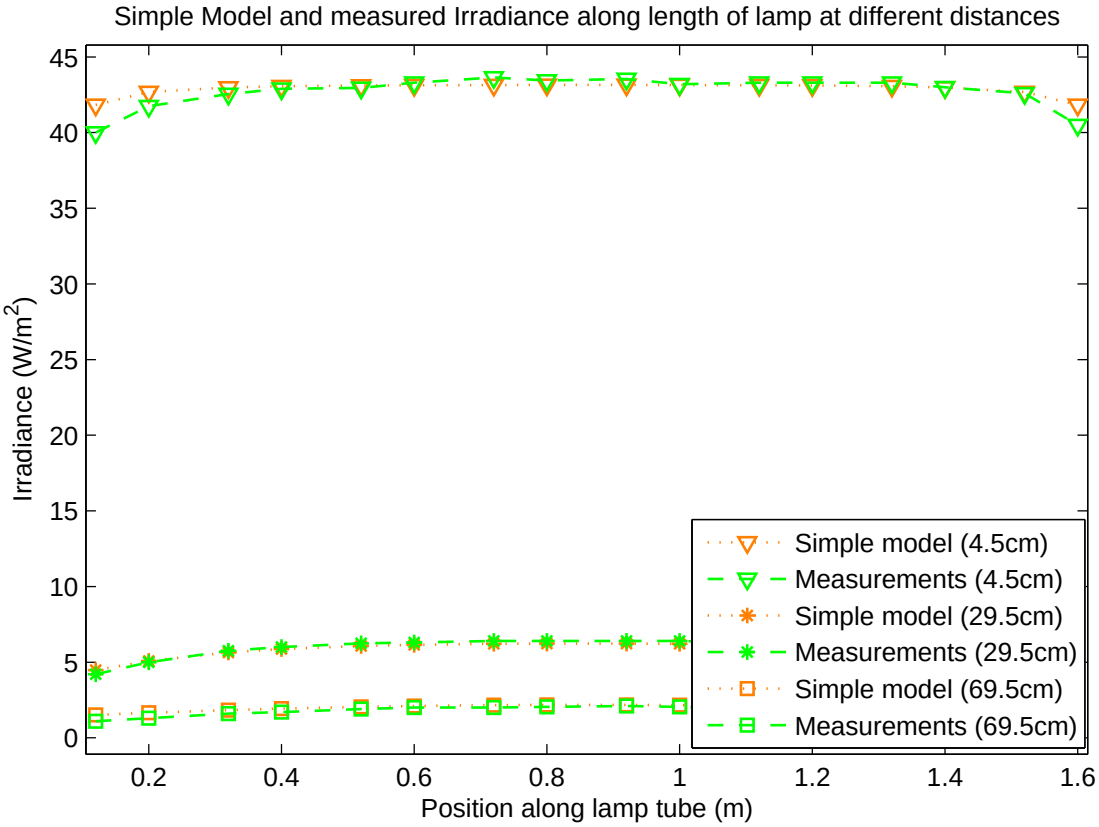

Figure 7.3: *Comparison of simple model normalized at* $495mm$ *with measured values along the length of lamp. Distances from lamp centre of* $45mm$. $295mm$ *and* $695mm$ *are shown.*

7.1.2 Simple case results

Results from the simple case were highly encouraging; The model and measured irradiance with various values of h along the tube is shown in figure 7.3 for $d = 0.045m$, $d = 0.295m$ and $d = 0.695m$ to illustrate the high level of agreement between simulated and actual values. The determined S_R in this particular figure is taken at the centre of the tube a distance of $0.495m$ away from the centre; S_R varied very little regardless of chosen normalization distance and length along tube; this implies that the model is robust and has a high level of accuracy. The goodness of fit data (co-efficient of determination) shown in table 7.1 highlights minimal impact of normalizing at various points. This high value for r^2 and low variance strongly imply the model is accurate in this situation.

Table 7.1: Goodness of fit for simple model

Tube edge distance	r^2 normalized at $45mm$	r^2 normalized at $745mm$
$120mm$	0.9956	0.9989
$200mm$	0.9983	0.9981
$320mm$	0.9992	0.9974
$400mm$	0.9996	0.9972
$520mm$	0.9996	0.9971
$600mm$	0.9998	0.9965
$720mm$	0.9997	0.9957
$800mm$	0.9997	0.9960
$920mm$	0.9998	0.9959

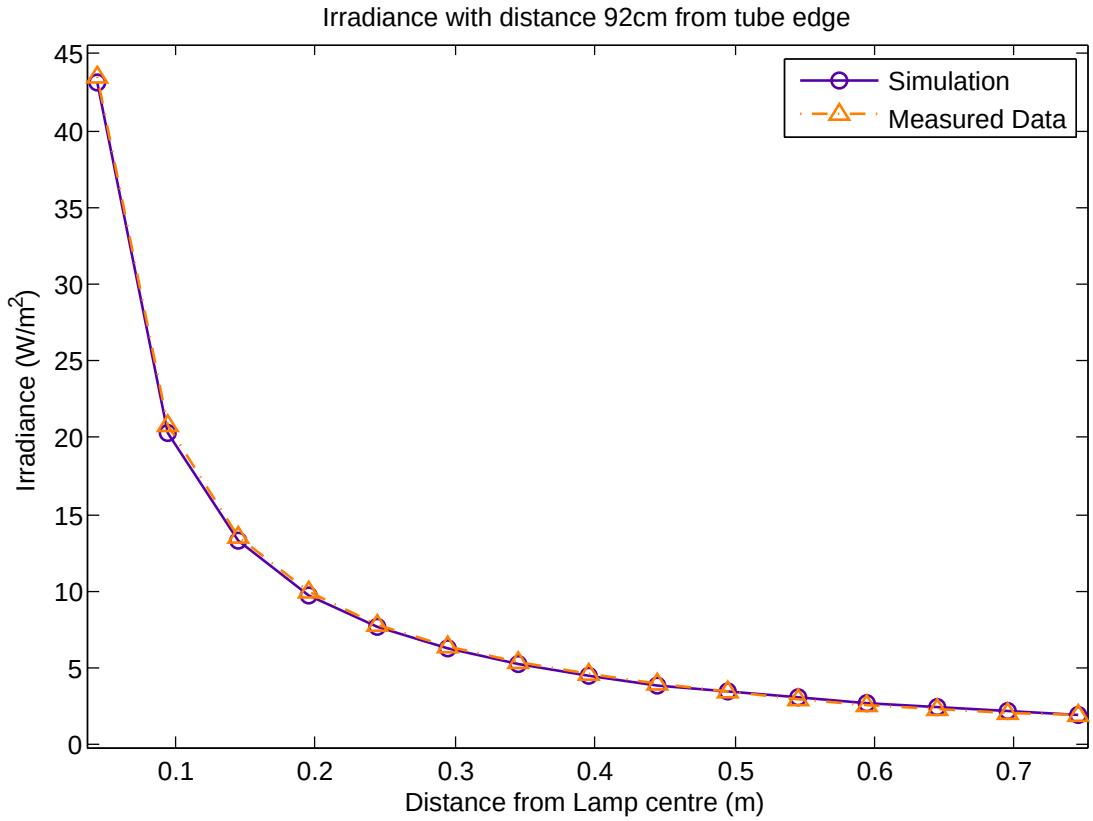

Figure 7.4: *Comparison of simple model normalized at* 495*mm with measured values,* 920*mm from tube end. The measured and simulated values lie very close to one another and the there is little variation in the two values regardless of normalization point.*

S_R had an average value of $0.976W/m$ with a standard deviation of $0.029W/m$. This indicates that the power per unit length S_L has an average value of $9.636W/m$ with a deviation of $0.29W/m$. Figure 7.4 shows the model irradiance versus measured irradiance with increasing values of d and $h = 0.92m$, showing the very close agreement. This close agreement is seen at all lengths along the tube in the simple case.

7.1.3 Conclusions for simple case

The high level of agreement between measured and simulated data strongly implies that the model works for the simple case. The simple case of the new model is much more accurate than the radial model at all points. However, the simple case shares one element in common with the radial model in so much as it breaks down when the detector is not directly focused upon the source. This requires the general case solution to be verified.

7.2 Investigating the general case

While it was useful to examine the simple model, a general solution proves a great deal more powerful as it allows calculation of irradiance regardless of orientation and in practice, human skin will not be directly facing the source in the majority of clinical situations. Also, most modern cabins are built with reflectors either behind or around the lamp, and even if the initial radiation from the source came directly upon a relatively flat skin surface, the reflected light would be incident upon the same target at different angles by definition. For these reasons, a general solution is much more applicable in practice and verifying the general solution is paramount to achieving this.

7.2.1 Experimental procedure

To test the general solution at a variety of angles and orientations, the automated detector system discussed in chapter 3.2.3 in conjunction with a single tube rigged independently of the cabin and reflectors. This rotating arrangement provides a varying surface normal $\vec{n}$. The system consists of a pair of detectors,

one collimated and one uncollimated, mounted upon a stepper motor that records 800 measurements over the entire 2π radian rotation, giving a circular irradiance profile. The uncollimated detector has an f_2 of $< 5\%$ and thus a good angular response. To test the merit of the general solution, the automated detector was set up as illustrated in figure 7.5. The length of the pivot to the detector face is denoted L_T, and the pivot lies a distance D along the $\vec{n}$ from the tube centre. The surface normal of this system is parameterized by a circle and the radial vector relates to this, so with respect to the rotation angle ϕ these vectors are given by

$$\vec{n}(\phi) = A(\phi)\vec{x} + C(\phi)\vec{z} = \cos\phi\vec{x} + \sin\phi\vec{z} \tag{7.1}$$

$$\vec{r}(\phi) = d(\phi)\vec{x} + z(\phi)\vec{z} = (D + L_t\cos\phi)\vec{x} + (L_t\sin\phi)\vec{z} \tag{7.2}$$

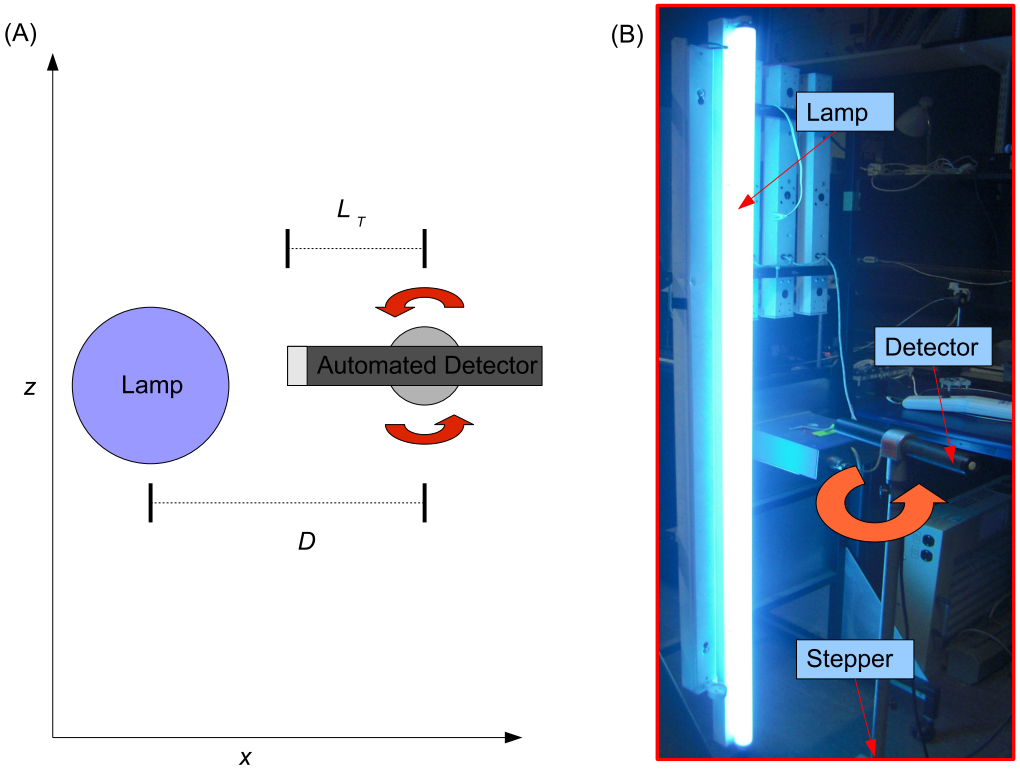

Figure 7.5: *Automated set-up; (A) Top-down view (B) Side view.*

The distance D was varied by moving the automated system back and a series of irradiance profiles were taken at various values of D. Recalling the general solution in equation 6.15, it can be seen as the $\vec{y}$ vector is zero then $B = 0$. Similarly, the magnitude of the normal in this case is a constant of unity so that $|n| = 1$. Thus, this equation can be rewritten in terms of ϕ as

$$E(\phi) = \frac{-S_R}{d(\phi)^2+z(\phi)^2}\left[\frac{(A(\phi)d(\phi)+C(\phi)z(\phi))(L-h)}{\sqrt{d(\phi)^2+z(\phi)^2+(L-h)^2}} + \frac{(A(\phi)d(\phi)+C(\phi)z(\phi))(h)}{\sqrt{d(\phi)^2+z(\phi)^2+h^2}}\right] \tag{7.3}$$

If the general solution holds, this equation should describe the irradiance recorded by the rotating detector. This equation produces negative values of E when the absolute angle between $\vec{n}$ and $\vec{r}$ is greater than $\pi/2$ so care must be taken to ensure that simulated irradiance is forced to zero when a negative value occurs.

7.2.2 General case results

Various values of D up to $570mm$ were examined and pivot length L_T was measured at $150mm$. The pivot began rotation facing directly away from the tube at 0 degrees and was directly facing the source at its closest point at π radians. Because of this, measurements were zero at 0 degrees and a maximum at π degrees. Simulation values were normalized and compared to measured values. These were found to be in good agreement for all cases. Results for the case where $D = 248.5mm$ is shown in figure 7.6. The TL-01 lamp used had an S_R of $0.99438W/m$ with a standard deviation of $0.0084W/m$. Although the lamp used in this experiment was a different TL-01 than in the previous case, the percentage difference in S_R is $< 1.385\%$, strongly suggesting that these model lamps have a consistent output. Agreement between data and model was found regardless of D used, as shown in table 7.2. With increasing values of D, the irradiance fell while the angular extent over which measurements were recorded increased. This is illustrated in figure 7.7 for $D = 368.5mm$ and $D = 478.5mm$, where the scales have been kept the same to illustrate the increasing angular measurement extent and decreasing irradiance with greater values of D.

Table 7.2: Goodness of fit for general model

D of Rotation	r^2 value for measurements at D
$248.5mm$	0.9971
$368.5mm$	0.9943
$478.4mm$	0.9904
$576.5mm$	0.9904

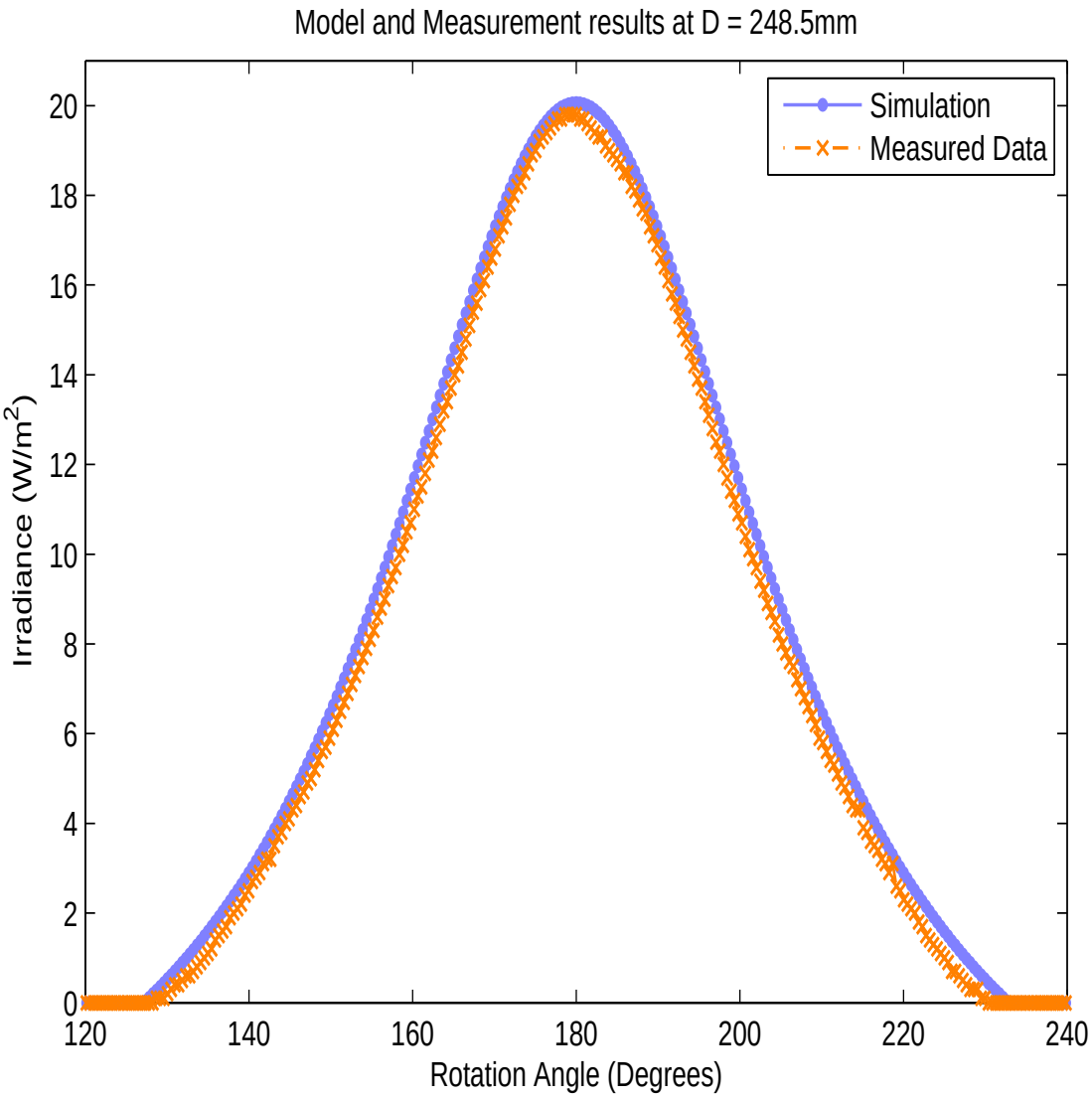

Figure 7.6: *Results of model and measurement at* $D = 248.5mm$

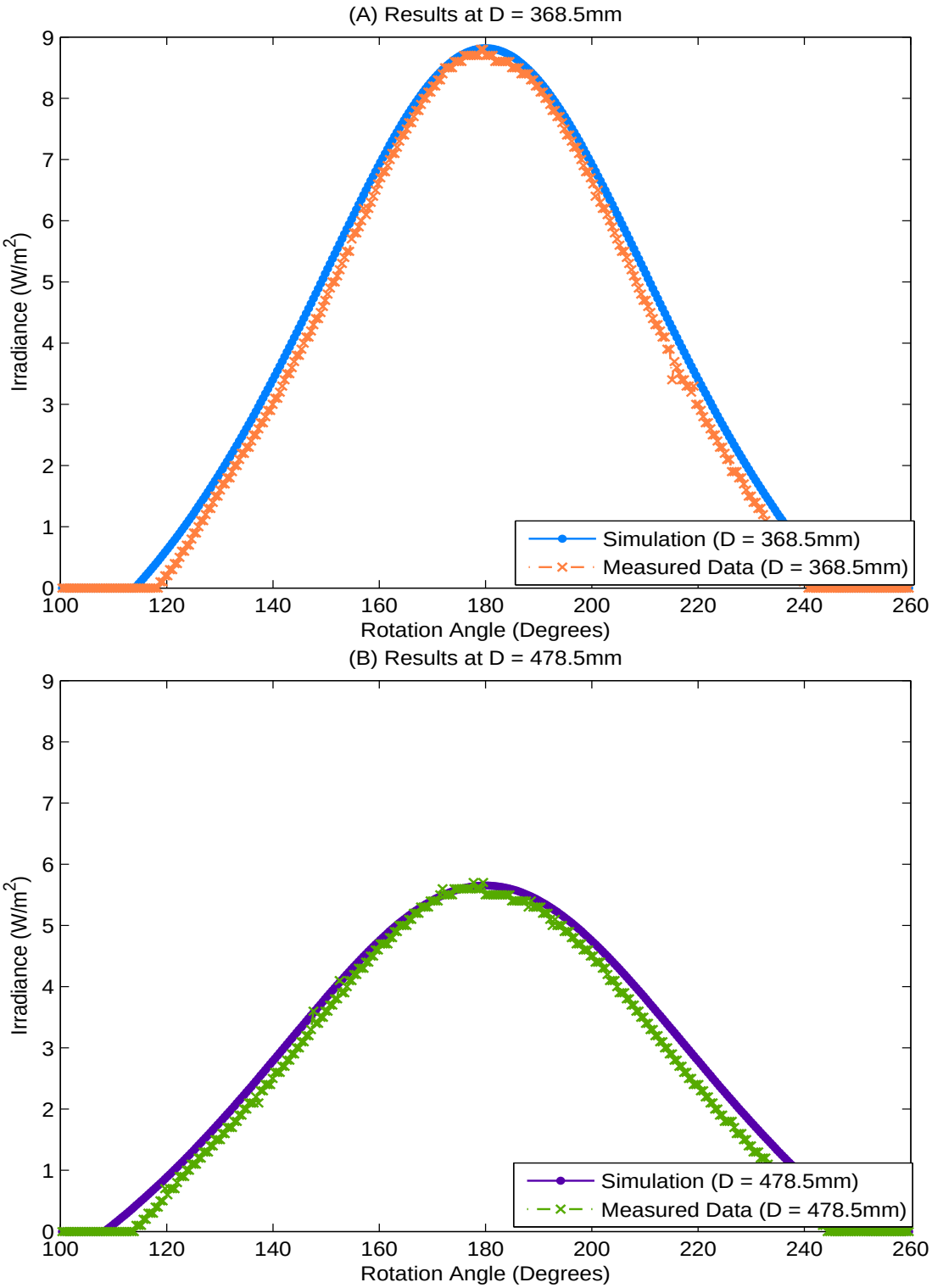

Figure 7.7: *Results at (A) $D = 368.5mm$ and (B) $D = 478.5mm$*

7.2.3 Conclusions for general case

The agreement between model and measured values for constantly varying values of $\vec{n}$ and $\vec{r}$ shows the new model is adapt at describing the physical reality of the lamp source by treating it as a diffuse line source. The value of S_R obtained of $0.99438W/m$ and standard deviation of $0.0084W/m$ yields a value for power per unit length of $9.8141W/m$ with a deviation of $0.083W/m$. The small errors in the fit are likely caused by uncertainties in ascertaining the exact detector to tube centre distance but are exceptionally small and do not impact on the over all fit. There is also a higher contribution from signal noise far out as the readings become much lower and the effects of small jumps become more pronounced.

7.3 Conclusions

The high level of agreement seen with the new model in both the simple and general case indicates strongly that it is capable of fully characterizing the artificial UVR sources for phototherapy. This in itself is a considerable step, as the characterization of artificial UVR sources had been earmarked as a area where research was needed by the NRPB. The model is hence viable as the fundamental component of a UVR dosimetry model and will be used as such in developing a dose model.

Chapter 8

Reflection Modeling

The emission model formulated in chapter 6 and examined in chapter 7 was found to have a very satisfactory predictive power and was suitable for characterizing the output of a UVR lamp. Using this as a basis, it is in theory possible to extend this analysis to deal with reflections from the anodized aluminium back panels and quantify what they contribute to patient dose. There are two distinct possible cases; in one case the images formed are specular and essentially an image of the tube is formed through the reflectors which then contributes to incident dose. The other potential model is a diffuse type model where all radiation from the reflectors can be considered forward directed either through the reflector design characteristics in the UV area of the spectrum or through multiple reflections resulting in a forward scatter. Initial test indicate the former has more predictive power so it is examined here.

8.1 Reflector arrangement

Ultraviolet phototherapy reflectors come in numerous shapes and sizes, and have been broadly outlined in chapter 3.1.2. They are placed as to maximize exposure and minimize light loss. These mirrors can be arranged in any configuration and sometimes consist of just a back mirror, but often these reflectors are typically three flat plane mirrors arranged behind the tube. Such a configuration is shown in figure 8.1. Such an arrangement is typical of a Waldmann cabinet. Other

arrangements include a single flat sheet reflector behind the tubes which is often observed in models from National Biologic.

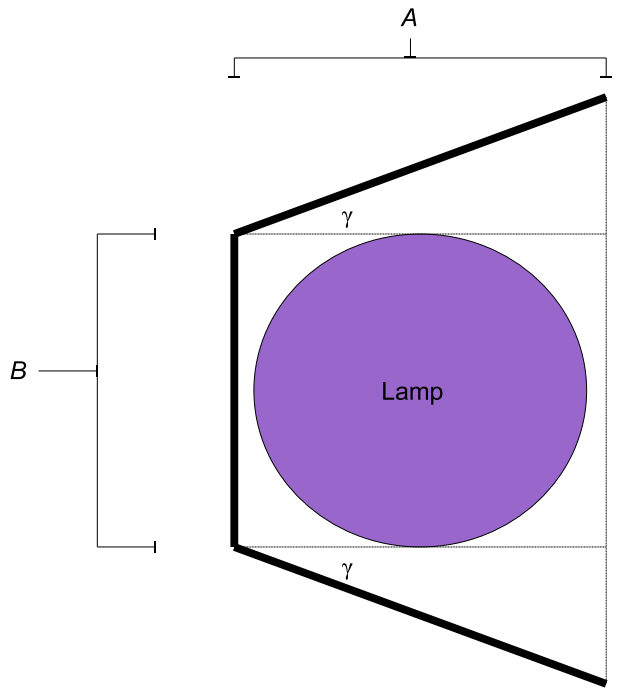

Figure 8.1: *A mirror arrangement with back length B, sides of horizontal length A projected at an angle of* γ

8.2 Specular reflective model

Before embarking on a discussion of the specular model, it is important to slightly modify the general equation to account for cases where $d \neq 0$ and / or $z \neq 0$, where the tube does not stand at the origin, and instead stands at Δd, Δz. Then the radial vector is given by

$$\vec{r} = (\Delta d - d)\vec{x} - l\vec{y} + (\Delta z - z)\vec{z} = d_o\vec{x} - l\vec{y} + z_o\vec{z} \tag{8.1}$$

This modifies the general form in equation 6.15 slightly to

$$E = \frac{S_R}{|n|(d_o^2 + z_o^2)}[\frac{(Ad_o + Cz_o)(L-h) + B(d_o^2 + z_o^2)}{\sqrt{d_o^2 + z_o^2 + (L-h)^2}} + \frac{(Ad_o + cz_o)(h) - B(d_o^2 + z_o^2)}{\sqrt{d_o^2 + z_o^2 + h^2}}] \quad (8.2)$$

The basic principle behind the specular reflection model is that images of the tube are formed in the reflectors and contribute to irradiance through this mechanism. These images will act as emitters, but will be limited by the geometry of the mirror and reduced in intensity by the reflectivity of the mirror, which will be less than unity. If we denote this as R_f, then the equation for a contribution from reflection is then

$$E = \frac{R_f S_R}{|n|(d_o^2 + z_o^2)}[\frac{(Ad_o + Cz_o)(L-h) + B(d_o^2 + z_o^2)}{\sqrt{d_o^2 + z_o^2 + (L-h)^2}} + \frac{(Ad_o + cz_o)(h) - B(d_o^2 + z_o^2)}{\sqrt{d_o^2 + z_o^2 + h^2}}] \quad (8.3)$$

.

For any arbitrary point, there may be contributions from the both the tube and one or more mirrors, or alternatively contribution from either the tube or mirrors or none. It is prudent to establish theoretical bound on where these zones of reflection occur.

8.2.1 Mirrors and source reflection

The specular reflective model assumes the mirrors are approximately planar, so that the angle of incidence equals the angle of reflection, and there is little dispersion of the incident light upon reflection. Similar assumptions have been made for cabin reflectors before (Langmack 1998). The reflections at a point $C(C_x, C_z)$ from a mirror arrangement similar to that is 8.1 are shown in 8.2. Geometrical effects are initially assumed to be small and contributions from the back mirror negligible.The source at P is effectively surrounded by two plane mirrors which contribute at the irradiance measured at C. For any point C there can be contribution from one mirror, both mirrors or neither mirror and it becomes important to generalize a method to allow quick computation of mirror contributions for any such point.

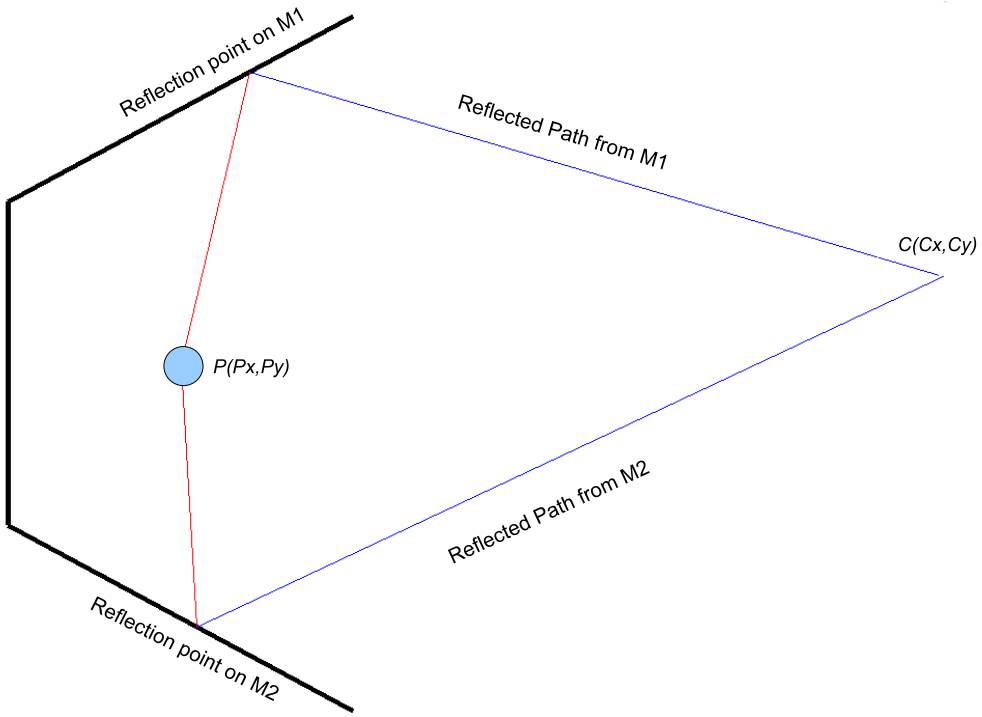

Figure 8.2: *The path of reflected light from the CR source centred on* (P_x, P_z) *to a measurement point* (C_x, C_z)*. M1 denotes the upper mirror and M2 the lower one.*

8.2.2 Finding the image of P through the mirror

The mirror can be defined with two sets of points at either extent; these points are denoted $L(L_x, L_z)$ and $U(U_x, U_z)$ respectively. With this, it is possible to treat the mirror as a line, with a slope M_L readily calculated from the coordinates U and L. For P, the co-ordinates are given by $\Delta d, \Delta z$. It can be shown through manipulation of the algebra that the coordinates for the image of P, denoted P', are given by

$$P'_x = \Delta d + (2M_L(\Delta z + M_L L_x - \Delta d M_L - L_z)/(M_L^2 + 1)) \tag{8.4}$$

$$P'_z = \Delta z + (2(L_z - M_L L_x + \Delta d M_L - \Delta z)/(M_L^2 + 1)) \tag{8.5}$$

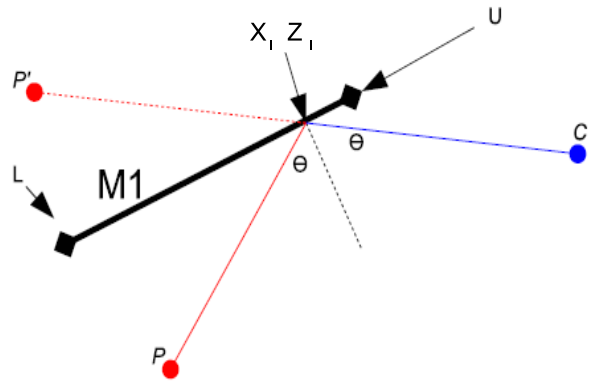

Figure 8.3: *Light incident from P hits a point on $M1$ creating an angle of θ with the normal. This is reflected at the same angle to C. P' is the image of P through $M1$. X_I and Z_I give the points of intersection.*

8.2.3 Determining regions of contribution and non-contribution

The analysis above can be extended to cover multiple reflectors around a tube quite readily. This leads into the next foreseeable problem; determining zones where reflection contributions count and zones where they do not. There are three specific regions of interest, depicted in figure 8.4. The first fundamental region of interest is the contribution from the source itself shown in figure 8.4(A); Emissions come from the centre of the tube source, and limited only by the reflector edges. The line from the upper edge of $M1$ to the centre of the tube source is $S1$, and the line from the upper edge of $M2$ to the tube centre is $S2$ so any point lying between these lines will have a direct contribution from the source.

Figure 8.4(b) illustrates the zones where reflections from the mirror $M1$ contribute. The line from the image of the tube centre in the reflector to the upper edge of $M1$ is denoted $Q2$. Assuming that any photons reflected back onto the tube itself from $M1$ are not re-emitted and secondary reflection from the tube is minimal, this means $Q1$ is the other bounding line for the contributions from $M1$ reflections and it is given as the line between the image through $M1$ and the tangent to the source circular cross-section. The zone bounded by these lines has a reflection contribution from $M1$.

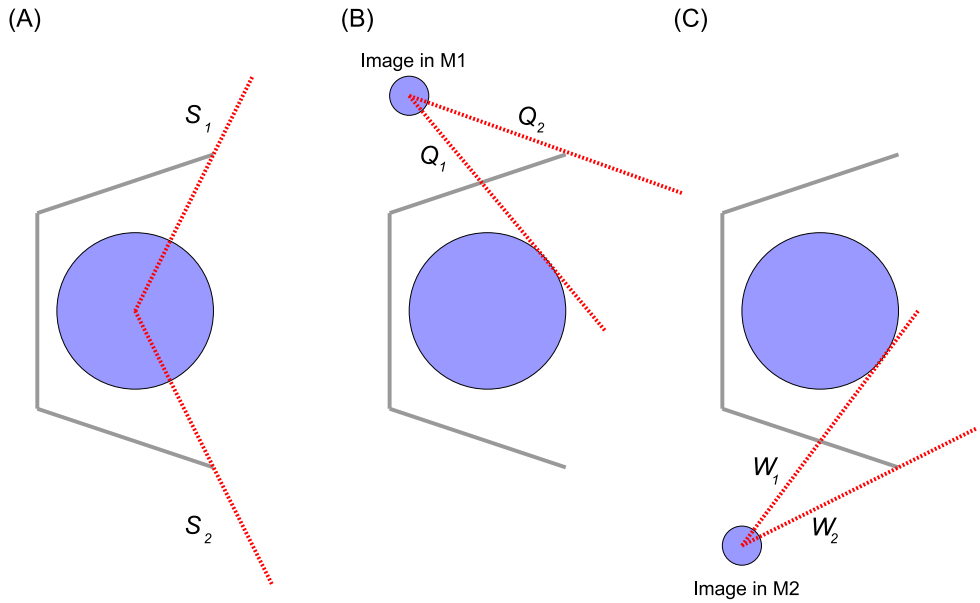

Figure 8.4: *Three possible regions of contribution (A) From the source between the lines S_1 and S_2 (B) From the source image in $M1$ between the lines Q_1 and Q_2 (C) From the source image in $M2$ between the lines W_1 and W_2*

Figure 8.4(c) depicts the analogous case for reflections from $M2$, bounded by the lines $W1$ and $W2$. Ergo, the region between these lines will have a reflection contribution from $M2$. These cases and the respective equations for determining them will be derived here.

8.2.3.1 Regions with direct contribution

To determine if any point x, z lies in a zone of direct contribution is relatively straight-forward. The slope of $S1$ is readily determined from the co-ordinates of the tube centre and edge of $M1$. Denoting this slope m_{S1}, the line equation can be re-arranged so that for any given input d, it produces a relative z_{S1} position on $S1$. Using the same logic on line $S2$ and denoting its slope m_{S2} yields the equations

$$z_{S1} = m_{S1}(x - \Delta d) + \Delta z \tag{8.6}$$

$$z_{S2} = m_{S2}(x - \Delta d) + \Delta z \tag{8.7}$$

If a chosen value of x has a corresponding z with a value between z_{S1} and z_{S2}, it has a direct contribution from the source.

8.2.3.2 Regions with reflection from $M1$

Determining the equation for $Q2$ is straight-forward, but the line equation for $Q1$ requires a slightly more esoteric approach. If the tube has a circular cross section with a radius R, it is technically possible to derive an algorithm to determine the two tangent points from the image. The tangent line nearest the upper point on the mirror is the bounding line $Q1$. Finding the equation of this line can be accomplished using a similar method to that used in chapter 6.3.1 on circular obstruction; the bisector angle can be calculated from equation 5.3. The angle between the tube centre and the reflected tube in $M1$ at P'_{M1x}, P'_{M1z}, γ, is then given by equation 5.4. The slope of the tangent lines is then given by

$$m_t = \tan(\gamma \pm \beta) \tag{8.8}$$

This produces two distinct values for m_t; the line nearest the upper point is the bounding line $Q1$ so it is important to determine which line is closer to the point and reject the other one. This is done by utilizing the formula for distance of a line to a point, which is straight-forward to implement into a simulation. Noting that $m_t = m_{Q1}$ and denoting the slope of $Q2$ as m_{Q2} yields the test equations

$$z_{Q1} = m_{Q1}(x - P'_{M1x}) + P'_{M1z} \tag{8.9}$$

$$z_{Q2} = m_{Q2}(x - P'_{M1x}) + P'_{M1z} \tag{8.10}$$

If a chosen value of x has a corresponding z with a value between z_{Q1} and z_{Q2}, it has a reflection contribution from the mirror $M1$.

8.2.3.3 Regions with reflection from $M2$

Determining the zones of reflection from $M2$ can be achieved in a way analogous to $M1$. The relevant bounding line equations yield

$$z_{W1} = m_{W1}(x - P'_{M2x}) + P'_{M2z} \tag{8.11}$$

$$z_{W2} = m_{W2}(x - P'_{M2x}) + P'_{M2z} \tag{8.12}$$

If a chosen value of x has a corresponding z with a value between z_{W1} and z_{W2}, it has a reflection contribution from the mirror $M2$.

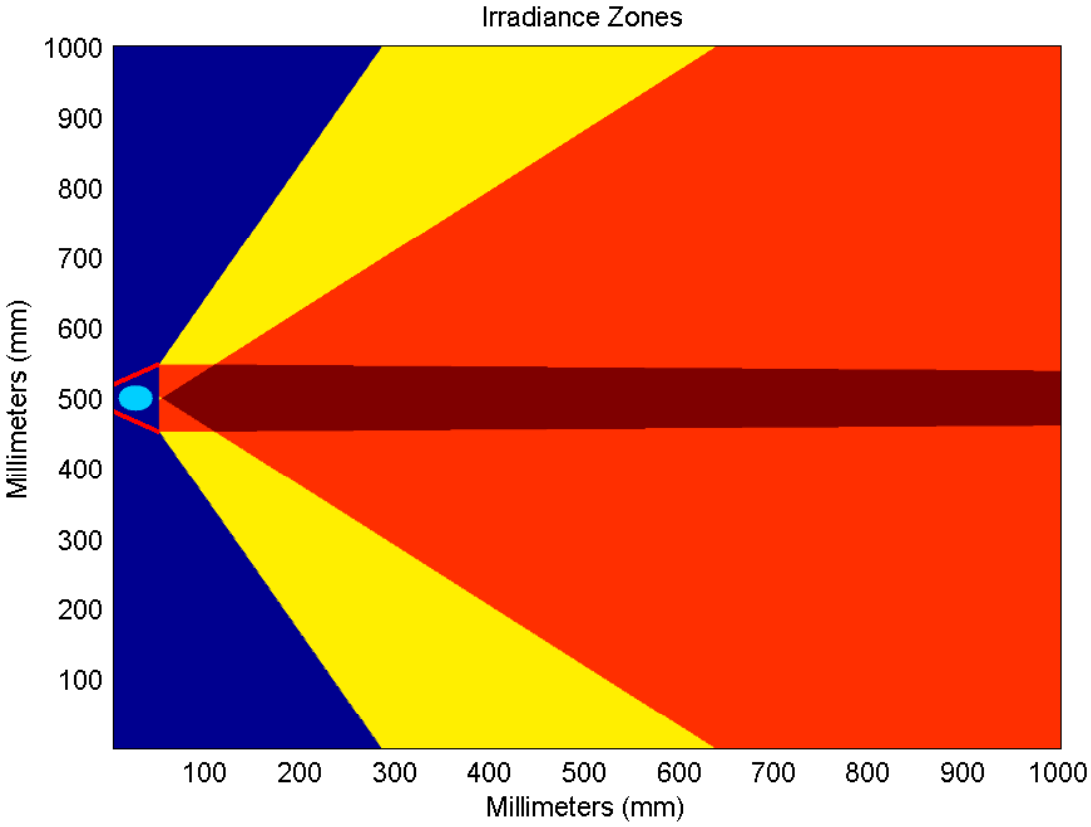

Figure 8.5: *Hypothetical bounding regions for a given mirror arrangement. Areas in blue are not irradiated, areas in yellow are irradiated by the source only, areas in red are illuminated by the source and one of the reflectors and the centre area in brown is illuminated by the source and both reflectors.*

8.2.4 Secondary reflections

The specular reflection model assumes negligible contributions due to the back mirror and secondary reflections off the tube. This assumption that contributions from the back mirror are negligible rests on the fact that the diameter of the tube effectively blocks any reflections from this surface. Reflections off the tube are also discounted; as the UV photons emitted from the tube are created in a fluorescent process, if they are reflected and incident upon the tube, they will effectively be unable to excite the phosphor into emitting further photons. There are, however, small secondary reflection artifacts that can occur. How this occurs is shown in figure 8.6 below. It should be noted that the secondary images formed are not full images as they are limited by the geometry of the mirrors.

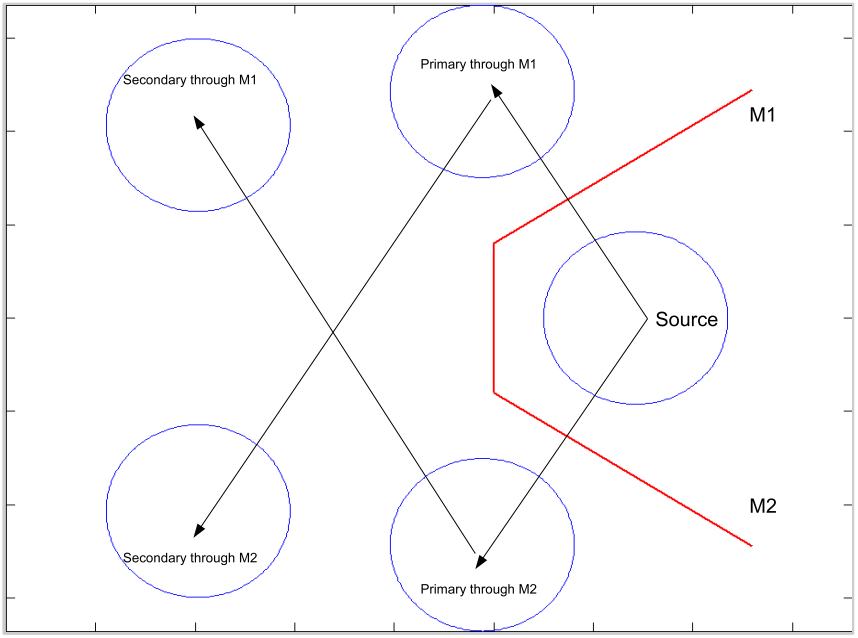

Figure 8.6: *Primary and secondary reflections through a reflector system. The source makes an image through $M1$ which is partially copied in $M2$ and vice versa*

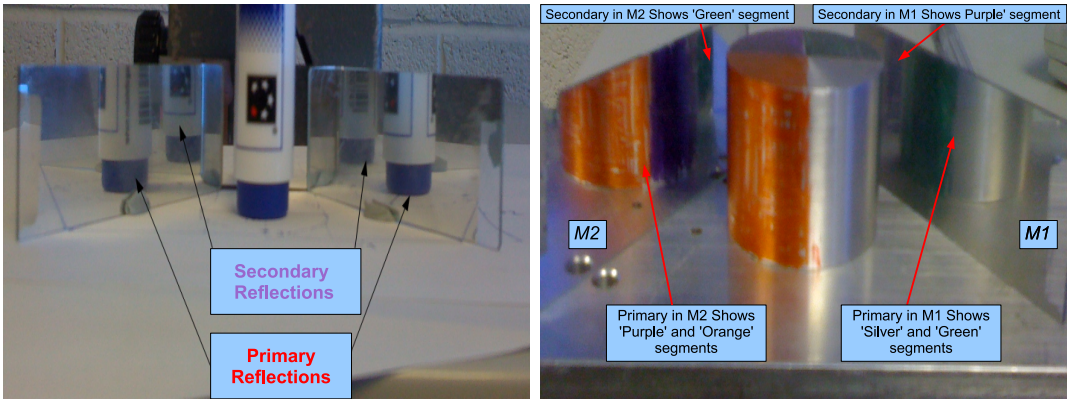

Figure 8.7: *(a) Primary and secondary images formed by an object of small cross sectional area (b) Primary and Secondary images formed by an object with same cross sectional area as UV tube. Object is divided into four equal segments of green, purple, silver and orange for clarity.*

These secondary reflections introduce self shielding issues. Figure 8.7 (a) shows a mock-up of a typical reflector geometry with a object of limited extent. In this case the secondary reflections are quite clearly seen and labeled. Figure 8.7 (b) shows the same set-up with a object with the same cross-sectional area as the tube. In this instance, secondary reflections are largely shielded by tube area itself, implying that it may be able to effectively discount them in practice. Experimentation reveals that the presence of the back mirror does not influence the primary or secondary images.

8.2.5 Specular reflection modeling

Through the analysis outlined thus far, it is possible to estimate the contribution from reflection. The irradiance from a tube standing at any point is given by equation 8.2. Figure 8.8 illustrates the contribution from reflections expected when $R_f = 0.3$ for a hypothetical mirror arrangement, shown by the red lines in this figure with a detector surface normal $\vec{n} = -\vec{x}$ The irradiance in the central line iS increased the most by the contributions from the two mirrors. If we consider the central line as line from the centre of the tube equidistant to both mirrors, it is possible to compare the pure source irradiance to the irradiance from source and mirrors as the detector moves back along this track.

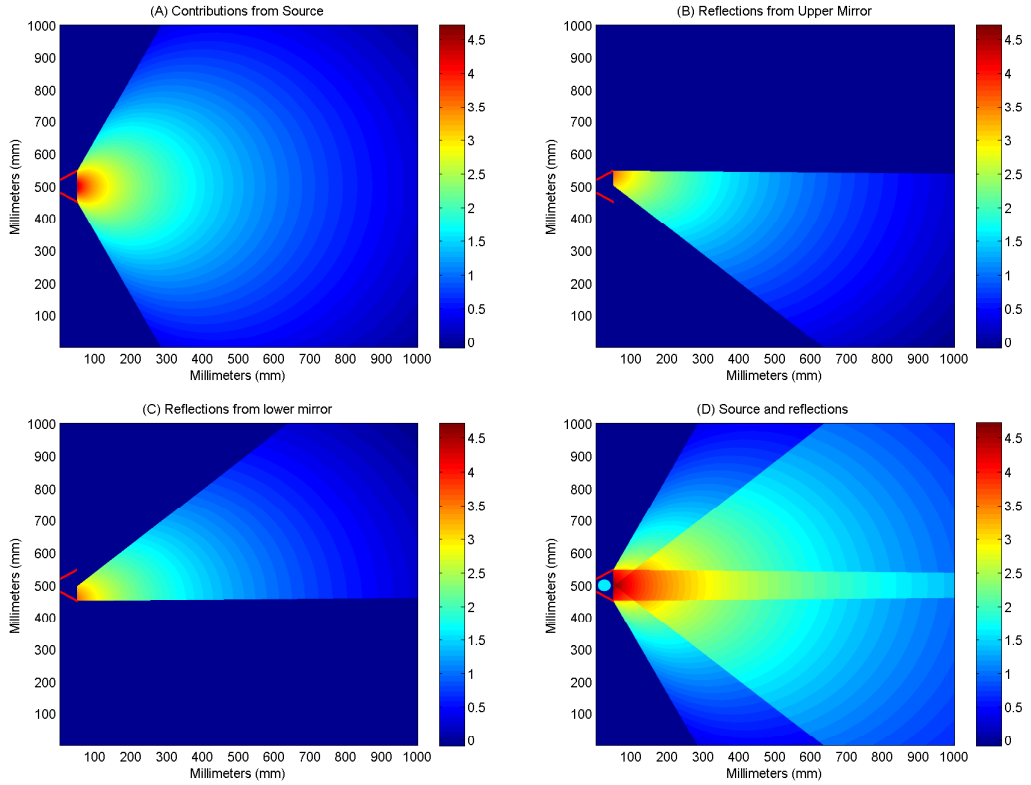

Figure 8.8: *Logarithmic plots of source and reflection contributions for a detector with surface normal* $\vec{n} = -\vec{x}$ *(a) Irradiance from Source (b) Irradiance from Upper mirror* $M1$ *(c) Irradiance from Lower Mirror* $M2$ *(d) Total irradiance from source and reflectors.* $R_f = 0.3$ *in this simulation. Tube is illustrated in (d) with reduced intensity for clarity*

The situation for a rotating detector, similar to the experiment undertaken to verify the general case in the prior chapter, can also be modeled. This is shown in figure 8.9 with for $d = 0.3m$, $z = 0m$ and $R_f = 0.8$. The case of no mirror attenuation and violent attenuation are illustrated in this figure. The harsh cut-off occurs when the detector can no longer 'view' the image source, based on the line source assumption that all photons are emitted from the centre of the line source. This is of course an approximation; an observer can still detect UV photons from a tube even if there is no direct line to the centre. It is likely the drop off will be more gradual than is currently predicted due to the fact the tube is in reality an extended source. This is discussed now.

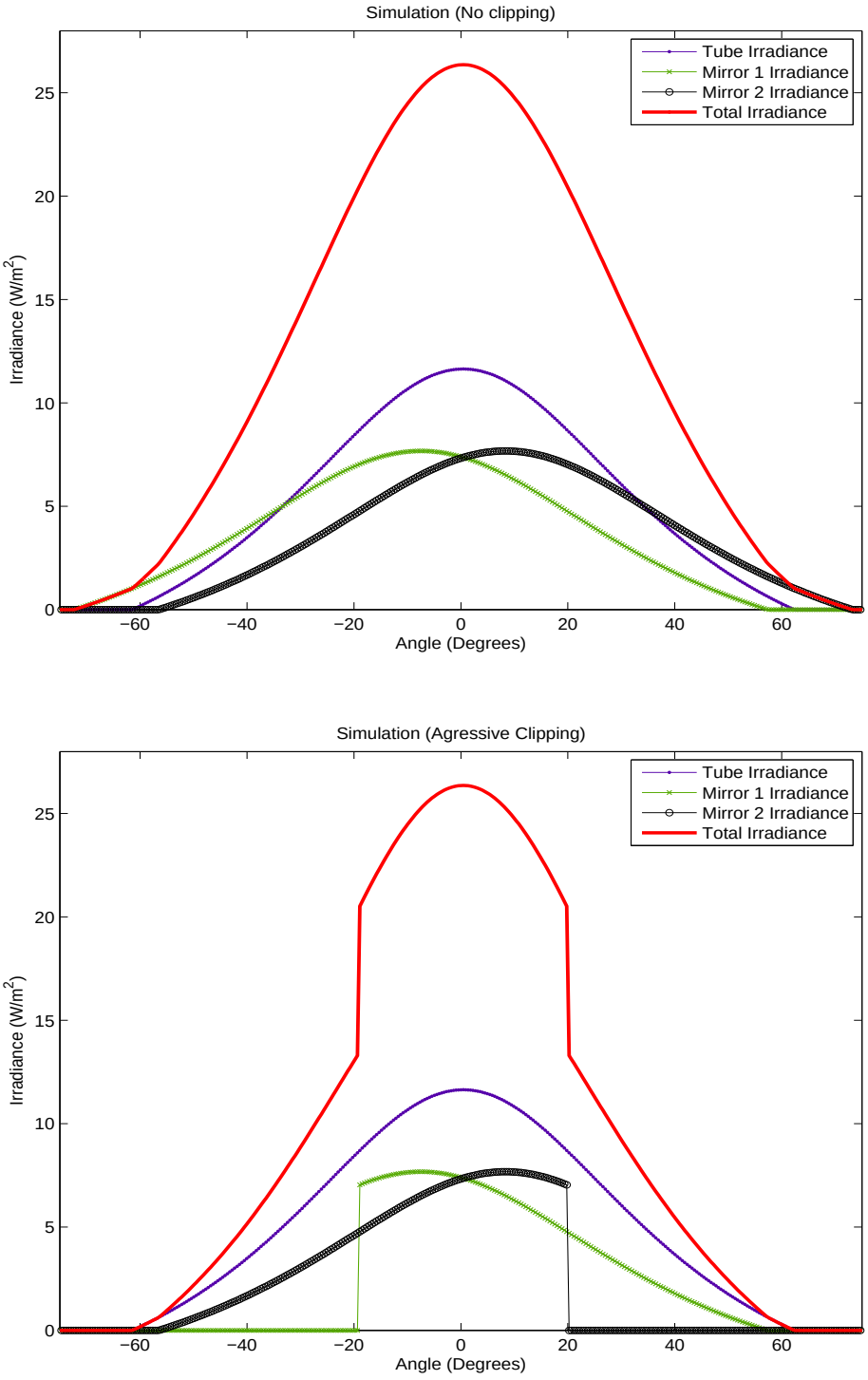

Figure 8.9: *Irradiance from the specular model with mirror arrangement at* $d = 0.3$ *and* $R_f = 0.8$ *and* $S_R = 1$. *Simulations with no mirror clipping and aggressive mirror clipping are shown.*

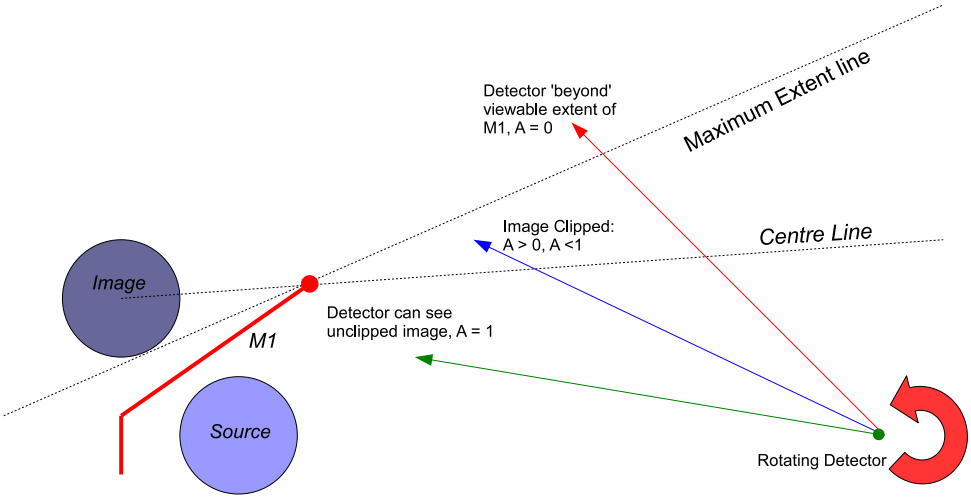

Figure 8.10: *A rotating detector going through distinct attenuation zones with M1; in the first, no reflected irradiance is recorded so $A = 0$. In the second, some is expected so $A > 0, A < 1$ in the third, there is no side mirror clipping so $A = 1$.*

8.3 Image clipping and mirror attenuation

The drastic clipping seen in figure 8.9 is a consequence of modeling the tube as a line source. A line source has no physical extent, but in reality a source does have a limited extent and will still emit even if the centre is not directly viewable. For this reason, one expects a more gradual fall off than that shown in figure 8.9 between these two extremes. A gradual attenuation function at these extents would improve accuracy. One method of doing this is to assume an attenuation function A at certain extents. Consider the situation outlined in figure 8.10. The centre line is the line from the centre of the image through the upper point of the mirror. The maximum extent line is the line through the upper point the mirror tangent to the circle closest to the mirror lower point. 'Below' the centre line, the detector readings are not attenuated and $A = 1$. 'Above' the maximum extent line, the detector cannot see anything from the image and $A = 0$. Between these two regions $0 < A < 1$. There are many options and methods for gauging this attenuation factor, of varying experimental merit but one method has promise and is examined here.

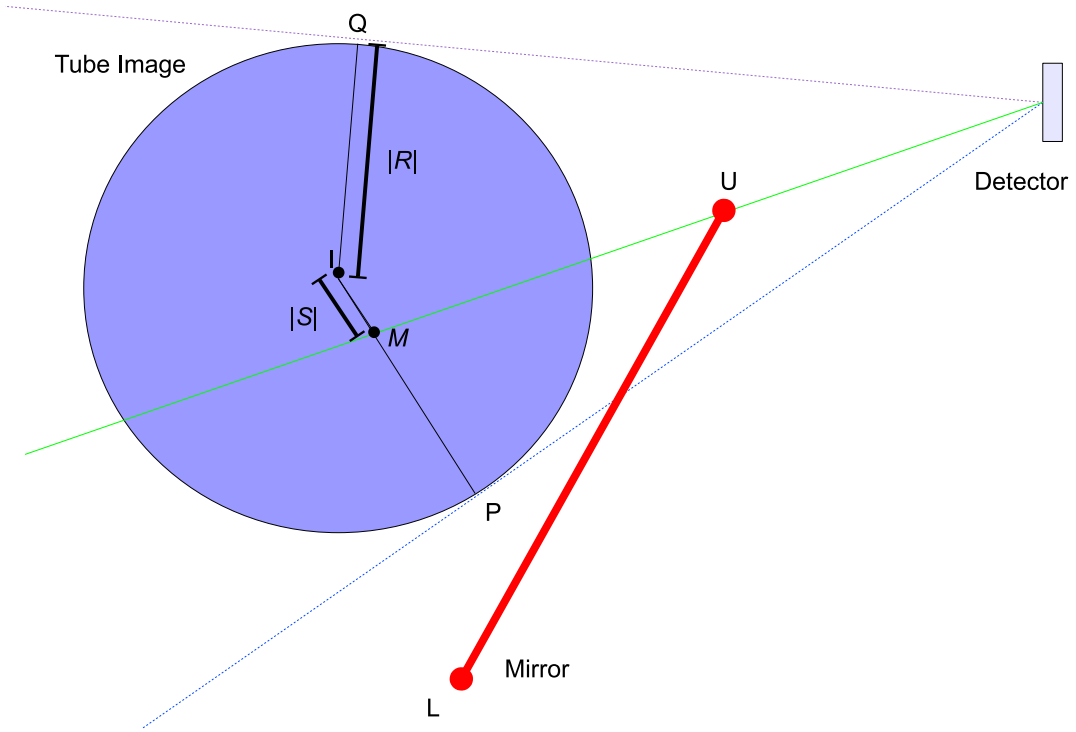

Figure 8.11: *Geometrical arrangement in attenuation zone*

A function that attenuates gradually for points between the central line and the maximum extent line should result in a more realistic model and tighter fit to any measured data. Consider the situation depicted for a detector in a position above the central line so that it undergoes an attenuation of less than unity and greater than zero. Such a scenario is depicted in figure 8.11. A detector at D has tangents to the tube image at P and Q. The line which goes through the upper mirror point U intercepts the line from P to the image centre I at point M. The length of this segment is $|S|$. The radius of the image is $|R|$. A full treatment of how to find these points is given in appendix C. When the detector is between the maximum extent line and the central line, it sees only a fraction of the line $|IP|$. This fraction is given by

$$A_L = \frac{R - S}{R} = 1 - S/R \tag{8.13}$$

With this linear attenuation function, full irradiance is expected up to the central line. After the central line is crossed, the irradiance is attenuated by the factor A in equation 8.13. When $S \geq R$ this is above the maximum extent line and $A = 0$. The attenuation factor is somewhat ad hoc and is introduced to compensate for the fact that the line source model does not have a surface correction. In reality, the tubes are three dimensional objects and as such some clipping is expected. Applying this attenuation correction to the situation in 8.11 results in the more gradual fall off depicted in 8.12

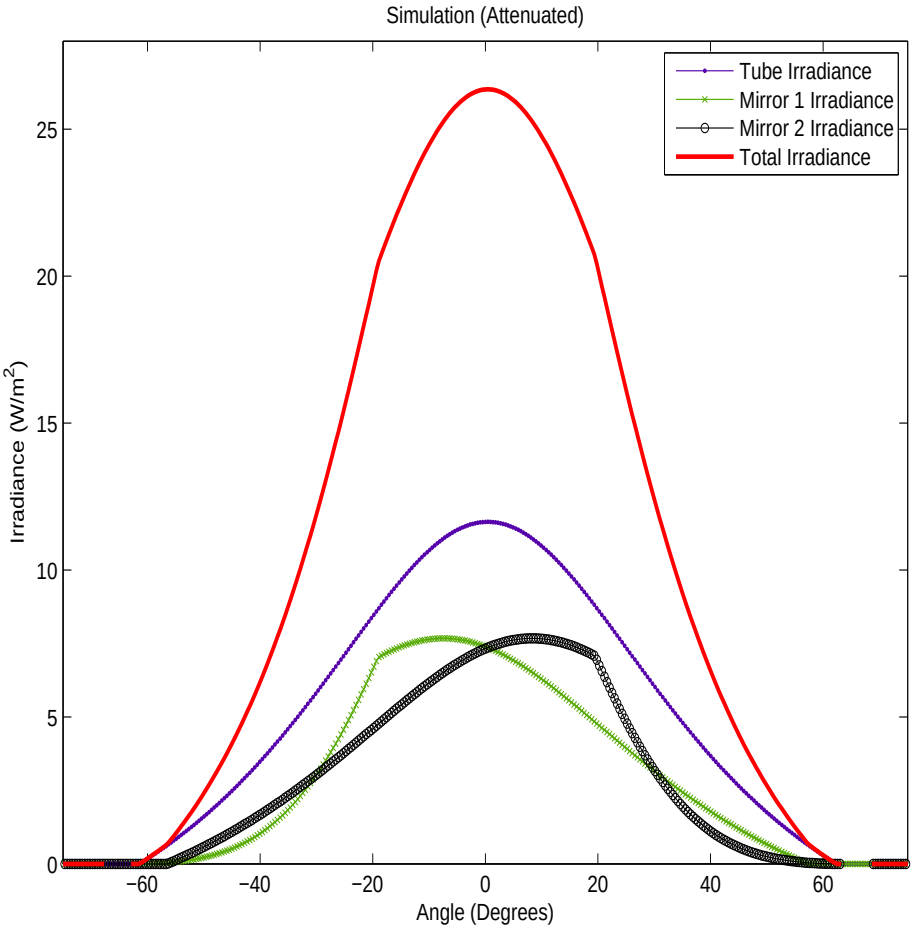

Figure 8.12: *The effect of the derived linear attenuation function on simulation.* $S_R = 1$, $D = 0.3$ *and* $R_F = 0.8$

Another potential attenuation function that results in a smoother cut off is the square of A_L which can be defined as the square attenuation function or

$$A_s = A_L^2 = (1 - S/R)^2 \tag{8.14}$$

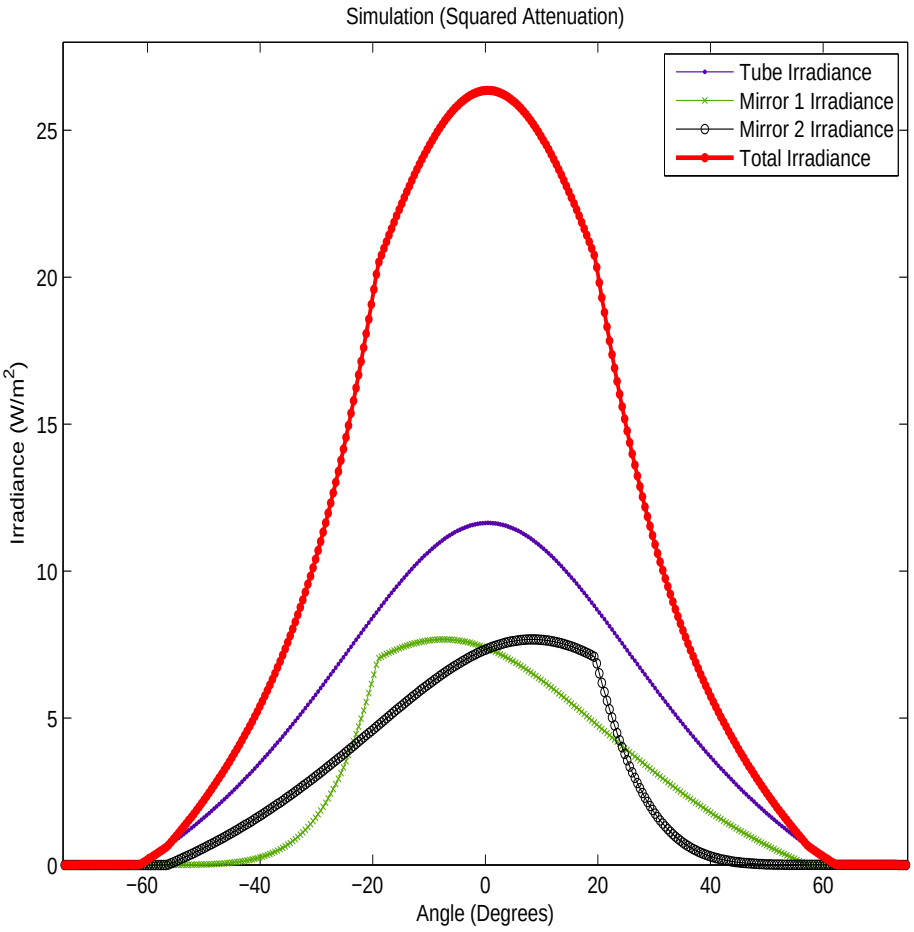

Figure 8.13: *The effect of the derived square attenuation function on simulation.* $S_R = 1$, $D = 0.3$ *and* $R_F = 0.8$

The effect of this squared attenuation function on the simulated irradiance is depicted in figure 8.13. The differences are subtle in that both functions attempt to correct for the expected clipping by relating the attenuation to the extent of tube surface visible at these points. The real physical relationship may be more complex but these functions may provide a good start to modeling the real tube behaviour.

8.4 Conclusion

Experimental investigation of the line source model proved that it works exceptionally well for UVR tube sources, and this section is an outline of how the same principle may be extended to cover specular reflection. To this end, a theoretical model that produces an image of the tube in a surrounding mirror has been developed in this section.

The fact that the tube is in reality an extended source may cause some complication, so to factor in for this possibility an ad hoc attenuation factor has been added to the model. The principle behind this attenuation factor is solely to correct for clipping artifacts that arise when the tube image is partially obstructed by the mirror edges.

The possible contributions from secondary images have been discussed though it is not expected to amount to a great deal with commonly encountered tube / reflector geometries. This can be verified through experimental analysis.

With the model, attenuation functions and possible reflection artifacts theoretically outlined, the next step is to experimentally examine the model to ascertain its merit. This is covered in the next chapter.

Chapter 9

Experimental investigation of reflection models

The model and conditions outlined in the previous chapter for reflective surfaces need to be experimentally verified to determine their viability and ascertain their predictive power.

9.1 Mirror geometry

Reflective aluminium sheets for use in phototherapy generally consist of pressed sheet metal. This sheet metal can be left flat and placed behind the tubes, or shaped and pressed into mirror arrangements to further increase the irradiance. To examine this, a Waldmann UV-1000 cabin was reverse engineered and the mirror sheets removed from it. The geometry of the tube / mirror arrangement seen on the non-inclined wall of this cabin is illustrated in figure 9.1 and laid out in table 9.1.

Table 9.1: Relative positions of Mirror points (tube centre on origin)

Mirror point	**Relative position**
U_{X1}, U_{Z1}	23.5 mm, 49 mm
U_{X2}, U_{Z2}	23.5 mm, -49 mm
L_{X1}, L_{Z1}	-28.5 mm, 16 mm
L_{X2}, L_{Z2}	-23.5 mm, -16 mm

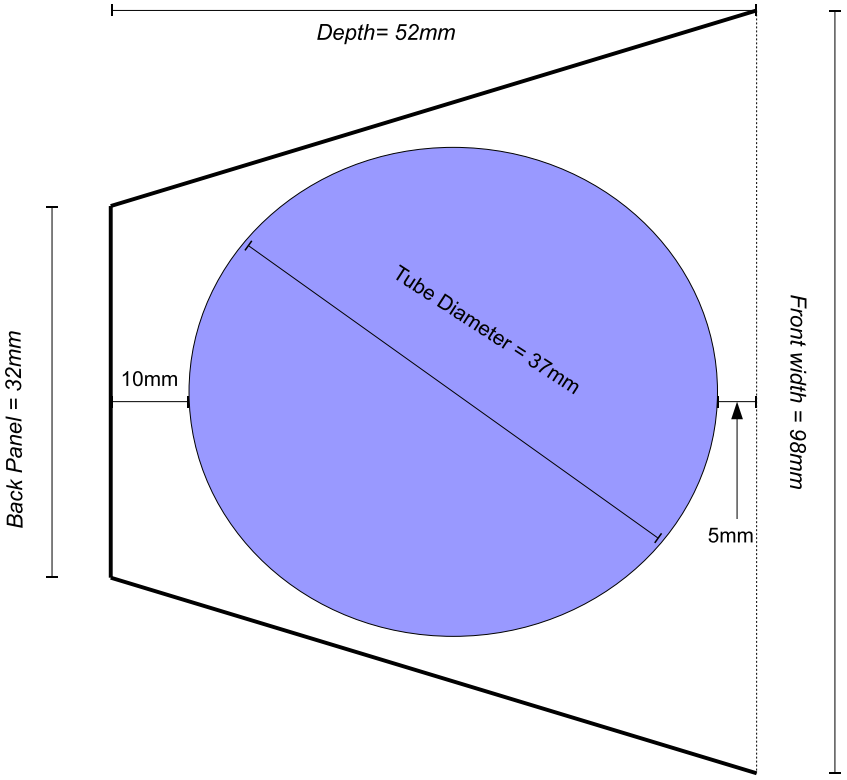

Figure 9.1: *Geometry of Waldmann UV-1000 reflector sheet / tube on flat side*

The sheet metal can be pressed into whatever configuration the manufacturer requires. Interestingly, there are two different arrangements inside the Waldmann UV-1000 cabin; in addition to the dimensions shown in the figure and table, there is also a slightly different configuration with the front width set at $80mm$ rather than $98mm$. For experimental purposes, the $98mm$ set up was replicated outside the cabin to investigate the effect of reflections from this arrangement. A holder was designed to keep the mirror in place around the vertical tube and the back mirror was blacked out with matt black cardboard. The experiment was set up in a similar fashion to rotating detector test outlined in chapter 7. The two side mirrors could be covered by using long thin strips of black matt card and the effects on the measured irradiance observed. A simplified version of the experimental set up is shown in figure 9.2.

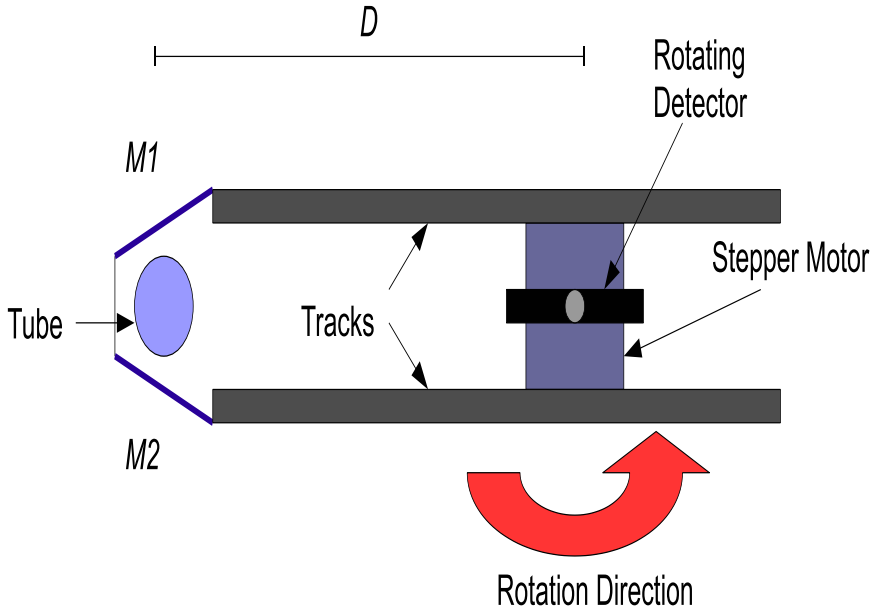

Figure 9.2: *Geometry of the reflection investigation set-up.*

Manipulating the image equations C.5 and C.6 and placing the tube centre at the origin yields images with centres through $M1$ and $M2$ respectively as

$$(P_{X1}, P_{Z1}) = (-0.0308423, 0.04860) \tag{9.1}$$

$$(P_{X2}, P_{Z2}) = (-0.0308423, -0.04860) \tag{9.2}$$

This establishes the position of the image centres through both mirrors, quantifying where one would expect the centre of the image to occur through $M1$ and $M2$ respectively.

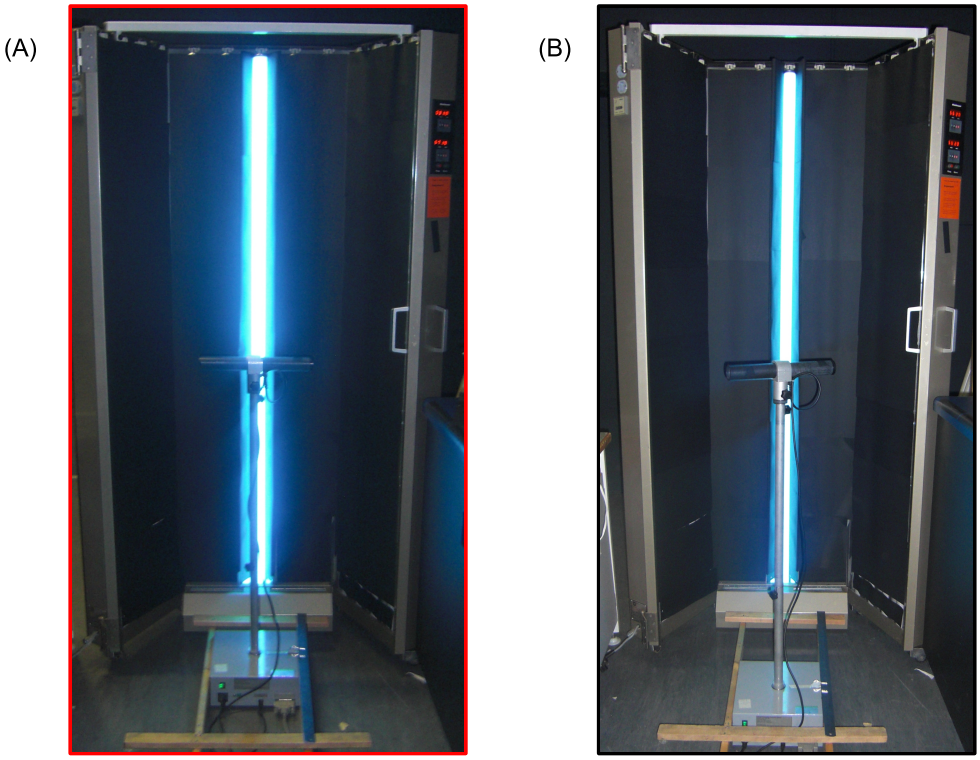

Figure 9.3: *Converted UV-1000 cabin for reflection testing (A) depicts set-up with distance from tube centre* $D = 0.3285m$ *and (B) depicts the case when* $D = 0.5685m$*. Both side mirrors are covered with hard card in this figure.*

9.2 Experimental setup

In this experiment, one half of a UV-1000 cabin was examined. All tubes except a single tube in the centre (*Phillips TL/01 100 W*) were removed and all mirrors apart from those surrounding the single tube were covered up with matt black cardboard. A cradle was constructed to allow the automated detector move along the distance axis from the tube. Distances along the cradle from the tube centre were graduated. The visible extent of the tube was 1.688 m and the detector head was a relative height of 0.845m along the length of the tube. The back mirror behind the single tube was also blacked out with thin strips of matt black cardboard to initially discount any stray reflections from the back mirror. In addition

to the free standing set up, two sheets of hard matt black card were constructed which were wide enough to block out the side mirrors. The experimental set up with these cards in place is shown in figure 9.3. With the experiment set up this way, a series of different investigations could be undertaken.

9.2.1 Reflection data

The cradle allowed the radial distance from the tube centre to be varied while the lateral displacement was kept constant at 0. The value of D was varied and at each value, four sets of measurements were taken with the automated detector. These were

1. A full rotation of measurements with both side mirrors $M1$ and $M2$ covered with the cardboard shields.
2. A full rotation of measurements with $M1$ uncovered and $M2$ covered.
3. A full rotation of measurements with $M2$ uncovered and $M1$ covered.
4. A full rotation with both both $M1$ and $M2$ uncovered.

The logic behind running the first test was to quantify the properties of the tube itself without reflection. The irradiance profile from the mirror-shielded tube with the automated detector was expected to look the same as the irradiance profile of a freestanding tube as outlined in chapter 6. Essentially the tube only irradiance provided a baseline against which reflection contributions could be quantified. The second and third measurement sets quantified the effect of $M1$ and $M2$ respectively and the final set of measurements provided data for the tubes together which would include any potential secondary reflection effects. The reflection contribution from either mirror could then be simply calculated by subtracting the baseline of the data set from a run with the mirror in question. The experiments were run and repeated and the results collected and analyzed.

9.3 Results from reflection data

The value of S_R for the Phillips tube was found to be 0.942 W/m with a standard deviation of 0.017 W/m. This is within 96% of the value for the previous tubes examined and was perhaps slightly lower due to the fact the tube tested in this experiment had seen prior clinical use whereas the tubes used before had never been used in clinical practice. The collimated detector recorded one peak with just the tube, two peaks for a tube and a side mirror and three peaks for the tube and both side mirrors uncovered. Direct and reflected contributions for $D = 0.3285m$, $D = 0.4685m$ and $D = 0.5685m$ are shown in figures 9.4 and figure 9.5.

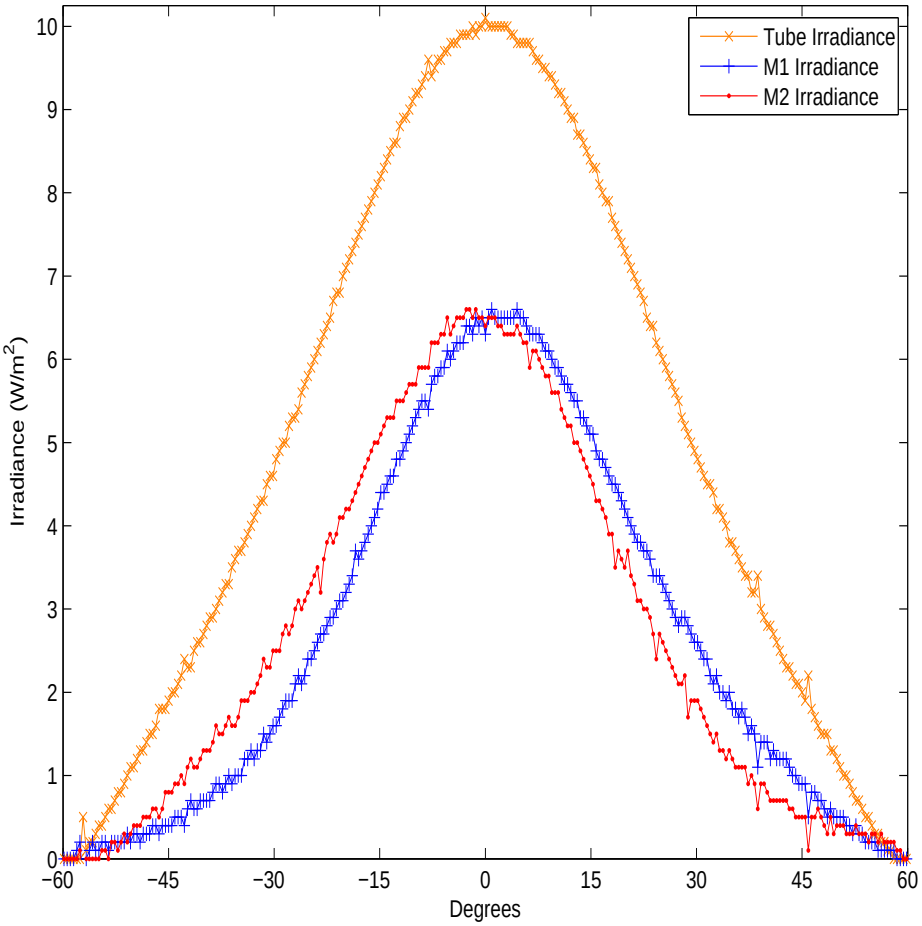

Figure 9.4: *Relative contributions of Irradiance at* $D = 328.5mm$

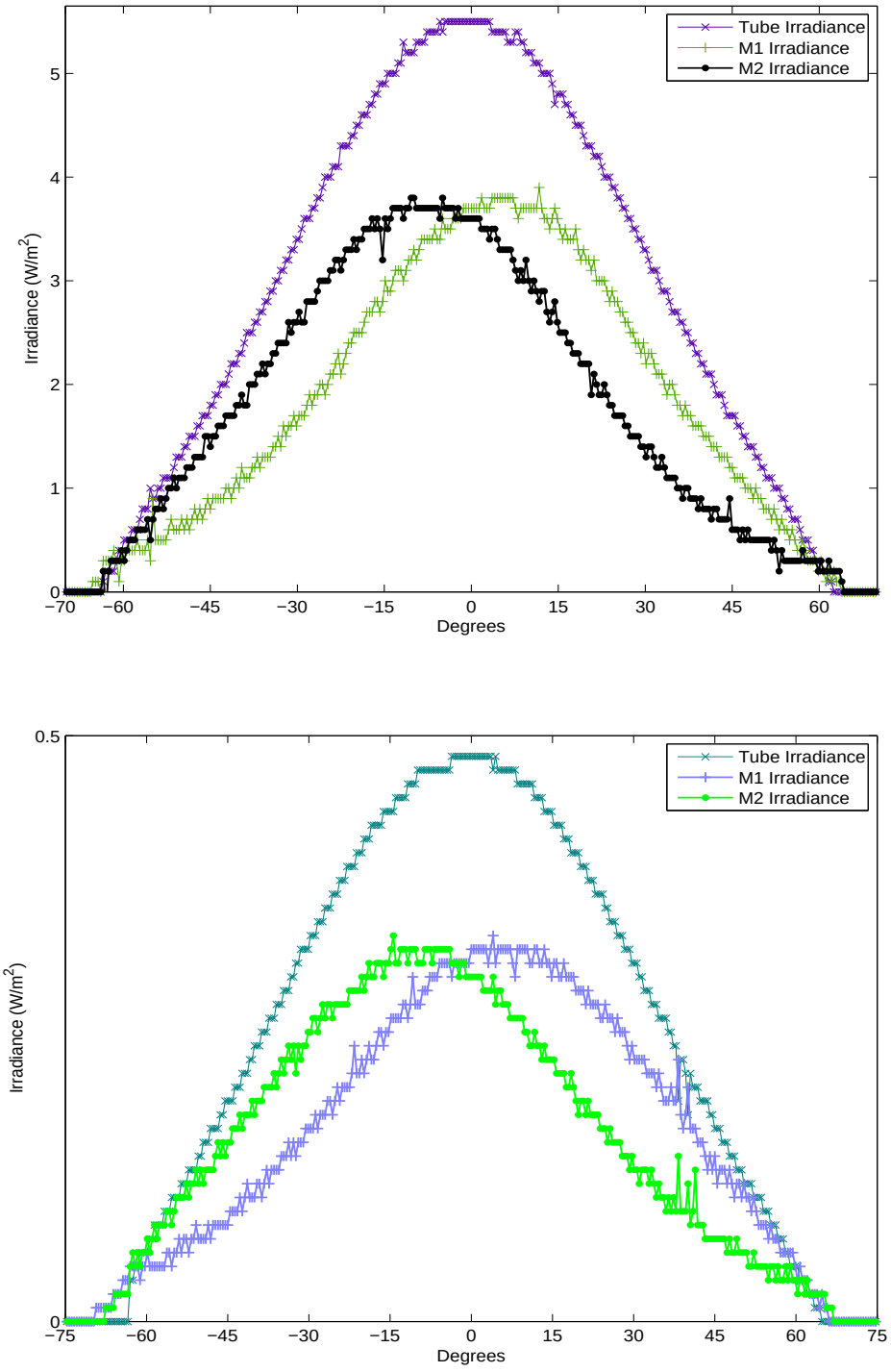

Figure 9.5: *Relative contributions of Irradiance at (A)* $D = 468.5mm$ *and (B)* $D = 568.5mm$

Comparing the data sets, it is clear that there is a reflected image for each side mirror as is clearly seen in the results graphs. The reflected data appears to get close to its peak and then gradually drop off towards the edges. A rough value for the reflectivity of the mirrors can be calculated if one assumes that the maximum value for reflected data is roughly inline with the model peak for the reflected data. This gives a value for the reflectivity R_f of 0.776 with a standard deviation of 0.014. This in reality may be a slight underestimation due to the fact that the mirror may cause clipping just prior to the respective peaks but the minimal variation suggests that it is consistent and close to this maximum value. The total irradiance for any surface normal is the clinical quantity of most interest and this can be found from the measured data. This can be compared and contrasted with the reflection model with mirror attenuation derived in the previous chapter. The results of this analysis are shown in figures 9.6 and 9.7.

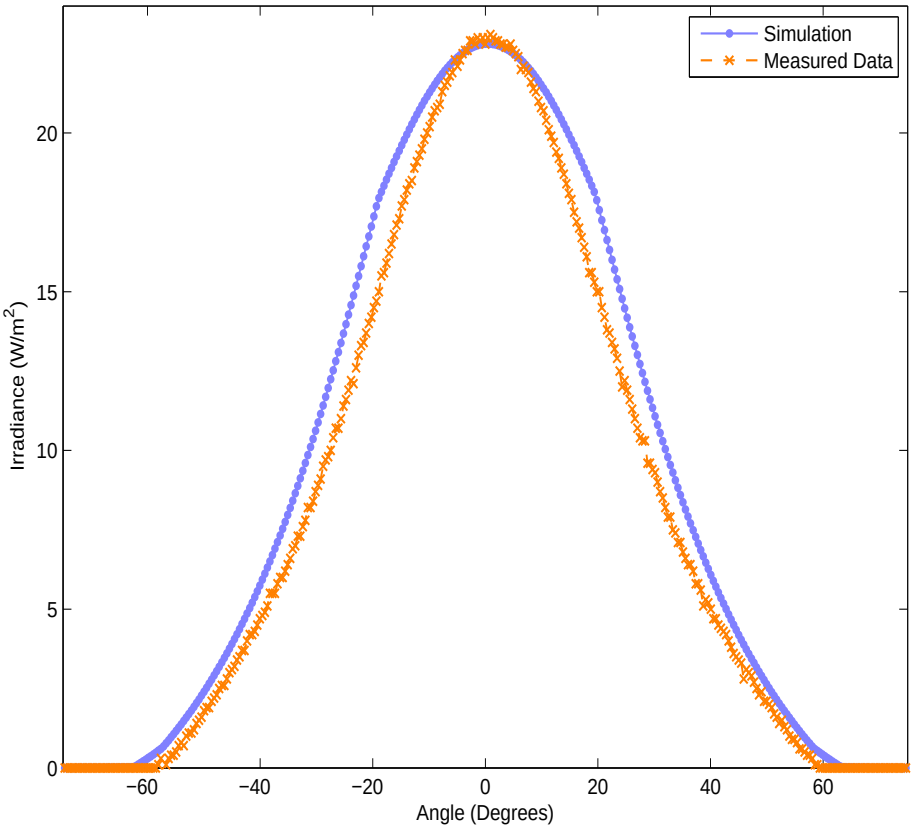

Figure 9.6: *Full rotation with $D = 328.5mm$ and linear attenuation*

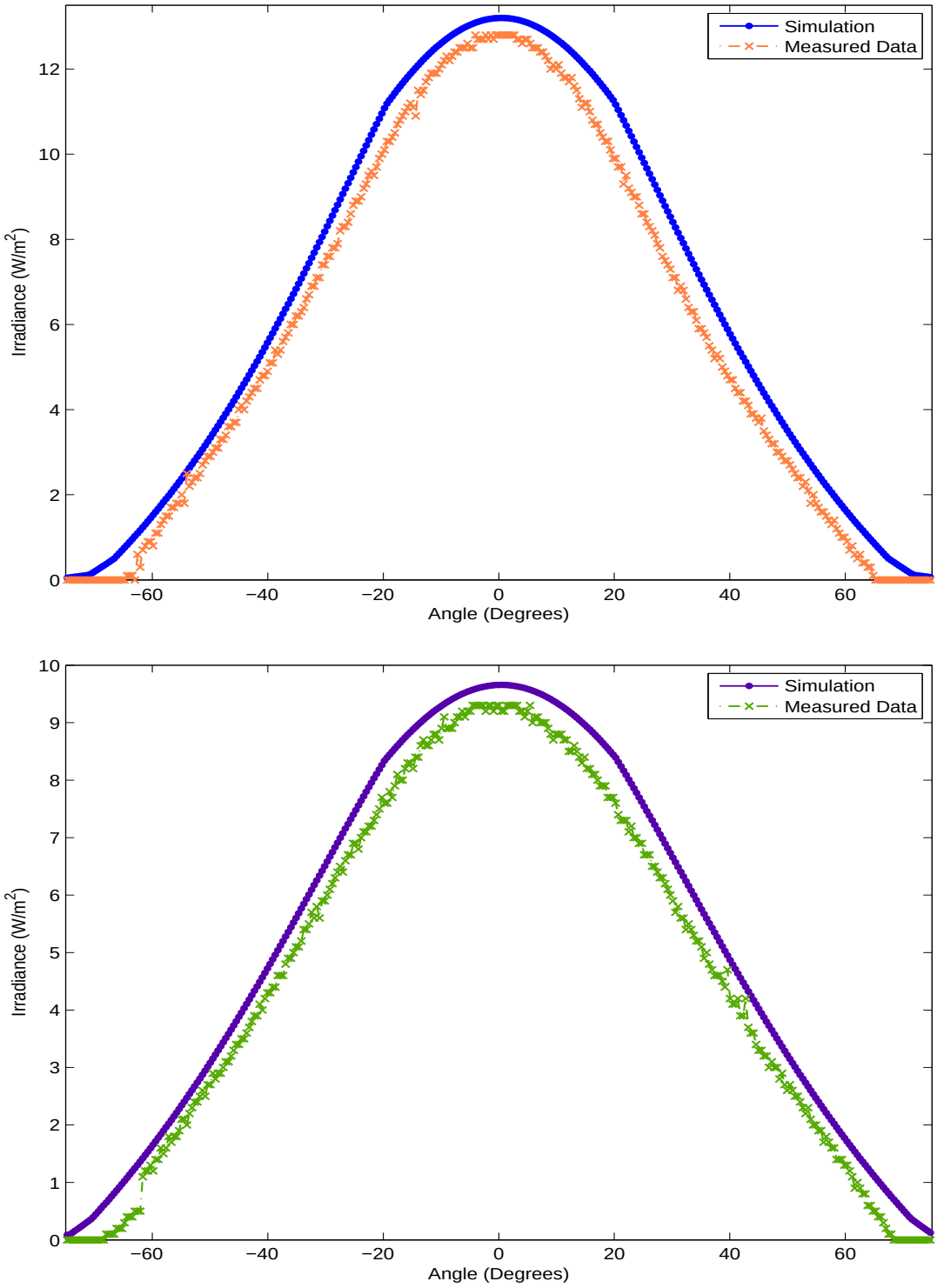

Figure 9.7: *Full rotations (A) $D = 468.5mm$ and (B) $D = 568.5mm$ with linear attenuation*

Table 9.2: Goodness of fit for linear attenuated reflective model

D of Rotation	r^2 value for measurements at D
$326.5mm$	0.9828
$468.5mm$	0.9854
$568.5mm$	0.9865

The co-efficient of determination for these rotations with linear attenuation are given in table 9.2. In general the fits are satisfactory, however the model slightly overestimates the irradiance in each case. This is likely due to the ah hoc attenuation factor not falling off fast enough but is still close enough that it gives remarkably good results. The same analysis can be performed for the squared attenuation function and this is show in figures 9.8 - 9.9.

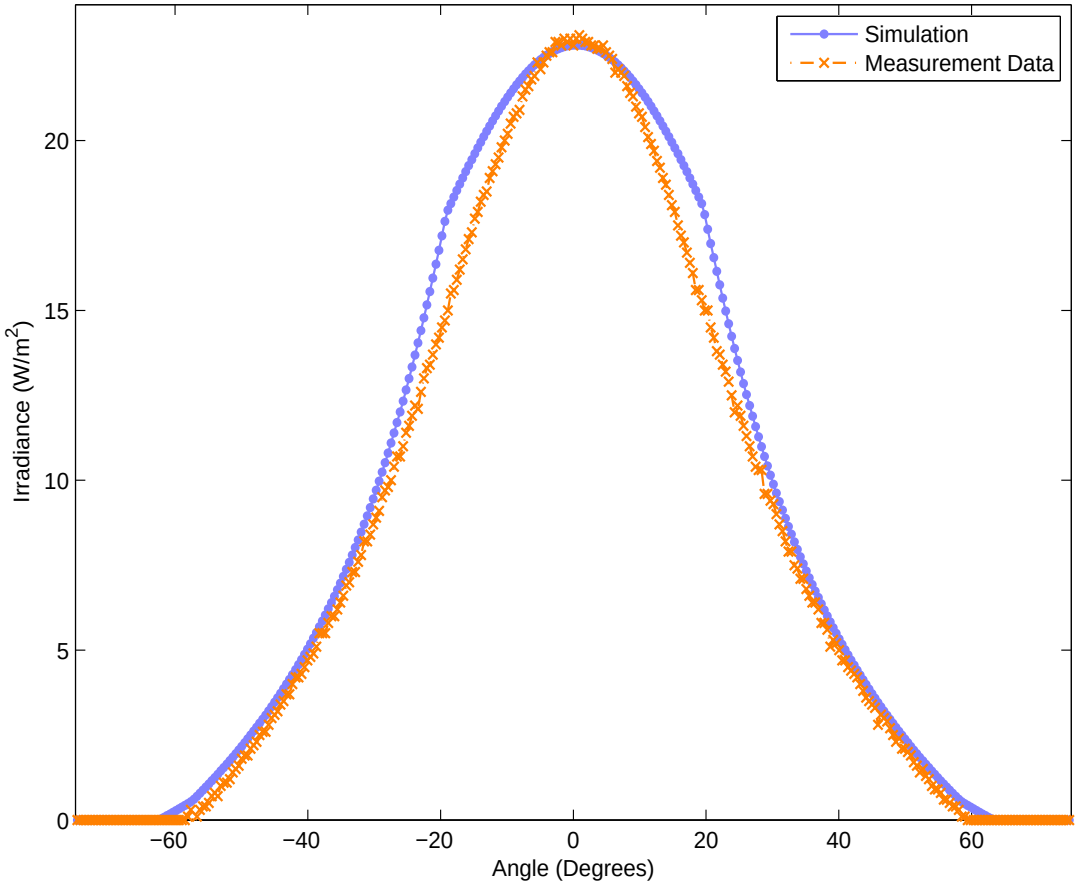

Figure 9.8: *Full rotation with* $D = 0.3285m$ *and squared attenuation*

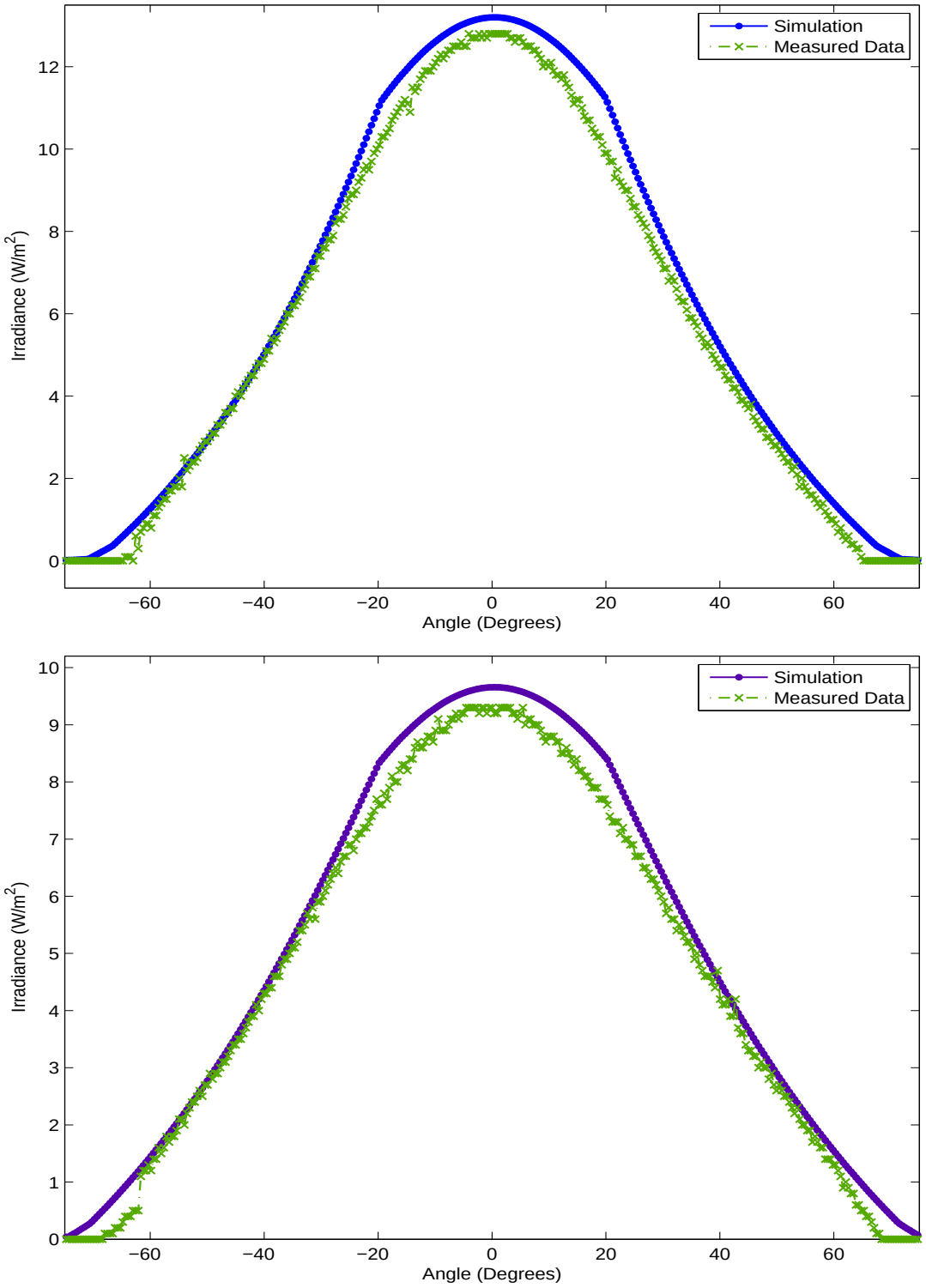

Figure 9.9: *Full rotations (A) $D = 0.4685m$ and (B) $D = 0.5685m$ with squared attenuation*

Table 9.3: Goodness of fit for squared attenuated reflective model

D of Rotation	r^2 value for measurements at D
$326.5mm$	0.9904
$468.5mm$	0.9927
$568.5mm$	0.9927

The squared attention function is a slight improvement over the linear function. While it still slightly overestimates, it is closer to the data points at far angles. Table 9.3 gives the co-efficient of determination for the squared attenuation function, all of which are slightly better fits than the linear fit. Of course as this function exists to adapt a one dimensional model to the effects of three dimensional clipping, it is very likely that better functions could be found that would improve the fit. Despite this, the simple functions derived result in very good agreement.

9.4 Contributions from secondary reflections

The contribution from secondary reflection was found by subtracting the the sum of direct, $M1$ and $M2$ irradiance from a run with both mirrors. It was found to be minimal and hard to distinguish from noise. The difference for $D = 0.3285$ and $D = 0.4685$ are shown in figure 9.10. The low values recorded suggest it can effectively be disregarded.

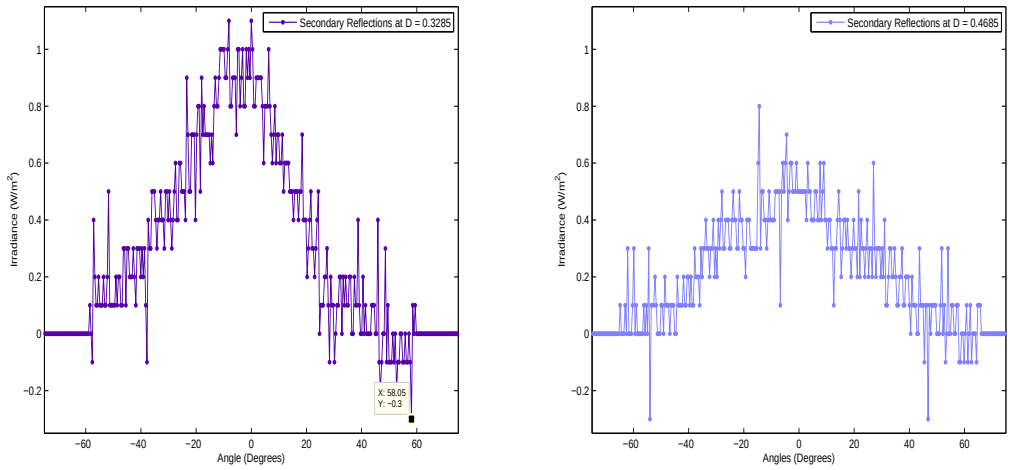

Figure 9.10: *Secondary contributions are minimal in all cases*

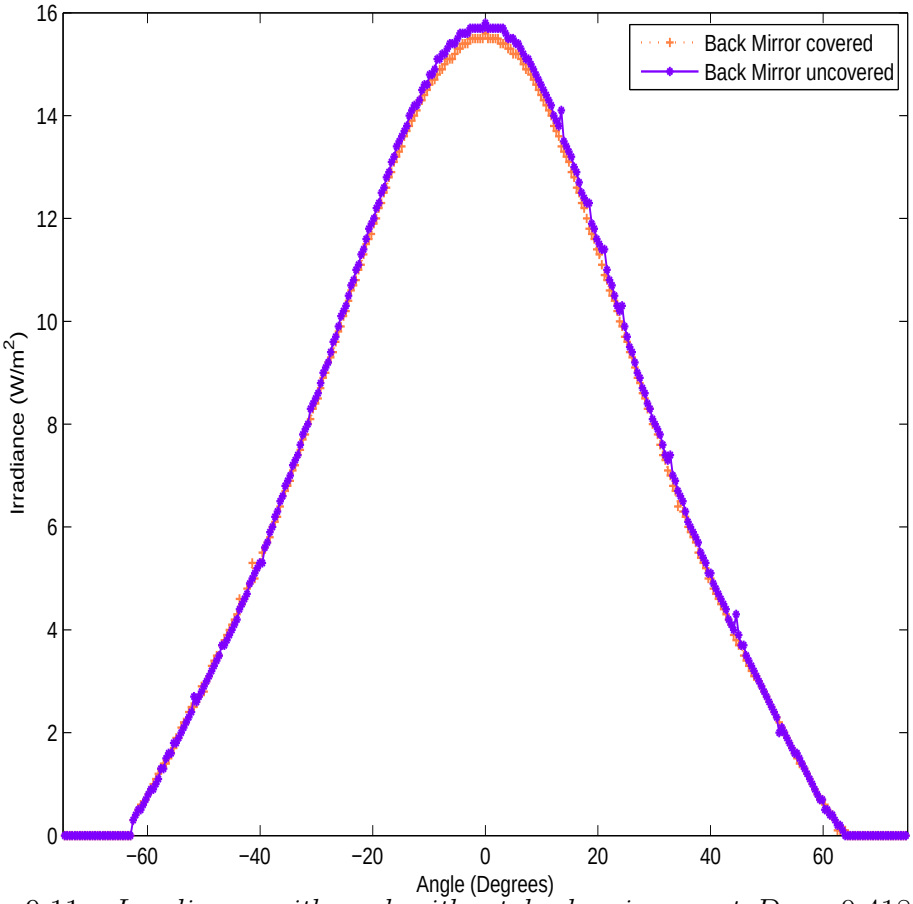

Figure 9.11: *Irradiance with and without back mirrors at* $D = 0.4185$. *The difference in both rotations is negligible*

9.5 Contributions from back mirror

The experiment was repeated with back mirrors and both side mirrors uncovered to ascertain if the back mirror had any effect on over all irradiance; specifically ,if back directed radiation would be scattered from the back mirror to the side mirror and then out. However, after investigation, the back mirror was found to contribute a negligible amount to the recorded irradiance. An example of this is shown for $D = 0.4185m$ in figure 9.11. The indication seems to be that the presence of the back mirror does not heavily influence overall irradiance and can be discounted.

9.6 Conclusions

The effects of secondary reflection seem to be minimal in this particular mirror geometry and hard to distinguish from noise. Similarly, the effects of the back mirror did not change the results significantly and suggests it can be disregarded without loss of generality.

The collimated detector saw three distinct peaks in each rotation (figures 9.4 and 9.5) with both side mirrors exposed; a high central peak and then lower peaks equidistant on either side. This observation supports the theory underpinning the specular reflective model, as it predicts an non-diffuse image of the tube will be formed in mirrors surrounding it. The model predictions versus what was measured in the subsequent rotations were in very close agreement. The R_f measured value of 0.7761 with a standard deviation of 0.014 was slightly lower than the up to 0.85 quoted by Waldmann, but as the cabin being used was quite old, gradual degradation of the anodized layer could explain the lower value. Also, the method by which R_F was calculated meant that if the peak in the data didn't include the image centre a lower value could arise. In any case, the agreement is good in all cases and the standard deviation low.

The model clipping factor seems to be the greatest cause of uncertainty, and greater accuracy would result from a better attenuation function. Despite this, the A_S factor gives impressive agreement and this model could be used as a basis for characterizing cabin reflections. Results were taken for off axis measurements and these also seemed to be in agreement with the model, however the measurements with lateral displacement were taken so far back that the readings were low and noise a significant problem. More investigation into what happens in these situations is recommended. The model does seem to give good agreement and can be used to model the effects of reflected UVR onto a patient in a treatment cabin.

Chapter 10

Ultraviolet dose modeling

In previous chapters, the nature of tube emissions, body obstructions and reflective contributions have all been discussed. With these factors quantified, it is possible to investigate and model the irradiance from a geometrical tube arrangement or series of tubes to estimate patient dose in different clinical situations.

10.1 Example with UV-1000 layout

The Waldmann UV-1000 cabin consists of twenty six TL/01 type bulbs arranged in two distinct mirror geometries. A full diagram of the layout can be found in appendix D and an illustration is shown in figure 10.1. In a UV-1000 cabin there are two distinct mirror geometries; those with a face width of $98mm$ and those with $80mm$, both of which are labeled in the figure. Ten of these lamps are arranged with the former geometry and the remaining sixteen with the latter. The automated detector with arm length $L_T = 0.15m$ makes a full rotation when centred in the cabin and it is possible to then estimate the recorded irradiance in such a rotation.

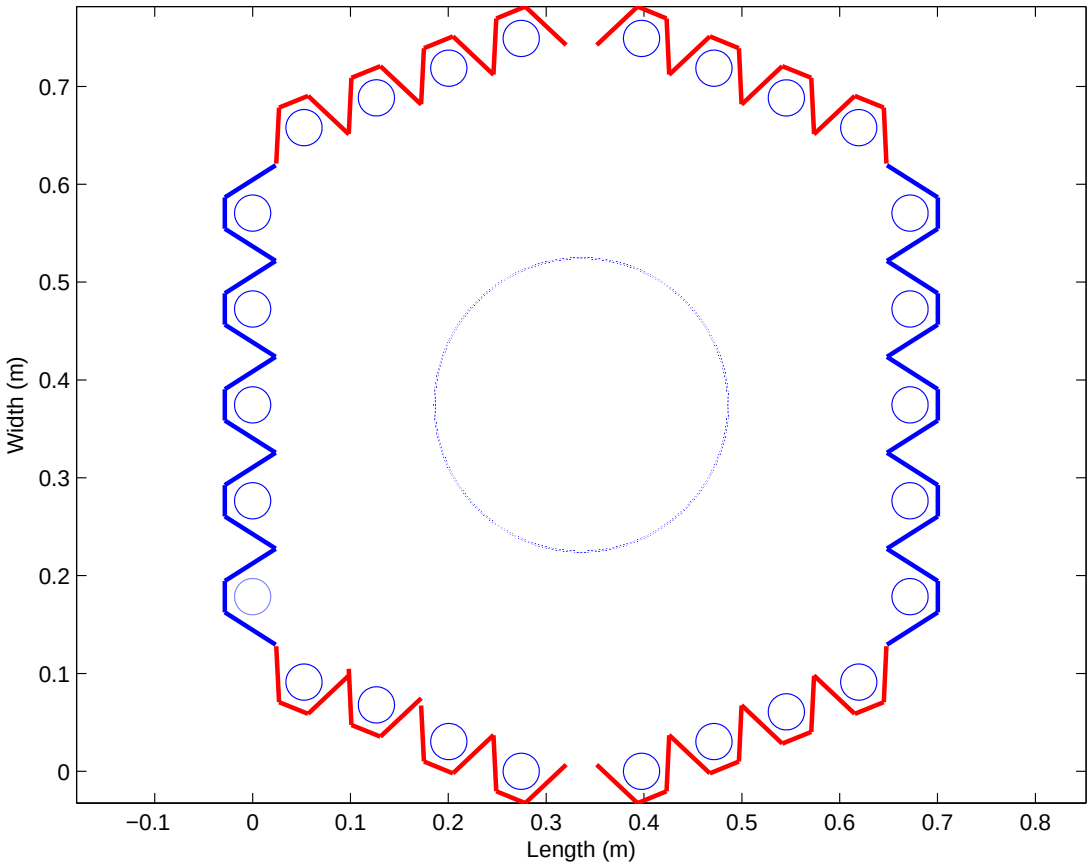

Figure 10.1: *Waldmann UV-1000 cabinet layout. Tubes with a front width of* 98mm *are shown in blue, tubes with front width of* 80mm *in red.*

It is relatively straightforward to implement a simple simulation to estimate the dose recorded by an automated detector rotating around in the cabin as shown in the figure. This is shown in figure 10.2 with the abrupt attenuation for ease of programming and $S_R = 0.97$, $R_F = 0.78$. The simulation is to illustrate the concept and as it uses an overly harsh attenuation it may result in sharp cut-offs. It is of course possible to use the A_S attenuation function to improve the quality of the simulation as discussed in the previous chapters. The average cabin irradiance from the simulation is $71.36W/m^2$ or $7.136mW/cm^2$ which is in remarkably good agreement with the measured average value of $70.045W/m^2$ or $7.0045mW/cm^2$, also shown in figure 10.2.

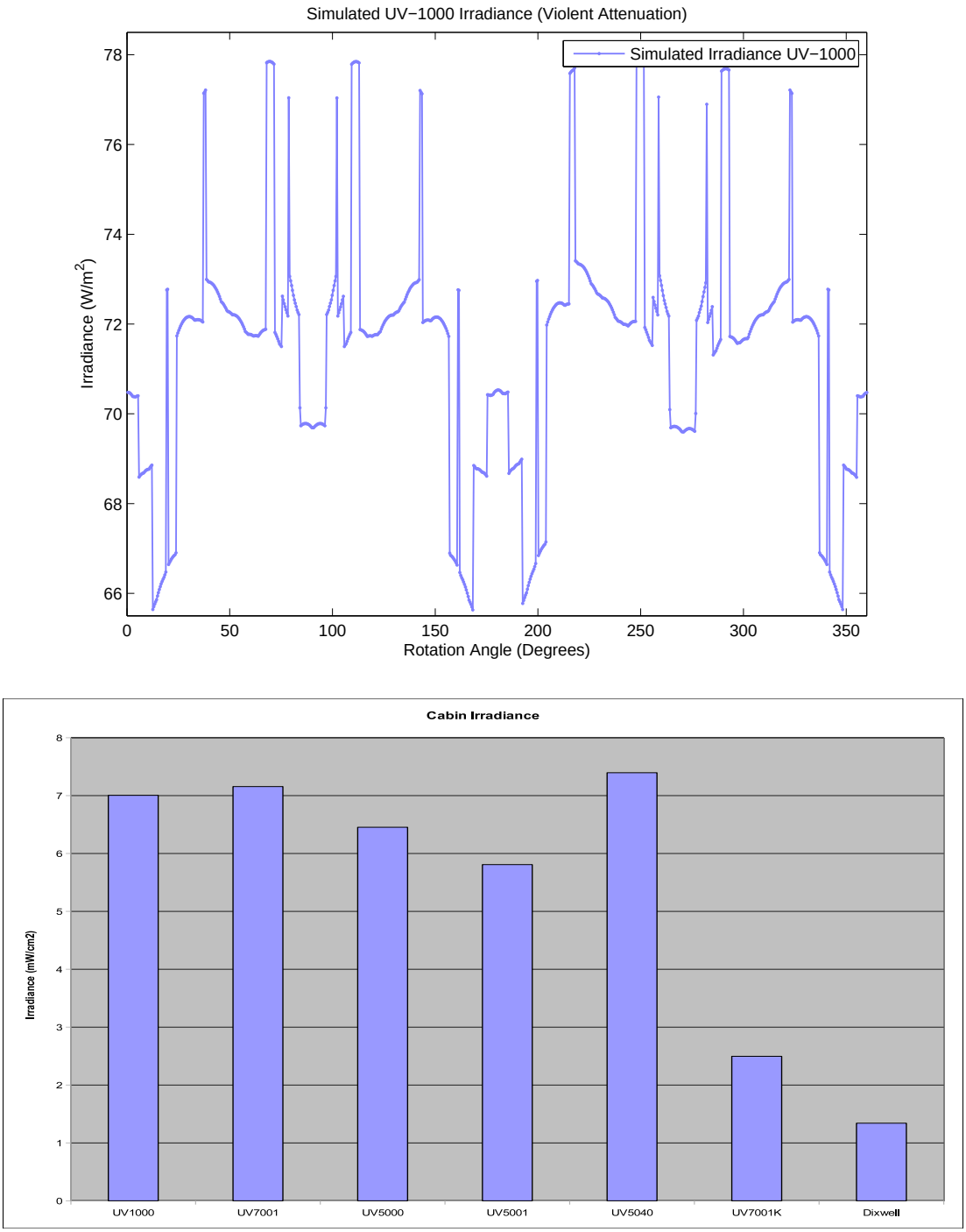

Figure 10.2: *Simulation of a UV-1000 cabin. Abrupt attenuation used for simplicity and illustration of concept with average value of* $7.136 mW/cm^2$. *Bottom bar chart shows measurements of average cabin irradiance for different models, reproduced with permission of CJ Martin. Irradiance for UV-1000 cabin is* $7.0045 mW/cm^2$, *in excellent agreement with simulation average.*

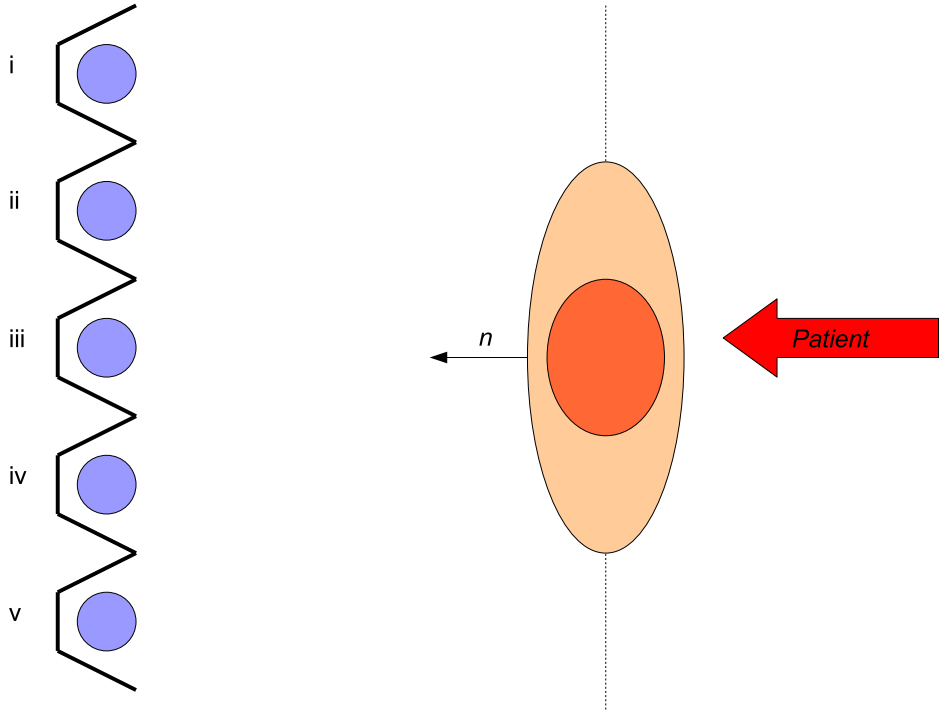

Figure 10.3: *Elliptical patient standing in front of five UVR tubes.*

10.2 Effects of tube failure

An advantage of having a UVR dosimetry model is that is allows simulation of effects both desirable and undesirable. For example, it is possible to simulate the effects of tube failure on patient dose. Consider the elliptical patient depicted in figure 10.3 whose torso is centred on $(h, k) = (0.5m, 0.5m)$ and semi-major axis length $a = 0.1935m$ and semi-minor axis length $b = 0.1185m$. The patient is standing facing five UVR tubes with surrounding reflectors, each reflector having a face length of $98mm$. The patient normal from their chest is denoted by the black arrow $\vec{n} = -\vec{x}$. It is possible to use the irradiance / reflective model this time with attenuation factor A_S to estimate the change in recorded irradiance when different lamps fail. When a lamp fails, it is reasonable to assume the reflectors around it cease to contribute.

Table 10.1: Effects of failing tubes

i	ii	iii	iv	v	Irradiance (W/m^2)	Relative intensity
On	On	On	On	On	33.5598	1
Off	On	On	On	On	29.0642	0.8663
On	Off	On	On	On	25.5501	0.7613
On	On	Off	On	On	24.9904	0.7447
Off	On	On	Off	On	21.0646	0.6277
On	On	Off	On	Off	20.5048	0.6110
On	On	Off	Off	On	16.9808	0.5060

Table 10.1 shows the various recorded irradiances with different tubes failing by utilizing the simulation with $S_R = 0.97$ and $R_f = 0.78$ where lamps $i - v$ are denoted as being either 'on' or 'off'. The relative effect on intensity is noted in the table alongside the recorded irradiance at the measurement point.In this example, the effects of failing tubes can be readily quantified - a tube from the far end failing (tube i or tube v) will reduce the over all intensity on the patient chest to just under 87% of the total value. By contrast, a single tube failing in the centre such as tube iii in this example reduces the intensity to just over 76% of the initial amount. It can be seen that two tubes (tube iii and tube iv or tube ii) account for just under half the dose received between direct contributions and mirror contributions in this particular geometry. One of the chief advantages of the model is that it allows for greater investigation of issues such as this which often arise in UVR phototherapy.

10.3 Effects of mirror geometry

The reflective portion of the model has some interesting predictions regarding mirror geometry. Specifically, it indicates that the wider the mirror angle γ is, the more UVR is forward directed and the less clipping becomes a factor, meaning less reduction in the emitted radiation. Conversely, the smaller the angle is, the more radiation is clipped by the reflector edge, and the less radiation that is effectively forward scattered. When the angle $\gamma = \pi/2$, another problem arises in that the side mirrors essentially become a 'flat' back mirror such as those seen in the National Biologic cabinets. This situation is also not ideal, as there is now only one image rather than two and clipping from the tube itself becomes a factor. This has implications for how cabins are built and indeed, there is also physical evidence that tubes with 'wider' angles are more efficient. Figure 10.5 shows the approximate irradiance per tube in various cabin geometries.

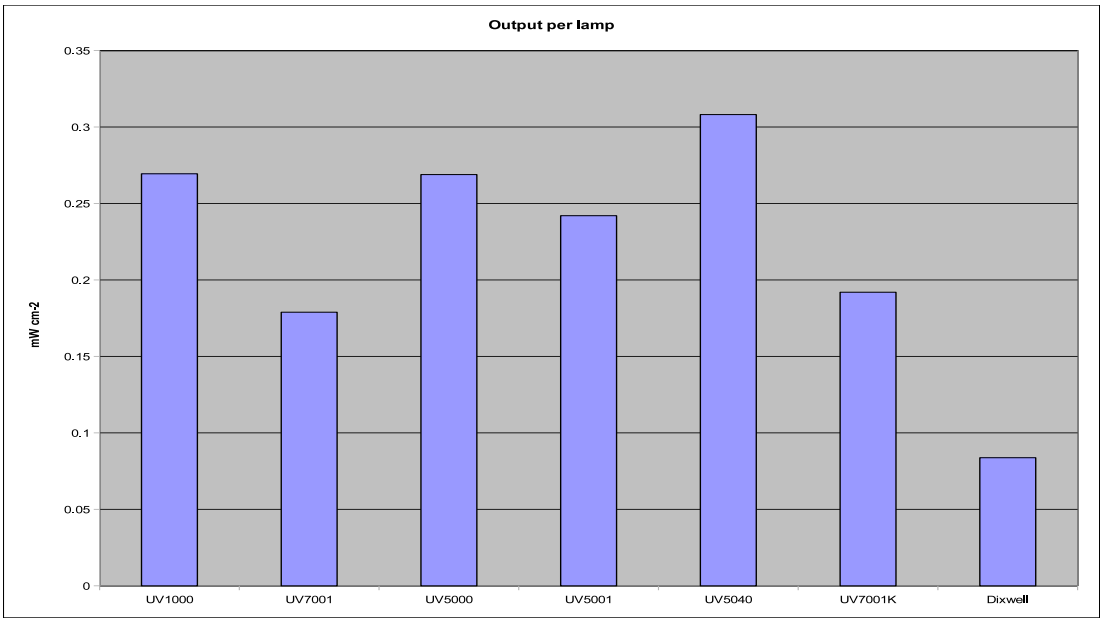

Figure 10.4: *Average output per lamp arrangement. Highest output is from UV-5040 arrangement* ($3.081 W/m^2$) *which also has largest angle values with arrangements from* $\gamma \simeq 50°$ *to* $\gamma \simeq 70°$

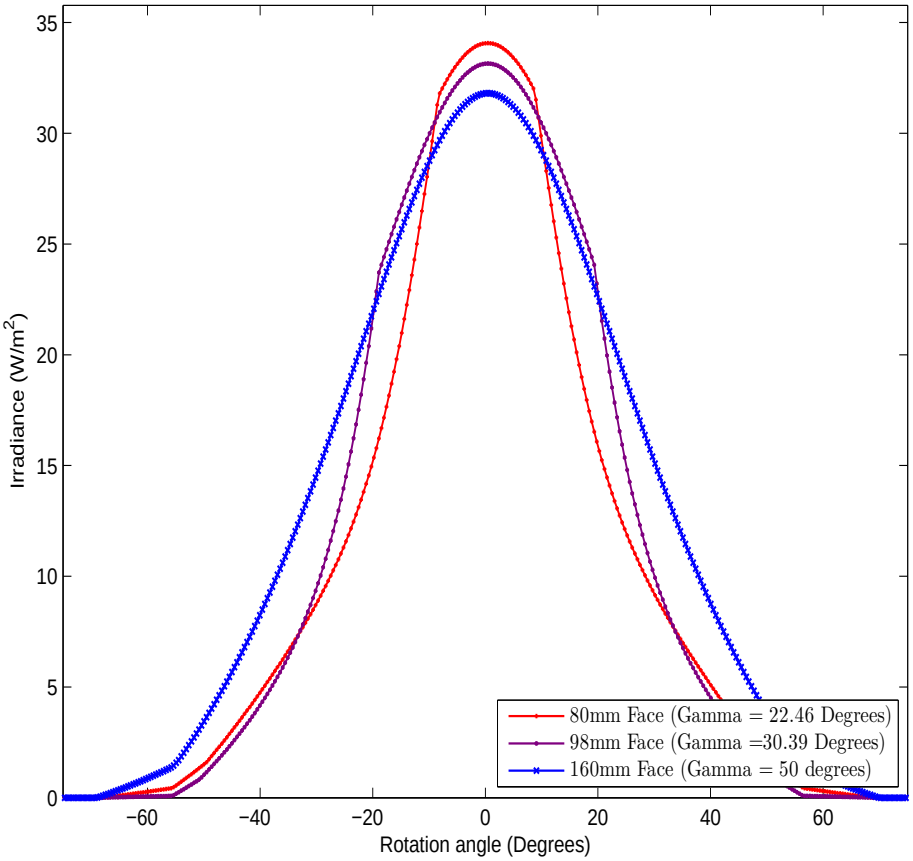

Figure 10.5: *Simulated effects of different face lengths and consequently γ angles on rotational irradiance.*

Table 10.2: Reflector geometries

Face length (mm)	Depth (mm)	γ (degrees)	Typical Configuration
80	52	22.46	UV-1000 corners
98	52	30.34	UV-1000 sides
160	52	50	UV-5040 sides

In table 10.2 above, there is a distinction between the angle at cabin sides and corners. This is because there are can be multiple mirror arrangements even inside a single cabin. In the UV-1000, there are two; one along the long side and another at the inclined sides. See appendix D for more details.

The effects of varying the angle and face length are quite clearly shown by the model; a greater value for γ results in a wider spread of UVR around the cabin and slightly reduced irradiance directly in front of the tube. Smaller values for γ and correspondingly smaller values for the face length result in most of the reflected UVR being directed into a very narrow stream in front of the tube and very little spread around the cabin. This has implications for how cabins are designed and indeed what reflector geometries may be preferable for different forms of treatment. A valid question is do we expect more or less potential contribution from secondary reflections with a wider γ angle. The answer is no, as a wider angle forces the secondaries closer together and they endure more clipping. An example of this for $\gamma = 50°$ is depicted in figure 10.6.

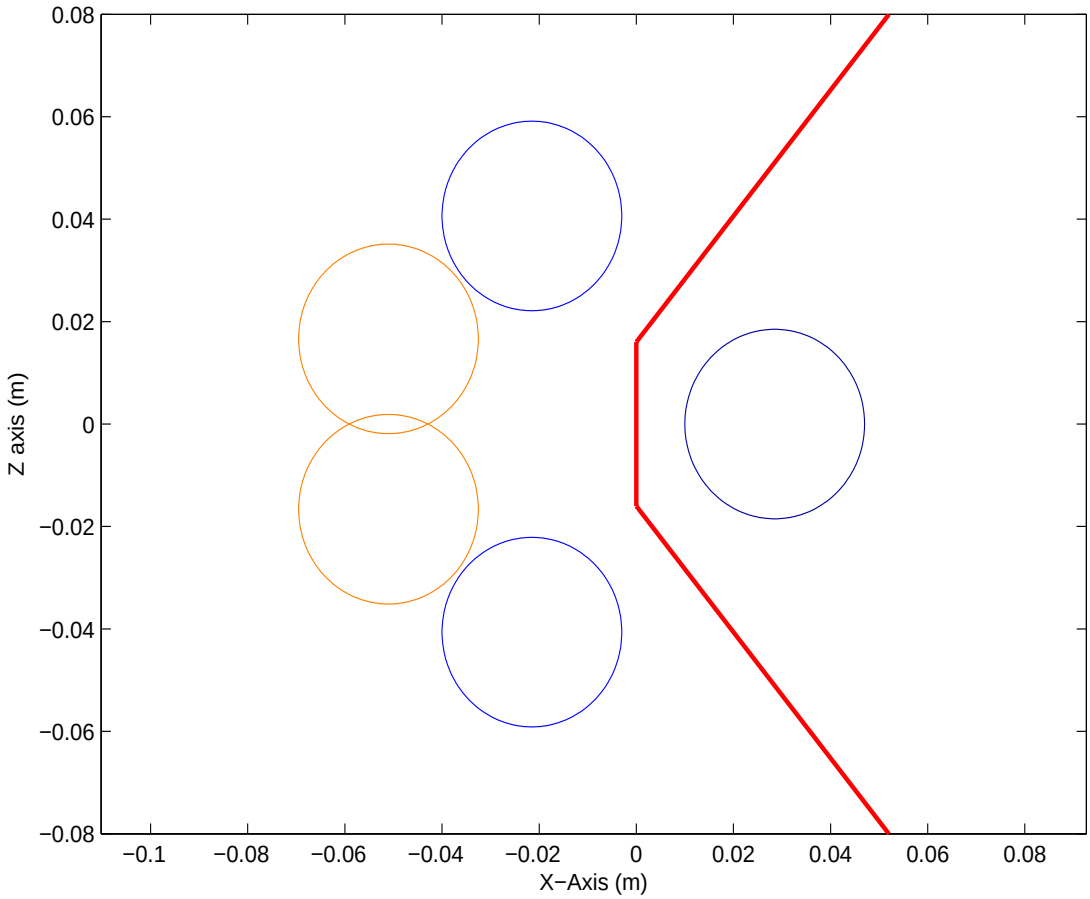

Figure 10.6: *Secondary images (shown in orange) for $\gamma = 50°$. Secondary images are extremely clipped.*

10.4 Conclusions

Bringing together separate elements such as tube and reflective modeling which have been previously outlined in this work allows theoretical investigation of numerous problems in phototherapy. Potential applications of these have been outlined in this chapter for examples such as tube failure and the impact of different mirror geometries.

It is possible to combine these elements with the obstruction factors outlined for the radial precursor, and this could allow for very powerful dosimetry. It would be possible to model this either by coding it or using the results of this work in a commercial light tracing package, specifying how tubes emit and how reflections are formed. Such packages can be costly but with correct modification could more than suffice to run implement the findings of this volume of work.

Chapter 11

Conclusions and future work

The aim of this work was to develop a model for dosimetry in ultraviolet phototherapy, and investigate the factors influencing this. A model was outlined with good predictive power to deal with both direct irradiance and reflected irradiance, and a method for estimating the shielding factors provided by the patient was explored. The chief conclusions of this work are listed in the following sections.

11.1 Characterization of Lamp source

Fundamental to the aim of this work was to find a powerful and accurate method of determining the output irradiance from a UVR lamp source at any potential orientation and distance from the tube itself. The radial model was found to be lacking and useful only for very specific applications in the near field when the surface orientation was parallel with the tube surface and facing it directly, a situation that cannot realistically be expected in phototherapy applications. With this model not adequate, a new model was derived that treated the lamp as a one dimensional line source. This model was theoretically derived and was in principle capable of handling the situations in phototherapy where the surface normal may take many values. The model was experimentally verified and found to give very impressive accuracy, thus qualifying it for use as a model of the emissions from UVR lamps.

11.2 Reflection modeling

The next addition to the dosimetry model was to allow for reflections from the highly anodized aluminium reflectors. This was done by assuming the majority of the radiation was approximately specular and the tube forms an image in the reflector; this image would then emit as a tube standing at those co-ordinates save its over all power output would be reduced by the reflectivity of the material at UV wavelength. The complication is that while the one dimensional line source has no extent in the model, in reality tube sources are slightly extended sources and thus a degree of clipping and attenuation occurs depending on the position of the detector / skin relative to this reflector. Hence, a method for estimating regions of mirror contribution and an attenuation function allowing for the physical extent of the tube was derived. This addition was found to give very good estimates of the contribution of reflection. The attenuation function derived was somewhat ad hoc but quantified the clipping factor well, though better fits may be possible.

11.3 Obstruction and shielding

A method was suggested of approximating patients to conic sections to estimate the shielding factors during treatment. With the emission from the tube modeled and the reflective contribution, it would be possible to use a mesh model of a human body to estimate the irradiance at any point with more certainty. The findings of this work could be used in a commercial ray tracing package to better model the effects of human obstruction, beyond the simple circle / ellipse method.

11.4 Future work

Future work might involve using the results of this work in conjunction with a commercial light tracing package to better model obstructions. The attenuation factor for reflective clipping could also be examined in more depth, perhaps with the aid of a commercial ray tracing program to better understand the attenuation due to mirror clipping.

11.5 Conclusions

The body of work in this thesis provides the framework for a full computational dose model. Some other conclusions arising from this work are the effects of reflectors in cabin design; the reflective model predicts that wider angles between the mirrors forward directs more radiation and reduces clipping, and indeed, this has been experimentally noted in different cabins. A powerful dosimetry model has been developed that can quantify dose well. This model could be of use in clinical practice and in the study of processes such as photoadaptation, where the mechanisms would be easier understood if dose could be strictly quantified. This model could also be useful for modeling the effects of common clinical situations, including tube failure and patients standing off centre in the treatment cabins.

Appendix A

Anodized reflector specifications

The graph in figure A.1 is from Waldmann and shows the reflection vs. wavelength of Anodized 316G2. There was no such graph available for Anodized 318G2, but the engineers pointed out that the reflection behaviour of 316G2 and 318G2 is essentially the same. Notice the modulations caused by the interference with the anodized layer and the aluminium which display in the graph as a zig-zag shape. The reflectance of this material at $\lambda = 311nm$ is up to 0.85. The total diffuse reflection from the material is approximately 8%.

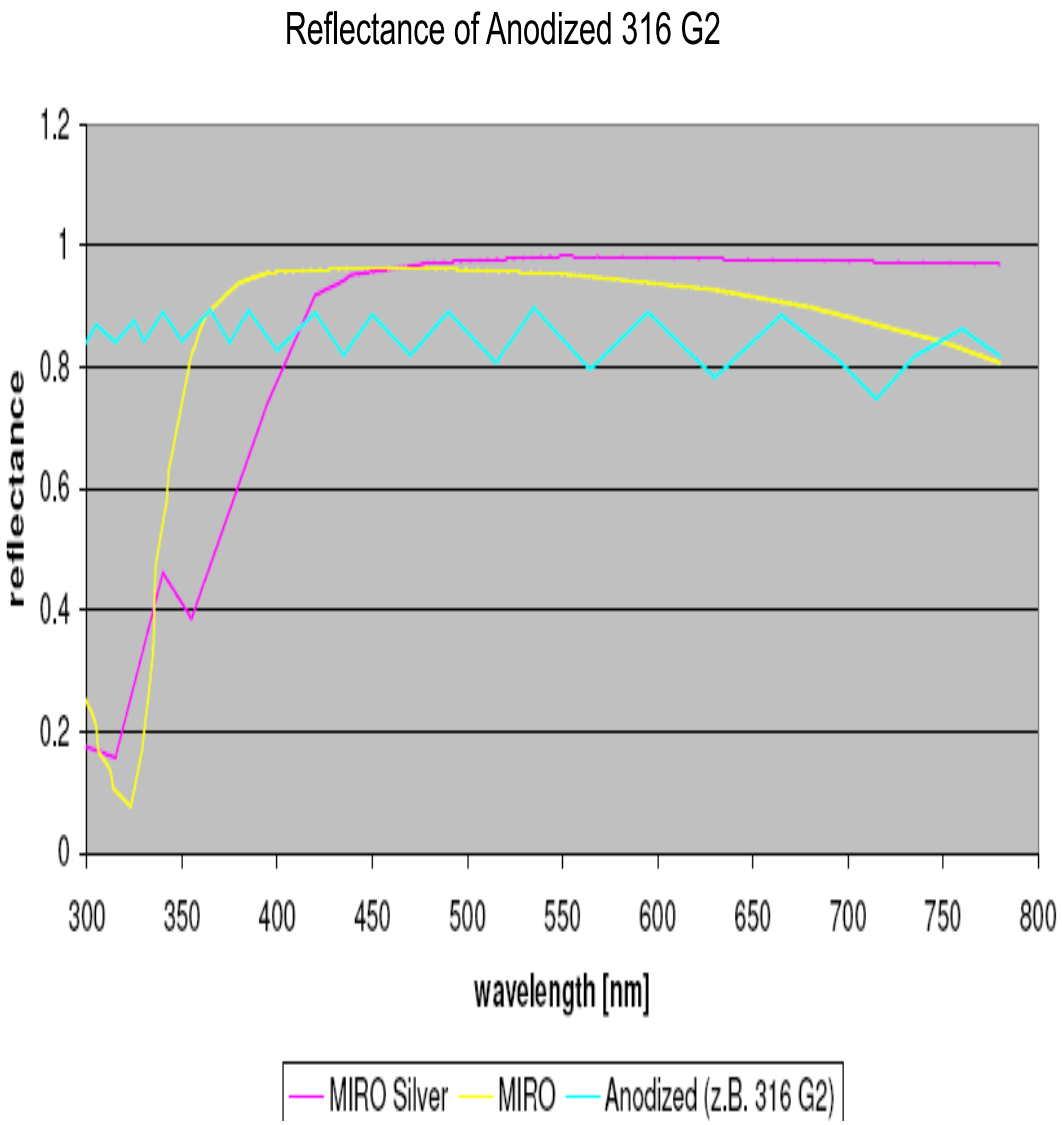

Figure A.1: *Reflectance with wavelength of 316GS Anodized material. Reprinted with permission from Waldmann*

Appendix B

Extended source model

Chapter 6 introduced a rigorously derived line source model. This appendix outlines the steps required to derive an extended source model or surface source model, which instead of treating the tube as a linear array of point sources treats every point as the surface as a point source. The analysis is broadly similar to the line source derivation.

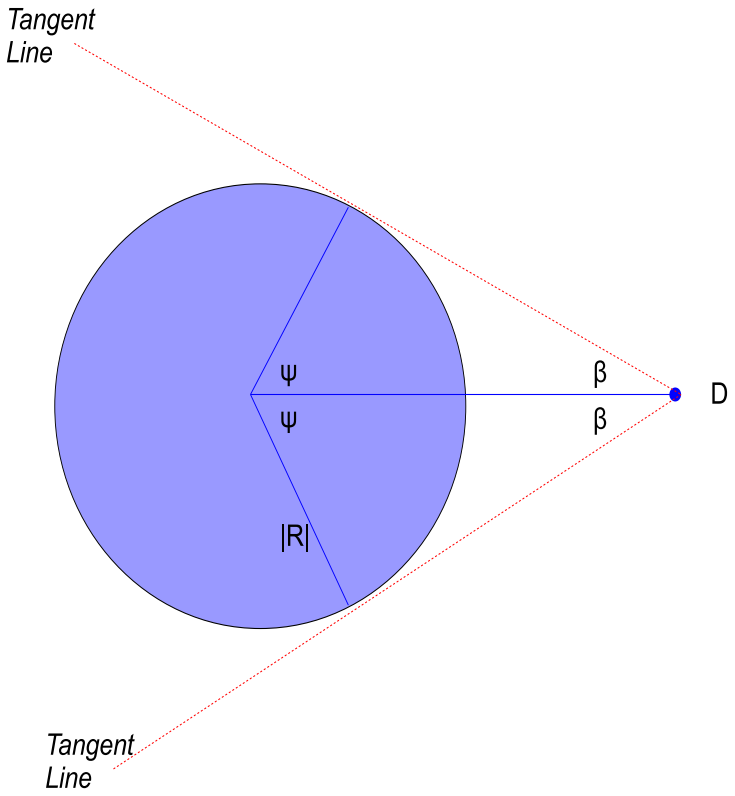

Figure B.1: *Important angles in the extended source model.*

Consider a detector at point D a distance D away from the tube centred on *(g,f)* with radius R as depicted in figure B.1. It forms an angle with the centre of the tube of γ and a bisector angle of angle of β which is given by

$$\beta = \arcsin[\frac{R}{D}] \tag{B.1}$$

This means that the inner angles Ψ are given by

$$\Psi = \pi/2 - \beta \tag{B.2}$$

Thus the angular extent ϕ between the two tangent lines is

$$\gamma - \beta < \phi < \gamma + \beta \tag{B.3}$$

The radial vector between points on the tube in this angular extent and the detector are given by

$$\vec{r} = (D_x - (g + R\cos\phi))\vec{x} + l\vec{y} + (D_z - (f + R\sin\phi))\vec{z} \tag{B.4}$$

This can be rewritten for simplicity as

$$\vec{r} = D\vec{x} + l\vec{y} + Z\vec{z} \tag{B.5}$$

By manipulating the identity in equation 6.8, the extended form can be written as

$$E = S_A \int\int \frac{\vec{n}\cdot\vec{r}}{|n||r|^3} dl d\phi \tag{B.6}$$

where S_A is power per unit area. This can be written as

$$E = S_A \int\int \frac{AD + Bl + CZ}{|n|\sqrt{(D^2 + Z^2 + l^2)}^3} dl d\phi \tag{B.7}$$

This can be solved for dl and results in an expression similar to that of the general from

$$\begin{aligned} E &= \int \frac{S_A}{|n|(D^2+Z^2)}[\frac{(AD+CZ)(L-h) - B(D^2+Z^2)}{\sqrt{D^2+Z^2+(L-h)^2}} \\ &+ \frac{(AD+CZ)(h) + B(D^2+Z^2)}{\sqrt{D^2+Z^2+h^2}}]d\phi \end{aligned} \tag{B.8}$$

Returning D and Z to this question yields

$$
\begin{aligned}
E \;=\; & \frac{S_A}{|n|}\int \frac{(D_x-(g+R\cos\phi)}{((D_x-(g+R\cos\phi))^2+(D_z-(f+R\sin\phi))^2)}[\\
& \frac{(A(D_x-(g+R\cos\phi))+C(D_z-(f+R\sin\phi)))(L-h)}{\sqrt{(D_x-(g+R\cos\phi))^2+(D_z-(f+R\sin\phi))^2+(L-h)^2}} \\
- \; & \frac{B((D_x-(g+R\cos\phi))^2+(D_z-(f+R\sin\phi))^2)}{\sqrt{(D_x-(g+R\cos\phi))^2+(D_z-(f+R\sin\phi))^2+(L-h)^2}} \\
+ \; & \frac{(A(D_x-(g+R\cos\phi))+C(D_z-(f+R\sin\phi)))(h)}{\sqrt{(D_x-(g+R\cos\phi))^2+(D_z-(f+R\sin\phi))^2+h^2}} \\
+ \; & \frac{B((D_x-(g+R\cos\phi))^2+(D_z-(f+R\sin\phi))^2)}{\sqrt{(D_x-(g+R\cos\phi))^2+(D_z-(f+R\sin\phi))^2+h^2}}]d\phi
\end{aligned}
\tag{B.9}
$$

This equation has no real analytical solution and cannot be solved explicitly but can be approximated with numerical integration between the angular limits set out in equation B.3. The extended source model is rather unwieldy in comparison to the line source approximation but could potentially be used to investigate clipping in the reflective model. However, when a numerical approximation is used to test this model, the results are quite poor; the model under-predicts massively near the tube. The surface source area model has very poor predictive power, which implies that the vast majority of the emitted photons originate in the centre and very few are expelled at wide angles from the surface. For this reason, it would seem the line source model is not only more simple, but far more accurate. Ergo is is unlikely that the surface source arrangement would improve the dose model as it stands without major modification or weighing.

Appendix C

Method of finding S

Finding the points of intersection illustrated in figure C.1 is important to estimating the attenuation factor A_S. There are several ways to do this and one method is outlined in this appendix. The idea behind the method is essentially to find the tangent at P and the equation of the line L from the measurement point through the upper mirror point U. The equation of the tangent line T with slope m_T can also be readily found, and from this the equation of the line orthonormal to it through the point P with slope $-1/m_T$. From this, the point of intersection M can be found and hence S.

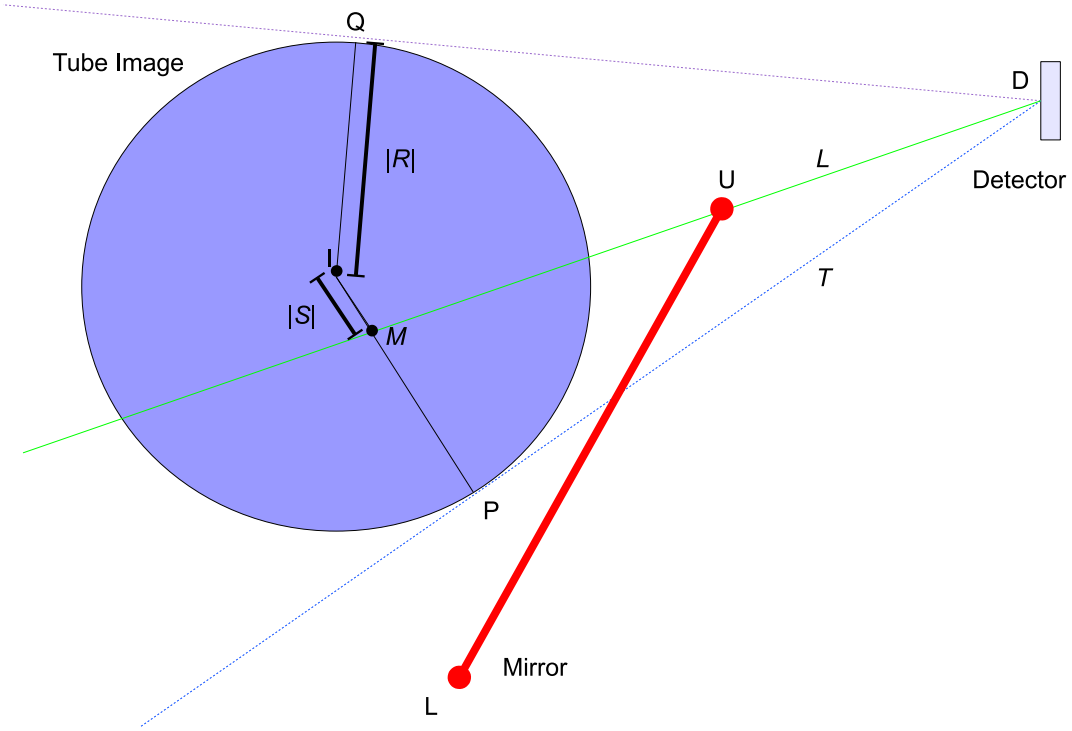

Figure C.1: *Points of interest in attenuation zone*

The detector stands at $D = (D_x, D_z)$. The slope of the line L through the upper part of the mirror part U is given by

$$m_L = \frac{D_z - U_z}{D_x - U_x} \tag{C.1}$$

and so the z co-ordinate along this line for any value of x is then

$$z = m_L(x - U_x) + U_z \tag{C.2}$$

This is the central line equation. Now an equation is needed for the line T from the detector at D to the tangent point at P. The slope of this line m_T can be

taken by finding the angle γ from D to the centre of the tube (S_x, S_z and the bisector angle β as outlined in chapter 5 and appendix B. From this is follows that the slope is

$$m_T = \tan(\gamma + \beta) \tag{C.3}$$

and it follows that the equation of this line is

$$z = m_T(x - D_x) + D_z \tag{C.4}$$

This tangent line T touches the tube at one place $P = (P_x, P_z)$. Solving one allows easy calculation of the other. Knowing the discriminant is zero at a tangent point, manipulation of the quadratic identity gives

$$P_x = \frac{2(S_x + m_T S_z - m_T(D_z - m_T D_x))}{2(1 + m_T^2)} \tag{C.5}$$

and from this

$$P_z = m_T P_x + D_z - m_T D_x \tag{C.6}$$

and hence from this S can be easily calculated by using the distance formula

$$S = \sqrt{(S_x - P_x)^2 + (S_z - P_z)^2} \tag{C.7}$$

and from these both the linear and squared attenuation factor can be calculated. Linear attenuation is given by

$$A_L = 1 - S/R \tag{C.8}$$

and the squared attenuation factor by given by

$$A_S = (1 - S/R)^2 \tag{C.9}$$

Appendix D

UV-1000 Engineering diagram

This appendix contains an autocad generated diagram of one half of the Waldmann UV-1000 layout, containing thirteen UVR lamps. The diagram was measured and put into CAD by Brendan Grimes of BEST Ltd.

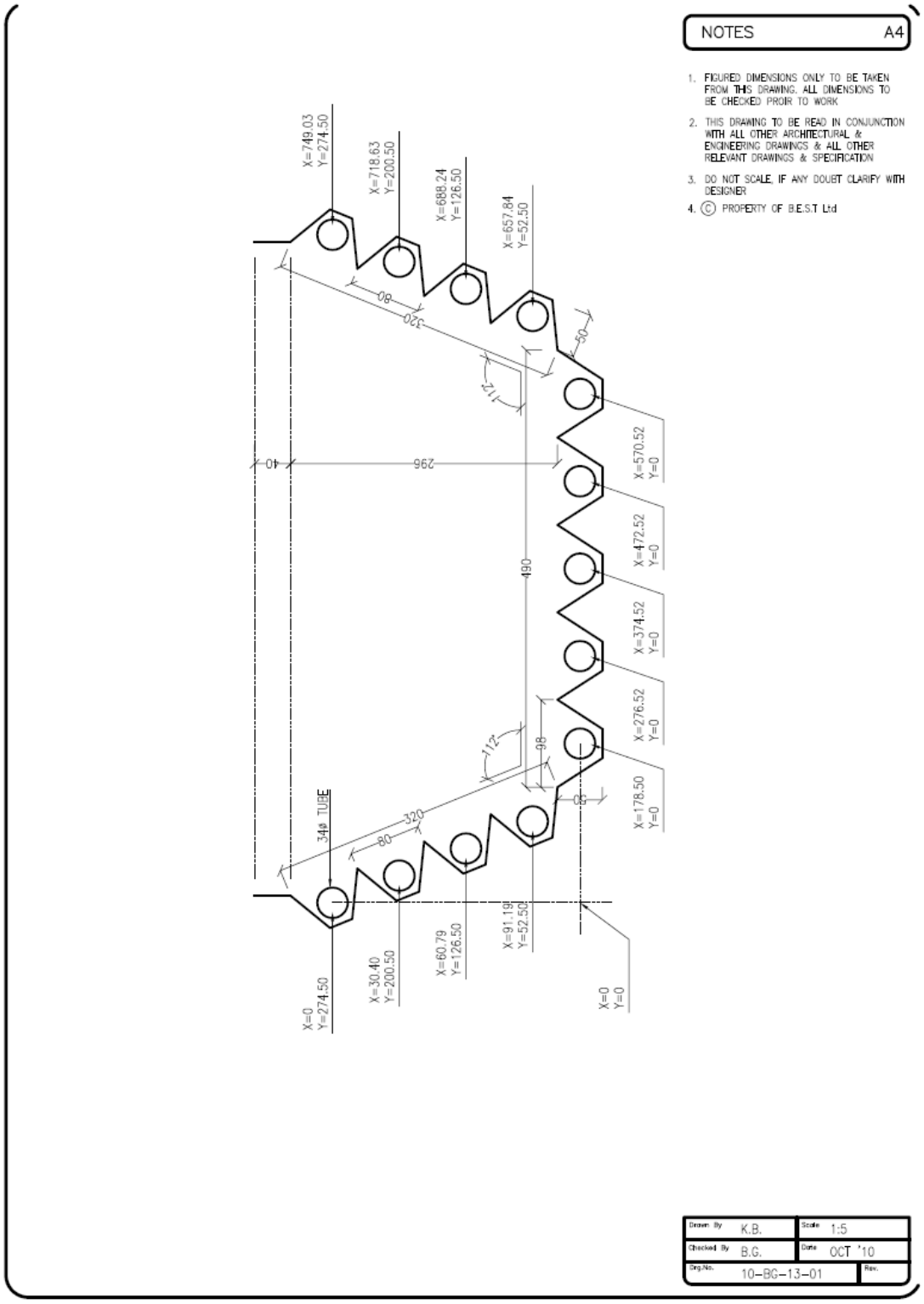

Figure D.1: *UV-1000 CAD layout. Courtesy of Brendan Grimes (BEST Ltd.)*

Appendix E

Uncertainty budget

This appendix contains a brief uncertainty budget for the rotating detector to quantify the sources of error in the experiment. Sources of errors were

- An error of up to 1cm radially outwards from the tube due to errors reading and aligning the scale ruler beside the track cradle
- An error of up to 1cm in the height measurement of the detector face and tube
- An error of up to 0.45° in a rotation of automated detector
- An error of up to 1° from potential lean of the apparatus below the level the spirt level could detect
- An error in measuring the radius of the tube
- An error due to radiometer round up / round down approximation.

These factors were duly considered and the respective maximum potential error in irradiance was calculated for each factor. As the model is quite complex, there are two uncertainty budgets presented; one in the very near field of the tube, 10cm from the tube surface and another further away, 50cm from tube surface. The errors were calculated for a set up facing the tube at these two

values respectively. The detector was positioned at a height 85cm along the tube length and displacement in the z-axis was zero initially. S_R was 0.98.

Table E.1: Uncertainty Budget 10cm from tube surface

Uncertainty type	***Maximum error***	***Uncertainty Value***
Displacement error	0.01 m	$1.54W/m^2$
Height error	0.01 m	$3x10^{-4}W/m^2$
Radius error	$1x10^{-4}m$	$1.4x10^{-3}W/m^2$
Rotation error	0.45°	$3x10^{-4}W/m^2$
Inclination error	1°	$2x10^{-3}W/m^2$
Radiometer error	$5x10^{-3}W/m^2$	$5x10^{-3}W/m^2$
Total Uncertainty		$1.54W/m^2$
Expanded Uncertainty		$3.07W/m^2$

At 10cm displacement there is a maximum expanded uncertainty of $3.07W/m^2$ where the ideal reading is $16.3852W/m^2$. Total error at worst case is likely to be $16.3852 \pm 1.54W/m^2$. It is immediately apparent that displacement from tube surface is the biggest potential source of error. This can also be seen with 50cm displacement from surface budget in the next table.

Table E.2: Uncertainty Budget 50cm from tube surface

Uncertainty type	***Maximum error***	***Uncertainty Value***
Displacement error	0.01 m	$8.1x10^{-2}W/m^2$
Height error	0.01 m	$4x10^{-4}W/m^2$
Radius error	$1x10^{-4}m$	$7x10^{-5}W/m^2$
Rotation error	0.45°	$1x10^{-4}W/m^2$
Inclination error	1°	$3x10^{-4}W/m^2$
Radiometer error	$5x10^{-3}W/m^2$	$5x10^{-3}W/m^2$
Total Uncertainty		$8.1x10^{-2}W/m^2$
Expanded Uncertainty		$1.69x10^{-1}W/m^2$

From the 50cm uncertainty budget table it is clear that the expanded uncertainty is $1.69x10^{-1}W/m^2$ when the ideal reading is $3.2372W/m^2$. Total error at worst case is likely to be $3.2372\pm0.08W/m^2$. Again, difficulty in measuring displacement is the biggest possible source of error. As a result of this budget, it can be seen an improvement in distance measuring is recommended for greater accuracy.

Appendix F

Appendix

The figure in this appendix shows a human appendix. As there is currently no evidence that this particular organ has any relation to any of the biomedical and biophysical topics discussed in this thesis, one could conclude that this appendix, like its physiological namesake, is entirely vestigial.

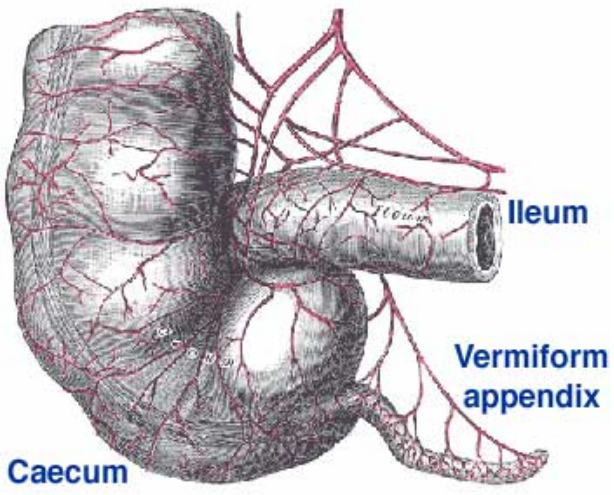

Figure F.1: *The Appendix, reproduced with modification from Gray (1918)*